

Electrochemical Investigation of Filiform Corrosion on Aluminum Alloys

by

Daniela Arango Vasquez

A thesis submitted in partial fulfillment of the requirements for the degree of

Master of Science

in

Materials Engineering

Department of Chemical and Materials Engineering  
University of Alberta

© Daniela Arango Vasquez, 2021

# ABSTRACT

Filiform corrosion (FFC, also known as under-film corrosion) is commonly observed on surfaces of coated aluminum (Al) and aluminum alloys (AA), especially in environments combining marine and industrial atmosphere. The chemical composition of the substrate is believed to play an important role in FFC resistance of AAs. However, there is still a lack of electrochemical studies focusing on clarifying the FFC behaviour of commercially used Al alloys. This work aims to investigate the FFC response of different AAs. To do so, commercially pure Al (AA1100) and AAs such as 2024 (Cu), 3003(Mn), 5052 (Mg), 6061(Mg, Si) and AA7075(Zn) were selected as candidate materials. The FFC behaviour of AAs was investigated using electrochemical methods. To simulate the under-film electrolyte environment, polarisation measurements were carried in a deaerated anolyte (5% NaCl + 0.1M AlCl<sub>3</sub>, pH=2) and an aerated catholyte (phosphate buffer solution, pH=7), respectively. Three factors were defined, including the resistance to FFC initiation ( $\Delta E_{PR}$ , V), the driving force for propagation ( $\Delta E_{corr}$ , V), and the FFC kinetics of propagation ( $i_{FFC}$ , mA/cm<sup>2</sup>). Results suggest that  $\Delta E_{PR}$  follows a tendency of AA 2024 (Cu) > 5052 (Mg) > AA7075 (Zn) > 3003 (Mn) > AA6061 (Mg, Si) > AA1100;  $\Delta E_{corr}$  followed the trend AA 6061 (Mg, Si) > 7075 (Zn), 3003 (Mn) > 5052 (Mg) > 2024 (Cu), 1100 and  $i_{FFC}$  followed the trend 7075 (Zn) > 6061 (Mg, Si) > 3003 (Mn) > 5052 (Mg) > 1100 > 2024 (Cu).

In addition, the influence of anodizing on the different substrates was evaluated using the same electrochemical parameters described for the bare alloys. AAs were pretreated with a three-step anodizing process: electropolishing in a 1:4 solution of HClO<sub>4</sub>:C<sub>2</sub>H<sub>5</sub>OH at 10 °C, sulfuric acid anodizing in 100 g/L H<sub>2</sub>SO<sub>4</sub> at 18 °C and hydrothermal sealing in boiling DI water. EC

measurements showed that anodizing could effectively lower the susceptibility of AAs to FFC. Resulting in a decrease in both, the driving force for FFC propagation ( $\Delta E_{\text{corr}}$ ) and FFC kinetics ( $i_{\text{FFC}}$ ).

Finally, the validation of the EC results was done by an accelerated exposure test. Bare and anodized AA disks were coated with a clear epoxy layer, scribed, and placed in an environmental testing chamber at 80% RH at 40 °C for 1000h. Two parameters were defined (i.e., number of threads (N) and length of the filaments (L)), and calculated by visual examination with naked eyes and OM. The results from this section agreed with what was found through EC methods. The FFC susceptibility of bare samples predicted by EC measurements follows the same trend as that one found by accelerated exposure testing. Additionally, anodizing was confirmed to drastically increase FFC resistance on AAs, resulting in a strong decrease on N and L after 1000h of exposition.

# PREFACE

This thesis is my original work. I was responsible for the data collection and analysis as well as the manuscript composition under the supervision and edition of Dr. Jing Liu. Part of Chapter 3 has been published and presented as *D. Arango, J. Liu, "Electrochemical study of aluminum filiform corrosion" COM 2021: Advances in Metallurgy and Materials Engineering, Canada.*

# DEDICATION

*To my loving family:*

*This thesis work is dedicated to my husband, David, who has been a constant source of support and encouragement during the challenges of graduate school and life. This work is also dedicated to my parents, Nelson and Angela who gave me the opportunities and experiences that have made me who I am, and last but not least to my little sister Kelly, who has always been there for me. I am truly grateful to have you all in my life.*

# ACKNOWLEDGEMENTS

Would first like to thank my supervisor, Dr. Jing Liu, who has been an excellent professor and role model. It has truly been an honour and privilege to have been provided guidance from such an admirable researcher and wonderful person. I will always be grateful for her kindness, patience, and utmost understanding.

I would also like to thank my friends and lab mates, Haoxiang Wang, Meifeng Li, Ezz Ahmed and Xinze Li for their friendship and cherished time spent together in the lab. It is their kind help and support that have made my academic life a wonderful time.

In addition, I would like to thank my former professor, Dr. Carlos Ostos who was my first mentor and provided me with the tools that I needed to choose this path and complete my dissertation.

Financial support from Mitacs and our industrial partner, Starline Windows, is gratefully recognized.

Finally, I would like to thank all my family. Without their understanding and encouragement, it would be impossible for me to complete my study.

# TABLE OF CONTENTS

PREFACE .....	iv
DEDICATION .....	v
ACKNOWLEDGEMENTS .....	vi
TABLE OF CONTENTS .....	vii
LIST OF TABLES .....	x
LIST OF FIGURES .....	xiii
LIST OF ABBREVIATIONS .....	xix
LIST OF SYMBOLS .....	xx
CHAPTER 1 INTRODUCTION.....	1
1.1 RESEARCH BACKGROUND .....	1
1.2 PROBLEM STATEMENT .....	5
1.3 RESEARCH OBJECTIVES .....	7
1.4 THESIS OUTLINE.....	9
CHAPTER 2 LITERATURE REVIEW .....	10
2.1 ALUMINUM AND ITS ALLOYS.....	10
2.2 CORROSION OF ALUMINUM .....	12
2.2.1 Aluminum as a passive metal .....	14
2.2.2 Types of corrosion .....	15
2.2.3 The corrosion resistance of AA series .....	16
2.3 FILIFORM CORROSION ON COATED ALUMINUM .....	18

2.3.1	Mechanism of Filiform Corrosion .....	19
2.3.2	Effect of alloying elements on FFC Susceptibility of AAs .....	22
2.3.3	Effect of Surface Treatment on improving FFC Susceptibility of AAs .....	26
2.3.4	Filiform Corrosion Testing Methods .....	29
2.3.4.1	Accelerated exposure experiments .....	29
2.3.4.2	Electrochemical Evaluation.....	32
2.4	EXPERIMENTAL PROCEDURES.....	39
2.4.1	Materials and Chemicals.....	39
2.4.2	Methods.....	41
2.4.2.1	Microstructural characterization.....	41
2.4.2.2	Electrochemical measurements .....	42
2.5	ALLOYS CHARACTERIZATION .....	44
2.5.1	AA1100.....	45
2.5.2	AA2024 (Cu) .....	46
2.5.3	AA 3003 (Mn).....	48
2.5.4	AA 5052 (Mg).....	50
2.5.5	AA 6061 (Mg, Si).....	52
2.5.6	Alloy 7075 (Zn) .....	54
2.6	ELECTROCHEMICAL PARAMETERS OF FFC .....	58
2.6.1	Resistance to FFC initiation.....	59

2.6.2	Driving force for propagation .....	66
2.6.3	Kinetics of propagation.....	72
2.7	SUMMARY .....	76
CHAPTER 3 ELECTROCHEMICAL STUDY OF ANODIZED ALUMINUM FILIFORM CORROSION 78		
3.1	EXPERIMENTAL PROCEDURES.....	78
3.1.1	Materials and Chemicals.....	78
3.1.2	Methods.....	79
3.1.2.1	Samples preparation .....	79
3.1.2.2	Anodic film characterization .....	80
3.1.2.3	Electrochemical measurements .....	80
3.1.2.4	Accelerated exposure testing.....	81
3.2	ANODIC FILM CHARACTERIZATION.....	83
3.2.1	General observations.....	83
3.2.2	Anodic film morphology.....	84
3.3	ELECTROCHEMICAL PARAMETERS OF FFC .....	88
3.3.1	Resistance to FFC initiation ( $\Delta E_{PR}$ ).....	89
3.3.2	Driving force for propagation ( $\Delta E_{CORR}$ ) .....	92
3.3.3	Kinetics of propagation ( $i_{FFC}$ ) .....	95
3.3.4	Electrochemical measurements summary.....	98
CHAPTER 4 ACCELERATED EXPOSURE TEST .....		
		101

4.1	General observations.....	101
4.2	Results for AAs.....	104
4.2.1	Number of filaments (N).....	105
4.2.2	Length of filaments (L).....	106
4.3	Results for a-AAs.....	109
4.3.1	Number of filaments (N).....	110
4.3.2	Length of filaments (L).....	111
4.4	Accelerated exposure testing summary .....	112
CHAPTER 5 CONCLUSIONS AND FUTURE WORK .....		114
5.1	Conclusions.....	114
5.2	Future Work .....	115
REFERENCES .....		117

# LIST OF TABLES

<b>Table 2-1.</b> AAs designation system and applications. ....	11
<b>Table 2-2.</b> Corrosion resistance of AA series in various environments. ....	16
<b>Table 2-3.</b> Summary of effect of alloying elements on FFC of Al alloys. ....	25
<b>Table 3-1.</b> Chemical Composition (wt. %) of the investigated specimens. ....	41
<b>Table 3-2.</b> List of etchants used in the microstructure revealing. ....	42
<b>Table 3-3.</b> Summary characterization and testing methods used. ....	44
<b>Table 3-4.</b> Summary of the matrix composition and IMPs obtained by EDS point base analysis at different locations for each alloy. ....	57
<b>Table 3-5.</b> Electrochemical parameters of FFC. ....	59
<b>Table 3-6.</b> $E_{\text{pitting}}$ , $E_{a, \text{corr}}$ and $\Delta E_{\text{PR}}$ of AAs from PDP curves in $\text{N}_2$ -deaerated anolyte. ....	61
<b>Table 3-7.</b> Summary OCP evolution trend during 5h of immersion in $\text{N}_2$ de-aerated anolyte [40], [192], [112], [191], [188]. ....	69
<b>Table 3-8.</b> $i_{\text{FFC}}$ and $i_{\text{corr}}$ measured in the anolyte by the extrapolation of the cathodic branch method. ....	75
<b>Table 3-9.</b> Electrochemical parameters of FFC for the AAs evaluated. ....	77
<b>Table 4-1.</b> Accelerated exposure test evaluated specimens. ....	81
<b>Table 4-2.</b> Average defect size ( $\mu\text{m}^2$ ), defect density ( $\mu\text{m}^{-2}$ ) and percentage of the defect area calculated for a-AA samples. ....	85
<b>Table 4-3.</b> $E_{\text{pitting}}$ , $E_{a, \text{corr}}$ and $\Delta E_{\text{PR}}$ of a-AAs from PDP curves in $\text{N}_2$ -deaerated anolytes. ....	90
<b>Table 4-4.</b> Averaged $E_{c, \text{corr}}$ and $\Delta E_{\text{corr}}$ values of the evaluated a-AAs at room temperature. ....	94
<b>Table 4-5.</b> $i_{\text{FFC}}$ of a-AAs from PDP curves in $\text{N}_2$ -deaerated anolyte. ....	97

**Table 4-6.** Averaged N values of AAs after 1000h accelerated exposure testing (80 % RH, 40 °C).  
..... 106

**Table 4-7.** Averaged N values of a-AAs after 1000h accelerated exposure testing (80 % RH, 40 °C).  
..... 111

# LIST OF FIGURES

<b>Figure 1-1.</b> Electrochemical processes during FFC in coated Al [20].	3
<b>Figure 2-1.</b> Sketch graph of properties of the different AA series.	12
<b>Figure 2-2.</b> Sketch of an electrochemical corrosion cell.	13
<b>Figure 2-3.</b> Depiction of (a) uniform corrosion and (b) localized corrosion on Al.	15
<b>Figure 2-4.</b> Effects of principal alloying elements on electrolytic solution potential of Al. Image courtesy of J.R. Davis [27].	17
<b>Figure 2-5.</b> FFC filament observed on AA3003 with a clear film of epoxy coating after 1000h at 40 °C and 80 % RH.	19
<b>Figure 2-6.</b> Schematic diagram showing the process of FFC initiation on organic-coated Al.	20
<b>Figure 2-7.</b> Schematic diagram showing the process of FFC propagation on organic-coated Al.	21
<b>Figure 2-8.</b> Schematic diagram showing FFC filament growing on organic-coated Al.	22
<b>Figure 2-9.</b> Schematic anodizing process of Al.	29
<b>Figure 2-10.</b> Schematic illustration of the AA surface with natural oxide films.	33
<b>Figure 2-11.</b> Schematic representation of polarization curves (semi-logarithmic) in anolyte (blue) and catholyte (red) with their respective reactions and their correspondence within an FFC filament.	35
<b>Figure 2-12.</b> Schematic representation of polarization curves in anolyte and catholyte in semi-logarithmic coordinates. Graphic calculation of passive range is also shown.	36

**Figure 2-13.** Schematic representation of polarization curves in the anolyte and catholyte in semi-logarithmic coordinates. Graphic calculation of (a) tendency to propagation and (b) FFC current density. .... 37

**Figure 3-1.** Radar chart of selected AAs and their main alloying elements. .... 40

**Figure 3-2.** Conventional three-electrode cell used for electrochemical measurements. The experimental parameters are also listed. .... 43

**Figure 3-3.** OM Images of AA1100 (a) as polished and (b) after etching using Keller’s reagent for 15s. .... 45

**Figure 3-4.** (a) BSE-SEM imaging for as polished AA1100 and (b) EDS maps of Al (red) and Fe (green) distribution on the framed area. .... 46

**Figure 3-5.** OM Images of AA2024 (Cu) (a) as polished and (b) after etching using Keller’s reagent for 10s. .... 47

**Figure 3-6.** (a) BSE-SEM imaging for as polished AA2024 (Cu) and (b)EDS maps of chemical elements distribution on the framed areas showing Al-Cu-Mg as rounded dark IMPs and Al-Cu-Fe-Mn as irregularly shaped bright IMPs. .... 48

**Figure 3-7.** OM Images of AA3003 (Mn) (a) as polished and (b) after etching using Weck’s reagent for 15s. .... 49

**Figure 3-8.** (a) BSE-SEM imaging for as polished AA3003 (Mn) and (b) EDS maps of chemical elements distribution on the framed areas showing Al-Fe-Mn as the elongated IMPs and Al-Fe-Mn-Si as the irregular shaped IMPs. .... 50

**Figure 3-9.** OM Images of AA5052 (Mg) (a) as polished and (b) after etching using Weck’s reagent for 20 s. .... 51

**Figure 3-10.** (a) BSE-SEM images of as polished AA5052 (Mg) and (b) EDS maps of chemical elements distribution on the framed areas showing gray Fe-containing IMPs and black Mg<sub>2</sub>Si IMPs..... 52

**Figure 3-11.** OM Images of 6061 (Mg) (a) as polished and (b) after etching using Weck's reagent for 15s. .... 53

**Figure 3-12.** (a) BSE-SEM image of as polished AA6061 (Mg, Si) and (b) BSE micrograph EDS maps of chemical elements distribution showing bright Fe-containing IMPs and dark Mg<sub>2</sub>Si.... 54

**Figure 3-13.** OM Images of AA7075 (Zn) (a) as polished and (b) after etching using Keller's reagent for 10s..... 55

**Figure 3-14.** (a) BSE-SEM image of as polished AA7075 (Zn) and (b) EDS maps of chemical elements distribution showing bright Al-Cu-Fe containing IMPs and dark Mg<sub>2</sub>Si..... 56

**Figure 3-15.** Summary of E<sub>corr</sub> distribution of IMPs in a standard 0.1M NaCl, H<sub>2</sub>O<sub>2</sub> solution [161], [112], [162]. .... 58

**Figure 3-16.** PDP curves of AAs in the N<sub>2</sub>-deaerated anolyte..... 61

**Figure 3-17.** Anodic branches from PDP curves of AAs in the N<sub>2</sub>-deaerated anolyte (denoted as A-). .... 64

**Figure 3-18.** Schematic representation of corrosion of the anodic IMPs Al<sub>2</sub>CuMg (left) and Mg<sub>2</sub>Si (right). .... 66

**Figure 3-19.** E<sub>corr</sub> evolution after 18000s of immersion in anolyte (denoted as A-) for the alloys (a) 1100, 2024(Cu), AA3003(Mn), 5052(Mg), 6061(Mg, Si) and 7075(Zn). .... 67

**Figure 3-20.** E<sub>corr</sub> evolution during 13800 s of immersion in catholyte (denoted as C-) for the alloys (a) 1100, 2024(Cu), AA3003(Mn), 5052(Mg), 6061(Mg, Si), and 7075(Zn). .... 70

**Figure 3-21.**  $E_{\text{corr}}$  and the driving force  $\Delta E_{\text{corr}}$  values of **AAs** in the  $N_2$ -deaerated anolyte and aerated catholyte. .... 71

**Figure 3-22.** Polarization curves of **AAs** obtained in the  $N_2$ -deaerated anolyte (denoted as A-), and in the aerated catholyte (denoted as C-) at 25 °C. FFC current density ( $i_{\text{FFC}}$ ) is taken as the intercept of the anodic and cathodic curves assuming an effective cathode/anode area ratio of 100..... 74

**Figure 3-23.** PDP curves of the specimens in the aerated at 25 °C..... 76

**Figure 4-1.** Process diagram of a-**AAs** preparation..... 80

**Figure 4-2.** (a) An epoxy coated **AA** before accelerated exposure testing, noted that the edges are covered and a scribe was made in the center of the disk, and (b) samples placed in a humidity chamber. .... 82

**Figure 4-3.** **AA2024** (Cu) after (a) electropolishing and (b) anodizing. .... 83

**Figure 4-4.** Formation and dissolution of an oxide layer on **AA7075** (Zn) during the electropolishing process in  $HClO_4$ :  $C_2H_5OH$  at 10 °C with a DC voltage of 8 V. .... 84

**Figure 4-5.** Surface SE-SEM images of anodic films for a-**AAs** (a) 1100, (b) 2024 (Cu), (c) 3003 (Mn), (d) 5052 (Mg), (e) 6061 (Mg, Si) and (f) 7075 (Zn)..... 86

**Figure 4-6.** Superposed images of SE (yellow) and BSE (blue) SEM micrographs after contour image processing for (a) a-**AA2024** (Cu) and (b) a-**AA3003**(Mn)..... 87

**Figure 4-7.** PDP curves of (a) **AAs** and (b) a-**AAs** in  $N_2$ -deaerated anolytes (denoted as A-).... 90

**Figure 4-8.** Estimated  $\Delta E_{\text{PR}}$  for a-**AAs** (blue) and **AAs** in  $N_2$ -deaerated anolyte. .... 91

**Figure 4-9.**  $E_{\text{corr}}$  values of a-**AAs** (blue half symbols) in the anolyte (circle characters) and catholyte (square characters).  $E_{\text{corr}}$  values for **AAs** (black full symbols) are also displayed..... 92

**Figure 4-10.**  $\Delta E_{\text{corr}}$  values of a-**AAs** (blue) and **AAs** calculated as  $E_{\text{c, corr}} - E_{\text{a, corr}}$  from PDP measurements in simulated anolytes and catholytes..... 95

**Figure 4-11.** Polarization curves of AA (black) and a-AA (blue) samples were obtained in N<sub>2</sub>-deaerated anolytes (denoted as A-), and in aerated catholytes (denoted as C-) at 25 °C. FFC current density ( $i_{FFC}$ , A/cm<sup>2</sup>) is taken as the intercept of the anodic and cathodic curves assuming an effective cathode/anode area ratio of 100. .... 96

**Figure 4-12.**  $i_{corr}$  values for a-AA (blue) and AA (black) samples calculated as the intercept of the anodic and cathodic PDP curves. .... 98

**Figure 4-13.** Graph of  $E_{PR}$  changing factors and  $E_{corr}$  and  $i_{FFC}$  decreasing factors for AAs after anodizing. .... 100

**Figure 4-14.** Development of FFC from a scribe on AA 3003(Mn) (a)(b)(c) and a-AA 3003(Mn) (e)(f)(g) after 1 week, 3 weeks and 6weeks of accelerated exposure testing. .... 102

**Figure 4-15.** OM images of an isolated FFC filament after 1000 h accelerated exposure to 80 % RH at 40 °C before (a) and after (b) removing the epoxy coating and corrosion products were washed on AA 2024 (Cu) samples. .... 103

**Figure 4-16.** Images of epoxy coated AAs 1100, 2024 (Cu), 3003(Mn), 5052 (Mg), 6061 (Mg, Si) and 7075 (Zn) with scribes after 1000 h accelerated exposure to 80 % RH at 40 °C. .... 105

**Figure 4-17.** OM images on the scribe area of epoxy coated AAs (a) 1100, (b) 2024 (Cu), (c) 3003 (Mn), (d) 5052 (Mg), (e) 6061 (Mg, Si) and (f) 7075 (Zn) after 1000h accelerated exposure to 80 % RH at 40 °C. .... 107

**Figure 4-18.** (a) Filament length (L) distribution on AAs, and (b) the relation between the  $i_{FFC}$  and L. .... 109

**Figure 4-19.** Images of epoxy coated a-AAs 1100, 2024 (Cu), 3003(Mn), 5052 (Mg), 6061 (Mg, Si) and 7075 (Zn) with scribes after 1000 h accelerated exposure to 80 % RH at 40 °C. .... 110

**Figure 4-20.** Relation between the  $i_{corr}$  and L for a-AA samples. .... 112

**Figure 4-21.** Summary of N (a) and L (b) values for AA and a-AA samples..... 113

# LIST OF ABBREVIATIONS

AAs:	Aluminum alloys
a-AAs:	Anodized aluminum alloys
AASS:	Acetic acid salt spray
Al:	Aluminum
BSE:	Backscattered electrons
CE:	Counter electrode
EC:	Electrochemical
EDS:	Energy-dispersive X-ray
FFC:	Filiform corrosion
IMPs:	Intermetallic particles
OCP:	Open circuit potential
OM:	Optical microscopy
PDP:	Potentiodynamic polarization
RE:	Reference electrode
RH:	Relative humidity
SE:	Secondary electrons
SEM:	Scanning electron microscopy
WE:	Working electrode

# LIST OF SYMBOLS

Symbol	Description	Units
$\text{Cl}^-$	Chloride ions	–
E	Potential	V
$E_{a, \text{corr}}$	Corrosion potential in anolyte	V
$E_{c, \text{corr}}$	Corrosion potential in catholyte	V
$E_{\text{pitting}}$	Pitting potential	V
i	Current density	$\text{A}/\text{cm}^2$
$i_{\text{corr}}$	Corrosion current	$\text{A}/\text{cm}^2$
$i_{\text{FFC}}$	Filiform current	$\text{A}/\text{cm}^2$
L	Filament length	mm
N	Number of filaments	$\text{cm}^{-1}$
$\Delta E_{\text{corr}}$	Corrosion potential	V
$\Delta E_{\text{corr}}$	Driving force for FFC propagation	V
$\Delta E_{\text{PR}}$	Passive range	V

# CHAPTER 1 INTRODUCTION

## 1.1 RESEARCH BACKGROUND

With the dramatic increase of aluminum (Al) production in the last century (from 6 kT in 1900 to 134400 kT in 2021) [1], the understanding of Al corrosion plays an important role in multiple industries involved in the manufacture and application of Al products. In fact, the costs of corrosion on the most abundant metal on the earth (Al) imply serious economic losses, safety hazards and important environmental impacts [2], [3], [4]. Therefore, it is not surprising that efforts from governments, industries, and scientific communities are joined against the corrosion and deterioration of Al products. Currently, one of the most common corrosion control methods, especially for Al alloys (AA) and steels, involves the application of organic coatings on the metal surface, providing a barrier between the bare metal and the corrosive environment [5]. These organic layers improve Al's aesthetic appearance and maintain its durability when exposed to weather, humidity, abrasion, or chemicals [6]. Under these conditions, there have been several reports on a form of localized corrosion between the metal surface and its organic coating, known as filiform corrosion (FFC) [7]. Its distinctive worm-like pattern has been found to be a consequence of reaction products left behind by a moving active point due to corrosion [8]. Even though some authors describe it as just an aesthetic problem, previous studies suggest that FFC causes the breakdown of the coating compromising its integrity and exposing the bare metal to environmental conditions [9].

The term FFC was first introduced in 1944 by C. F. Sharman, who reported the production and growth of hair-like corrosion tracks on coated steels exposed to atmospheres containing acetic acid and water vapour [10]. However, it was not until 1969 that a study of FFC on coated Al was published by Michiki H and Toshio S [11]. Since then, the increased use of painted Al on a variety of applications has accelerated the occurrence of FFC and has initiated an extensive research activity to improve FFC resistance of Al finishes. The aircraft industry has reported the recurrent incidence of FFC on external tanks of airplanes; these tanks are usually made of AA 6061 coated with epoxy or polyurethane paint. Interestingly, this problem was observed mostly in planes with hot and humid routes close to the Mediterranean [12]. FFC has also been identified on Al structures on buildings exposed to marine atmospheres. A. Bautista identified edges, vent frames and cutoff lines to be the most markedly affected zones [13]. Bike frames [14], PVC coated Al cans [15] and body cars [16] have also been the study objects due to FFC incidents.

The FFC process consists of three steps, initiation, propagation, and growth. The main driving force triggering the FFC process is believed to be a differential aeration cell that results in a potential difference and the subsequent separation of anodic and cathodic sites with an uneven level of oxygen [17]. As seen in **Figure 1**, two parts of the filament have been identified: an active head that acts as an electrochemical cell and a dry tail made of corrosion products. Al dissolution takes place in the front of the head (relatively deaerated anodic site); pH measurements have indicated that the active heads of the filaments develop an acidic pH ( $1 < \text{pH} < 2$ ) [18]. The cathodic reaction is expected to be oxygen reduction, leading to the formation of hydroxide ions. A wide range of pH values ( $3 < \text{pH} < 11$ ) has been reported for the cathodic site [19].

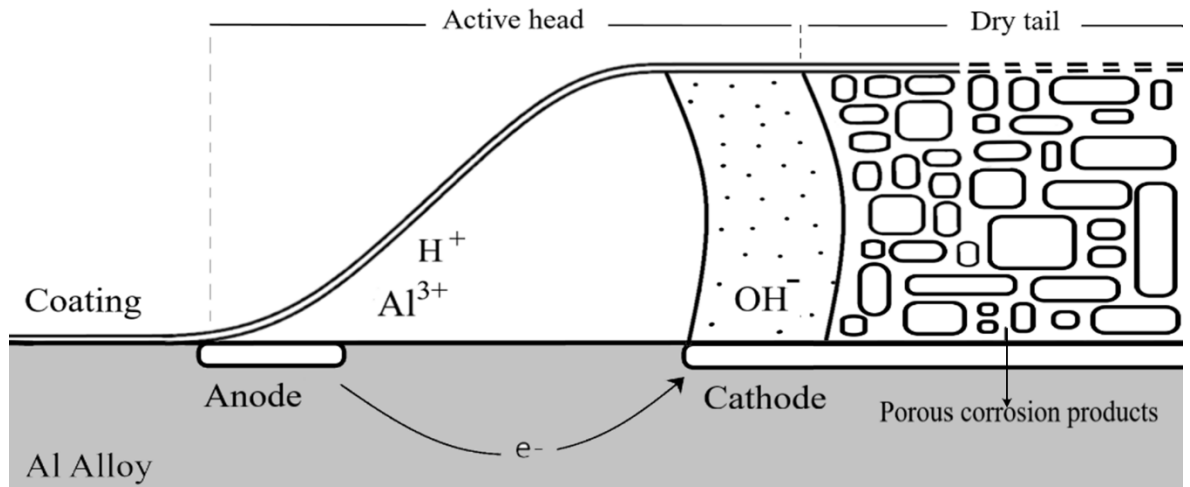


**Figure 1-1.** Electrochemical processes during FFC in coated Al [20].

A variety of accelerated experimental methods have been designed to predict the sensitivity of a system to FFC. Filaments have been satisfactorily replicated in laboratories through standard tests including acetic acid salt spray (AASS) test, Lockheed Test [21] and FFC test [22]. Although these conventional methods provide a qualitative analysis of the filaments on coated metals, they offer limited information on mechanisms and kinetics. For this reason, electrochemical techniques have been established to obtain a better understanding of the FFC phenomenon and its mechanisms. Particularly, potentiodynamic polarization (PDP) analyses are often conducted to evaluate the initiation and propagation stages of FFC on AAs [23].

Over the years, the determination of factors that affect FFC on AAs has been a common topic in numerous conferences and publications. Whereas the nature of the coating does not seem to influence FFC of AAs [24], it has been reported that the composition of the alloys and more particularly the presence of intermetallic particles (IMPs) is an important parameter on FFC susceptibility of Al painted products. Considering this criteria, most homogenous single-phase

solid solutions are not vulnerable to FFC, as it usually does not involve the presence of an electrochemically different second phase. This was confirmed by Afseth, who examined the influence of alloying elements and microstructures on the FFC response of super-purity-based binary model alloys of the Al-Mg, Al-Mn, Al-Fe [25]. Most of the coated commercial AAs exposed to humid environments are susceptible to FFC due to the presence of a strengthening second phase [26] and its degree of susceptibility seems to depend on their main alloying elements [12]. On the other hand, several authors agree that a distinction must be made between the FFC susceptibility of the bulk metal and that of the surface layer. Therefore, the surface treatment seems to be another crucial factor in the FFC performance of coated metals as many researchers found variations in quantity and length of filaments on metals under different pre-treatments [27]. For instance, anodizing is an electrochemical technique used to enhance FFC resistance of AA by thickening its natural oxide layer which delays the development of FFC initiation points. The above was observed on the AAs 3005, 3103 and 3063 [28].

In a word, environmental influence, the composition of AA substrates, and the pre-coating surface treatment are the critical factors influencing the FFC susceptibility of AA. The FFC susceptibility of AAs with coatings has been widely investigated in controlled environmental chambers with widely accepted standards. Nevertheless, there is a lack of electrochemical studies focusing on FFC mechanisms and on clarifying the roles of alloying elements on the FFC susceptibility of commercially used AAs.

## 1.2 PROBLEM STATEMENT

To minimize the occurrence of FFC on painted AAs, it is crucial to understand the mechanisms involved in the filament initiation and propagation, as well as the influence of parameters that can be easily controlled in the manufacture and processing of Al finished products. Al metallurgy is advanced by leaps and bounds and provides a wide range of options among the eight series of AAs with the ability to fulfil a diverse range of needs and applications (It is important to emphasize that AA series are classified based on their main alloying element as it will be discussed in section 2.1). However, this variety may cause some confusion and lead to an unappropriated selection of material, in particular with respect to the FFC resistance. Preceding research has tended to focus on evaluating the influence of certain elements on a specific alloy series or pure binary systems with no industrial application, which causes considerable uncertainty with regard to comparison and categorization of FFC resistance of commercial AA series and the influence of alloying elements on their behaviour. For instance, it has been suggested that coated AA containing copper (Cu) exhibits the worst resistance against FFC because bare Al-Cu alloys are known to corrode very easily in comparison to the other series. However, J. H. Powers found that the FFC behaviour of AA 6009 with 0.15-0.6 wt.% Cu was very similar to that of AA 2008 with 0.7-1.1 wt.% Cu [16]. Similarly, iron (Fe) and silicon (Si) contents have been reported to be detrimental for FFC resistance on the 1xxx [29], [30] and 3xxx AA series [31] respectively. Yet, there has been no attempt to compare the FFC performance of both series.

In addition, previous work has mostly focused on qualitative approaches to evaluate the FFC susceptibility. For instance, humidity exposure and AASS tests have been widely applied to evaluate the FFC of AAs. These methods are time-consuming (over thousands of hours) and

preclude significant information that could contribute to the fundamental understanding of the corrosion process. In contrast, electrochemical procedures are usually carried out in a few hours and provide important information. Various attempts have been made to correlate electrochemical work with exposure testing, but more in-depth research and comparative data are required before qualitative analysis can be confidently predicted by electrochemical methods.

### 1.3 RESEARCH OBJECTIVES

The present work aims to investigate the FFC of various AAs via electrochemical measurements and long-term humidity testing. A series of experiments are designed and performed to study the influence of alloying elements and anodizing as a pre-coating treatment on the FFC susceptibility of AAs in order to broaden current knowledge on the FFC of painted AAs. The specific objectives are addressed below:

- (1) To study the effects of alloying elements on the FFC behaviour of AAs. Electrochemical measurements are performed on AA substrates in bulk anolyte and catholyte solutions at room temperature. Three electrochemical factors, including the resistance to FFC initiation, the driving force for propagation, and the FFC current density, are introduced and defined. Besides, a large number of OM images, SEM and EDS are taken and related to results from electrochemical measurements to generate FFC dataset and trends.
  
- (2) To identify the influence of anodizing as the pre-coating treatment on the FFC susceptibility of various AAs. In order to reveal the influence of anodizing, the same electrochemical measurements done on the bare AAs are performed on the anodized specimens. Together with surface characterization, electrochemical investigation offers a clear understanding of the FFC mechanisms of AAs with and without anodizing.

(3) To corroborate and validate the trends observed in the electrochemical experiments.

Accelerated humidity tests are performed. Filament density and average filament length are calculated and correlated to the electrochemical FFC parameters.

In the end, it is expected that advances in the understanding of FFC mechanisms could be implemented in commercial or research codes in the near future, benefiting all research communities involved in Al manufacturing and coating.

## 1.4 THESIS OUTLINE

**Chapter 1** presents the research background, problem statement, and specific objectives of this dissertation.

**Chapter 2** reviews the common commercial AAs in terms of alloying elements, and current methodologies, progress, and knowledge gap on FFC research and FFC of AAs.

**Chapter 3** presents an electrochemical study of FFC on 6 commercial AAs, including detailed experimental procedures, AAs characterization, and interpretation of results.

**Chapter 4** compares the electrochemical FFC behaviour of the selected AAs after three steps anodizing with results from Chapter 3, including detailed experimental procedures, anodic film characterization, and interpretation of results. In addition, it presents the long-term accelerated exposure tests on coated AAs with and without anodizing as the pre-coating surface treatment; also correlates these results with electrochemical parameters from Chapters 3 and 4.

**Chapter 5** exclusively summarizes experimental findings and provides recommendations for future works.

# CHAPTER 2 LITERATURE REVIEW

## 2.1 ALUMINUM AND ITS ALLOYS

Aluminum (Al) is the most abundant metal and the third most prevalent element on the Earth's surface [32]. With an annual global consumption of 134.4 million tons in 2020, it is considered the leader in the metallurgy of non-ferrous metals [33]. The breakthrough of new applications for Al and its alloys, along with their increasing demand, can be linked to Al's outstanding properties such as favorable mechanical strength, low density, and excellent workability, which are decisive criteria for material selection in many fields including transportation, construction, and packaging. Historical figures indicate that Al demand is expected to increase by about 80 % by 2050 [1].

In terms of properties, lightness is the most remarkable characteristic of Al. The density of its alloys range between  $2,640 \text{ kg/m}^3$  and  $2,810 \text{ kg/m}^3$  (one-third the weight of commonly used steels) [34]. The implications of its low weight on structures and moving parts are innumerable and benefit both the properties of the final product and the operational conditions involved in its manufacturing (which saves energy, reduces carbon footprint, decreases inertia and vibration, lowers shipping and assembly costs, etc.) [35]. In general terms, pure Al is soft, ductile, and has limited structural utility in industrial applications. Therefore, alloying elements must be added to Al to promote solid solution hardening and stimulate the development of a second strengthening phase, which enhances the material's mechanical properties and usefulness [36][37]. The most common alloying elements are copper (Cu), manganese (Mn), silicon (Si), magnesium (Mg) and zinc (Zn); In most cases, other elements are added in lower quantities (less than 1 wt.%) to meet specific needs.

Aluminum alloys (AAs) are traditionally classified into 8 main groups according to their principal alloying element as listed in **Table 2-1** [38].

**Table 2-1.** AAs designation system and applications.

AA series	Principal Alloying Element	Applications
1XXX	99 wt.% Al	Heat exchangers
2XXX	Cu	Construction of aircraft and spacecraft, mechanical applications
3XXX	Mn	Building, outdoor installations and urban amenities
4XXX	Si	Welding and brazing wire
5XXX	Mg	Building, outdoor installations and urban amenities, shipbuilding, mechanical applications
6XXX	Mg, Si	Building, outdoor installations and urban amenities, shipbuilding, mechanical applications
7XXX	Zn	Construction of aircraft and spacecraft, mechanical applications
8XXX	Other Elements	Specific applications

AAs that are part of the same family display a group of similar characteristics such as castability, mechanical properties, corrosion resistance and others [12]. These properties may vary considerably from one series to another. **Figure 2-1** shows the variation of some properties through different AA series [39], [40], [41]. AAs series are divided into two groups: age-hardenable, which

include the series 2XXX, 6XXX and 7XXX, and strain-hardenable, such as 1XXX, 3XXX and 5XXX. In general, age-hardenable series are heat treatable and receive a T-temper while strain-hardenable series obtain their strength through cold deformation and received H-tempers [37]. The alloying elements and microstructural features developed during solidification, processing, and heat treatment determine the performance and properties of Al final products. [42]. From now, throughout this thesis, the terms Al and AAs are used interchangeably.

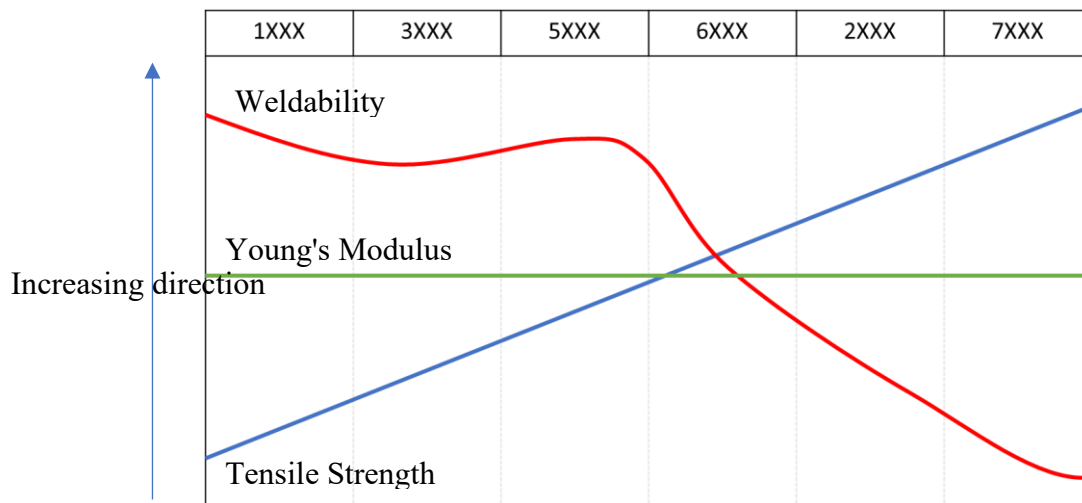


**Figure 2-1.** Sketch graph of properties of the different AA series.

*These tendencies are approximations from the literature and are used only for comparison purposes.*

## 2.2 CORROSION OF ALUMINUM

In most environmental conditions, the corrosion of Al, as well as other common metals, is the result of the development of an electrochemical cell composed of an anode where the oxidation of the metal atoms occurs, a cathode where chemicals species are reduced, a potential difference between the two sites that drive the cell and metallic and electrolytic paths between the anode and

cathode [43]. The depiction of the described electrochemical cell is shown in **Figure 2-2**. In atmospheric corrosion, the electrolyte is believed to be formed by a thin film of moisture adsorbed on the metal surface [44] and the potential difference is attributed to differences between the characteristics of different metals, surface conditions, chemical concentrations, and the environment [43].

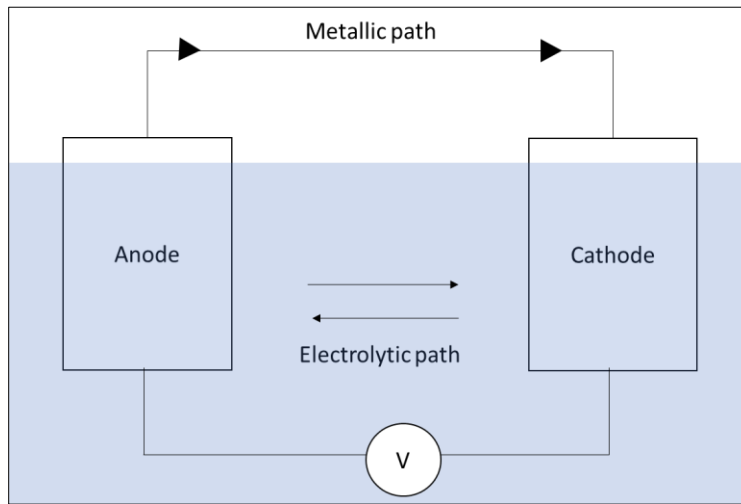


**Figure 2-2.** Sketch of an electrochemical corrosion cell.

The corrosion of Al in aqueous media is a consequence of the following electrochemical reactions [12][45]:



The oxidation reaction is balanced by a simultaneous reduction in ions present in the solution:





### 2.2.1 Aluminum as a passive metal

Even though Al is a very reactive metal, it exhibits relatively good corrosion resistance. This is due to a phenomenon first described by Joseph W. Richards in 1896 known as passivity. Joseph W. et al. [46] observed and reported a “thin film with a dead appearance” on Al products after long exposure times. The free energy of the Al oxidation reaction is  $-1,675 \text{ KJ.mol}^{-1}$ [45], which indicates that Al has a high reactivity towards oxygen and a prominent tendency towards the spontaneous growth of a uniform natural oxide film according to the reaction:



Thus, the corrosion resistance of Al is subjected to the stability of the natural oxide film formed on its surface [47]. Studies have found that if the oxide film is physically or chemically damaged, it will be reconstructed almost immediately (within milliseconds) if the environment is favourable [48]. However, if the film is not stable, the dissolution of Al will take place. Extensive research and thermodynamic calculations show that passivation of pure Al occurs in a pH range from 6 to 8 in pure water at 25 °C [49] but years of Al usage have shown that the composition of the AA significantly modifies the natural film behaviour. A clear example of this was the research carried out by Ph. Gimenez who collected several experimental data and sketched the Pourbaix diagram of AA 5086. They concluded that the film exhibited stability with a pH range from 1 to 10 [50]. That said, the composition of AAs highly influences the stability of the oxide film and thus controls the type and severity of corrosion on Al under specific media [51].

## 2.2.2 Types of corrosion

Corrosion on Al can be divided into two main categories: uniform and localized corrosion. Both types of corrosion are represented in **Figure 2-3**. Uniform corrosion occurs only when AAs are exposed to highly acidic or alkaline mediums in which the natural oxide film is soluble. In this kind of corrosion, the cathodes and anodes are located randomly and alternate with time. Therefore, reactions (2-2), (2-3) and/or (2-4) take place in a "uniform" manner as there is no preferential site or location for cathodic or anodic reactions, which results in a uniform loss of dimension [52]. On the other hand, localized corrosion is the most common form of corrosion on AAs. It begins with the breakdown of weak spots in the oxide film and targets specific areas of the metal surface according to several parameters related to the alloy composition, the environment, and the operating conditions [3]. Localized corrosion can be further divided into several types: pitting, crevice, intergranular, FFC, etc.

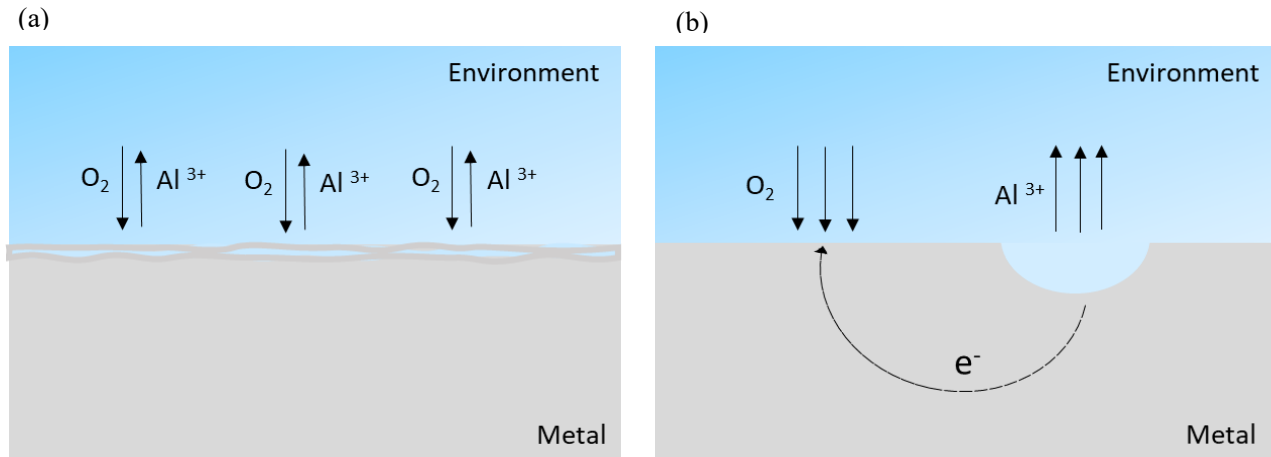


**Figure 2-3.** Depiction of (a) uniform corrosion and (b) localized corrosion on Al.

### 2.2.3 The corrosion resistance of AA series

As mentioned earlier, AAs that are part of the same series display a group of similar characteristics including corrosion resistance. Chemical composition has been recognized as one of the main parameters governing the intensity and type of corrosion on AAs [53], [54]. Overall, AAs from the 5XXX series have the best resistance to atmospheric corrosion of all the AAs, in contrast to the 2XXX and 7XXX series that exhibit the worst corrosion resistance in most environments. **Table 2-2** compares and summarizes the rankings of resistance to corrosive deterioration given from different references in various environments.

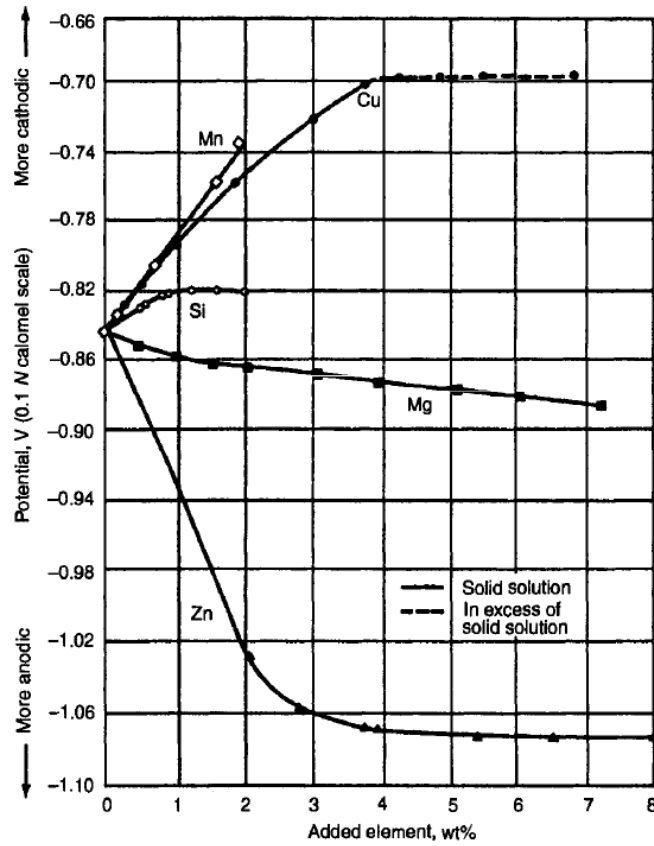
**Table 2-2.** Corrosion resistance of AA series in various environments.

AA series	Corrosion Resistance		
	[55] <sup>a</sup>	[56] <sup>b</sup>	[12] <sup>c</sup>
1XXX	Moderate	Good	Good
2XXX	Poor	Poor	Poor
3XXX	Moderate	Good	Good
5XXX	Good	Good/Moderate	Good
6XXX	Good	Good/Moderate	Moderate
7XXX	Poor	Poor	Poor

- a. *From weight-loss studies conducted in a marine environment.*
- b. *Relative ratings based on exposure to sodium chloride solution by intermittent spraying and immersion.*
- c. *Localized corrosion resistance of the metal in a natural environment: air, freshwater, seawater*

Certain elements affect the corrosion resistance of AAs by modifying the properties of the natural oxide film. Alloying elements such as Cu and Zn have been identified to weaken the protective properties of the oxide film. Further explanation regarding the effect of alloying elements on the natural oxide film is given in section 2.3.2.

The effect of alloying elements on the corrosion resistance of AAs varies significantly according to their state in the metal structure. They could be either in solid solution and/or part of intermetallic particles (IMPs). As illustrated in **Figure 2-4**, the presence of alloying elements in solid solution causes significant variations in the corrosion potential ( $E_{\text{corr}}$ ) of Al.



*Note: The potentials reported are for high purity binary alloys solution heat-treated and are measured in a solution of 53 g/L NaCl + 3 g/L H<sub>2</sub>O<sub>2</sub> at 25°C.*

**Figure 2-4.** Effects of principal alloying elements on electrolytic solution potential of Al. Image courtesy of J.R. Davis [27].

When the alloying elements are part of IMPs, their influence on the corrosion behaviour of AAs is dependant on the electrochemical properties of the IMPs that they consist of. The main IMPs occurring in AAs in descending order (from the highest to the lowest  $E_{\text{corr}}$ ) are:  $\text{Al}_3\text{Fe}$ ,  $\text{Al}_2\text{Cu}$ ,  $\text{Al}_7\text{Cu}_2\text{Fe}$ ,  $\text{Al}_6\text{Mn}$ ,  $\text{Al}_2\text{CuMg}$ ,  $\text{MgZn}_2$  and  $\text{Mg}_2\text{Si}$  [57]. When the potential of the matrix differs considerably from that of the IMPs, micro-galvanic coupling can occur and promote different forms of localized corrosion [58]. IMPs can be either anodic or cathodic with respect to the matrix. Cathodic IMPs exhibit a higher  $E_{\text{corr}}$  than that of the matrix, causing the dissolution of the surrounding matrix. In contrast, anodic IMPs have a lower  $E_{\text{corr}}$  than that of the matrix which causes their own dissolution. Among all possible types of localized corrosion, FFC is a special concern for coated AAs, as it causes the breakdown of the coating, compromising its integrity and exposing the bare metal to environmental conditions [9].

### **2.3 FILIFORM CORROSION ON COATED ALUMINUM**

FFC is a type of localized atmospheric corrosion that commonly occurs on painted metals (such as steels, Mg, and Al [18]). It has a very distinct pattern of attack: fine thread-like filaments that do not cross each other, arising from pre-existing defects on the coating surface [59]. FFC propagates through paths of low resistance; lines of IMPs have been determined as favourable paths [18]. FFC filaments consist of an electrolyte-filled active head and a dry tail made of corrosion products [60]. Numerous investigations have identified three necessary conditions to generate FFC on painted Al: the presence of oxygen, aggressive ions (e.g.,  $\text{Cl}^-$ ), and high relative humidity (RH) [61]. This also explains why FFC is mainly observed on products exposed to marine and industrial atmosphere [14].

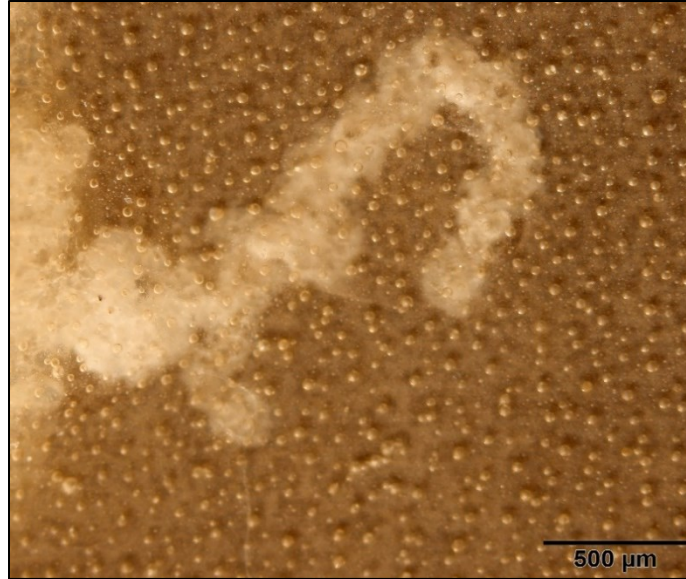


**Figure 2-5.** FFC filament observed on AA3003 with a clear film of epoxy coating after 1000h at 40 °C and 80 % RH.

### 2.3.1 Mechanism of Filiform Corrosion

After years of study, the anodic undermining mechanism was proposed in order to explain FFC on AAs [23]. The anodic undermining process consists of three steps: FFC initiation, propagation, and filament growth. All steps are described in the following paragraphs.

**FFC Initiation.** It is known that FFC initiates at defects on the coating due to salt and water accumulation that causes the development of an aqueous electrolyte capable of supporting corrosion [62]. As stated by V. Dumitrascu, the natural oxide film is under a constant cycle of breaking down and repairing. In unaggressive environments, the damaged film can be restored immediately [63]. However, in the presence of a solution containing aggressive ions such as  $\text{Cl}^-$ , the dissolution rate overcomes the growth rate, which results in the failure of the Al oxide layer and allows  $\text{Cl}^-$  ions to target the exposed surface. Reactions (2-6) and (2-7) have been proposed as the chemical reactions occurring during the oxide film break down [64]. It is worth mentioning

that the natural oxide film on AAs contains mainly alumina ( $\text{Al}_2\text{O}_3$ ) and Al hydroxide ( $\text{Al}(\text{OH})_3$ ) [65]. As presented in **Figure 2-6**, defects on the coating thus, give place to localized corrosion initiation in the form of pits on coated Al with the possibility of propagating into FFC filaments.

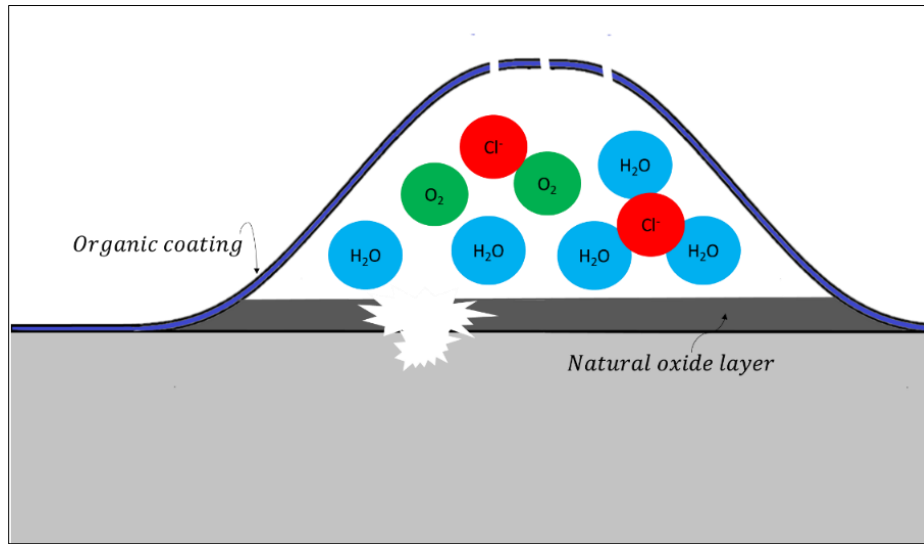
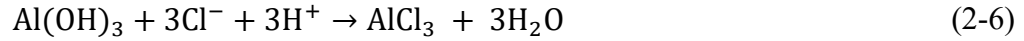


**Figure 2-6.** Schematic diagram showing the process of FFC initiation on organic-coated Al.

**Filament Propagation.** The propagation of an FFC filament from an initiation point is subjected to the presence of a more electrochemically noble site that promotes oxygen reduction when exposed to an aerated environment [18]. Al dissolution causes the acidification of the region according to reaction (2-8) and migration of  $\text{Cl}^-$  ions towards the anodic zone to preserve the electroneutrality of the cell [66]. Various surface characterization techniques have been applied to demonstrate that  $\text{Cl}^-$  ions are accumulated in the anodic zone (i.e., the filament head), and show a

very low concentration in the tail region [67]. Conversely, the reduction of oxygen in the cathode prevents the oxygen from reaching the anode and produces  $\text{OH}^-$  ions according to reaction (2-4), which results in an alkaline local area and an aeration gradient between the anodic and cathodic zones. As a result, two physically separated environments with opposing conditions (pH, aeration, and  $\text{Cl}^-$  concentration), anolyte and catholyte, coexist under the coating as represented in **Figure 2-7**.

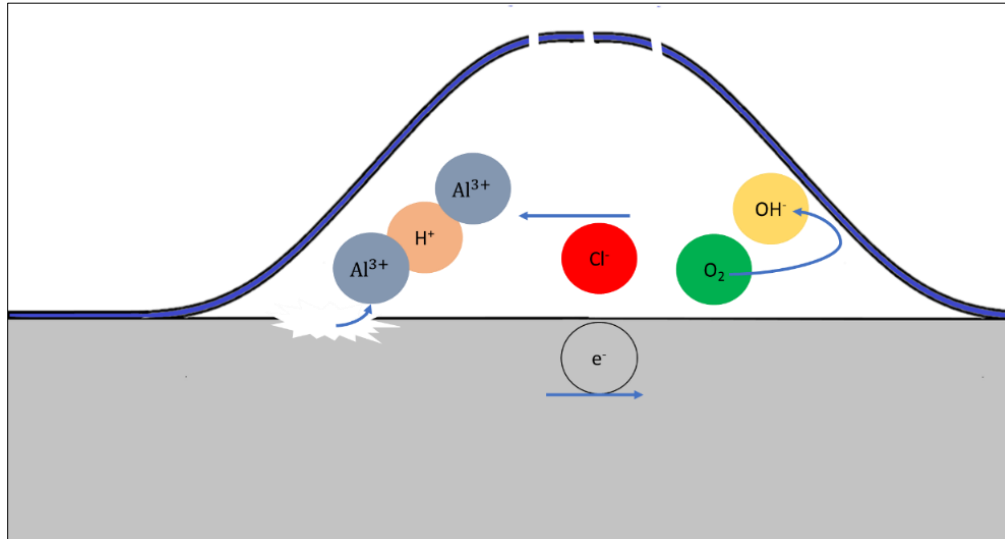
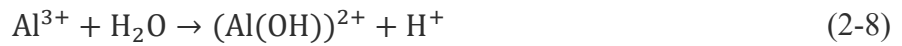


**Figure 2-7.** Schematic diagram showing the process of FFC propagation on organic-coated Al.

**Filament growth.** Upon growth and movement of the filament head, corrosion products from the Al oxidation are left behind and dried [67]. G.D. Steele reported the observation of a semipermeable membrane that separates the active head from the corrosion products. He described it as a humid layer filled with a very concentrated solution of salts that thwarts the migration of ions from the electrolyte in the head to the tail [68]. As the filiform head advances, the membrane

is renewed from solvated corrosion products and the previous membrane becomes dehydrated, which gives place to the dry tail, as shown in **Figure 2-8**. In a word, once initiated, corrosion filaments propagate and move away from the coating defect, due to the influence of an  $O_2$  and  $Cl^-$  concentration cell.

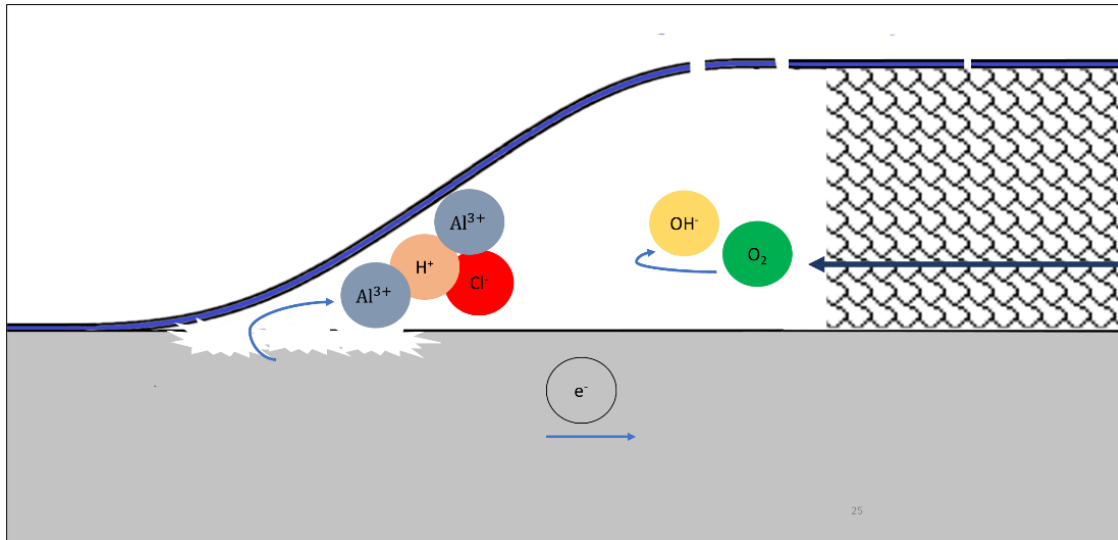


**Figure 2-8.** Schematic diagram showing FFC filament growing on organic-coated Al.

### 2.3.2 Effect of alloying elements on FFC Susceptibility of AAs

In general, AAs are not homogeneous. They consist of a matrix rich in alloying elements and IMPs distributed in the matrix and at the grain boundaries. Their activity for cathodic reduction of oxygen varies considerably with the presence of alloying elements. Pure Al, for example, has been reported to be practically inactive as an oxygen cathode [69]. This passive behaviour is often attributed to the properties of the native Al oxide that, as an electrical insulator with a wide bandgap, disfavors interfacial electron transfer [18]. Alloying elements affect not only the electrochemical properties of the metal surface, but also influence the structural characteristics of

its naturally formed oxide film. Therefore, all three stages of FFC on AAs are expected to be strongly influenced by the AAs' composition.

As mentioned in previous paragraphs, the initiation stage of FFC is linked to the structure and composition of the native film. Specific elements have been identified to boost the protective properties of the oxide film by the formation of mixed oxides. For example, the exceptional corrosion resistance of Al-Mg alloys (5XXX series) is often attributed to the development of a very protective natural oxide layer containing Al and Mg in the form of MgO, Al<sub>2</sub>O<sub>3</sub> or MgAl<sub>2</sub>O<sub>4</sub>. This film nucleates and grows much more rapidly than the Al<sub>2</sub>O<sub>3</sub> is able to form in pure Al. Conversely, elements like Cu and Zn weaken the protective properties of the passive film by doping it, thus decreasing oxygen diffusivity, and slowing down Al<sub>2</sub>O<sub>3</sub> nucleation. Therefore, it is expected that AAs 5XXX exhibit higher resistance to FFC initiation than those with high content of Cu and/or Zn. The following paragraphs are a distillation of what is found in the literature regarding the effects of main alloying elements on Al FFC behaviour [70], [71].

**Copper.** Cu has been found to have a detrimental effect on the FFC properties in a number of papers through different techniques. For example, Van der Weijde et al. found that the FFC resistance of AA 2024 decreases as the Cu content increases, by exposure tests. To explain this trend, they performed polarization measurements in anolyte and catholyte solutions which were characteristic of the local anodic and cathodic sites in the filaments on the Al substrates and calculated the FFC current, defined as the intercept of the anodic and cathodic curves. It was found that FFC current increased with Cu concentration in the alloy [31]. Similarly, it was observed that the presence of Cu in solid solution significantly impairs the FFC resistance of AA 3005. Cu is

believed to be locally enriched on the surface during the corrosion process, thereby enhancing cathodic reactions and micro galvanic coupling with the adjacent Al-rich matrix [72]. Another study shows that binary Al–Cu alloys exhibited severe FFC in comparison with Al-Mn and Al-Mg binary alloys [25]. Authors attributed the detrimental effect of Cu in solid solution to a selective dissolution phenomenon during the corrosion process, whereby copper was locally enriched on the surface in the form of Cu-rich IMPs, providing efficient and active cathodic sites [73]. Additionally, the influence of Cu in pure Al resulted in the increase of FFC severity up to 6 wt.% of Cu, and the FFC resistance started rising again with 9 wt.% of Cu [26].

**Zinc.** The 7XXX series are very high-strength AAs with Zn as the primary alloying agent. AA 7075 was reported to have slower FFC propagation kinetics than AA 2024 after alkaline cleaning [74]. Furthermore, a correlation between Zn content and average FFC filament length was not observed in Al-Zn alloys [25], [31].

**Manganese and Iron.** The alloying elements Mn and Fe in the 3XXX series have been reported to influence the FFC behaviour of Al. A recent paper compared the performance of AA 3005 and AA 5754 by a combination of accelerated exposure tests and corrosion potential measurements. It was found that the AA 3005 exhibited a higher FFC resistance in comparison to AA 5754. After annealing, FFC resistance of AA 5754 did not display much variation, whereas a drastic increase in FFC susceptibility was observed on AA 3005. The author attributed this behaviour to the precipitation of high-density Al-Mn-Fe IMPs [75]. A deeper study on the influence of Fe on FFC resistance of AAs identified that  $\text{FeAl}_3$  IMPs acted as efficient sites for cathodic reactions, thus promoting FFC on the metal surface [29], [30]. Conversely, the precipitation of the phase  $\text{MnAl}_6$

does not affect the FFC response of the material due to its similar electrochemical properties to the Al-rich matrix [76]. Some researchers also observed that the Fe content did not significantly impact FFC behaviour of AA 3005 without annealing [72].

**Silicon and Magnesium.** Si is an element used in the 4XXX and 6XXX series. Usually, AAs with high Si content are more susceptible to FFC than those with low Si content. This tendency is attributed to the influence of Si on the precipitation of finely dispersed IMPS with a high population density that provides a large number of potential FFC initiation sites [77]. This is in contrast with Al-Mg binary alloys, which show no variation in average filament length with solute content up to 3.6 wt.%. [31]. Other studies have reported that Al-Mg binary AAs are not susceptible to FFC after 1000 h of accelerated FFC test [25].

**Table 2-3.** Summary of effect of alloying elements on FFC of Al alloys.

Alloying Element	AA	FFC Resistance	Observations	Ref.
<b>Cu</b>	2024	Decreases	Copper-rich IMPs provide efficient cathodic sites	[78]
	3005	Decreases		[72]
	6060	Decreases		[79]
	Al-Cu	Decreases		[25]
<b>Zn</b>	Al-Zn	Independent	-	[25]
	AA8006	Independent	-	[80]
	Al-Si-Mg	Independent	-	[81]
	3005 (annealed)	Decreases	IMPs	[75]

<b>Fe</b>	AA3005	Independent	-	[72]
	Al-Mn	Decreases	Precipitation of phase FeAl <sub>3</sub>	[30]
	1XXX	Decreases	Precipitation of phase FeAl <sub>3</sub>	[29]
<b>Mn</b>	Al-Mn	Independent	MnAl <sub>6</sub> similar electrochemical properties to Al	[30]
	3005	Decreases	Secondary IMPs	[31]
<b>Si</b>	Al-Si	Decreases	-	[72]
<b>Mg</b>	Al-Mg	Independent	-	[72]

Literature investigating the effect of alloying elements on the FFC performance of AAs is sparse and often divergent. What is clear is that the composition of the AA's surface plays an important role in the FFC performance of AAs. Christopher Hahin stated that the penetration depth of filaments in Al can be as deep as 15  $\mu\text{m}$ . Therefore, FFC is a superficial phenomenon that can be controlled by surface modification [82].

### 2.3.3 Effect of Surface Treatment on improving FFC Susceptibility of AAs

Al coating is often integrated with preceding processes that promote coating adhesion and Al passivation. Several pre-treatments to inhibit FFC on AAs have been proposed, including chemical cleaning, chromating, anodizing, etc. These techniques are used individually or combined to replace or modify the natural aluminum oxide film and heighten FFC resistance. Usually, chemical cleaning is applied before other processes like chromating or anodizing. The following paragraphs briefly describe the mentioned pre-treatments, with an emphasis on anodizing.

**Chemical cleaning.** Chemical cleaning consists of exposing the bare AA to an alkaline or acid bath before applying an organic coating. The most commonly used solvents are NaOH and HNO<sub>3</sub> respectively. The effectiveness of this pre-treatment seems to depend on the AA composition. For instance, while alkaline cleaning has been observed to enhance FFC resistance on AA 7075, L. Fedrizzi observed an increase in FFC susceptibility on AA 6060 after alkaline cleaning [72], [74]. Acid cleaning, on the other hand, was found to be effective in mitigating FFC on AA6060 [83].

**Chromating.** Chromating has been identified as the most common and effective pre-treatment on organic-coated Al products. The presence of Chromium (Cr) on the Al surface, improves its FFC resistance by inducing the development of a very stable Al/Cr mixed oxide film which acts as a passivation layer and inhibits localized corrosion [17]. However, over the last decades these treatments have been restricted due to concerns over safety and environmental protection; hexavalent Cr, which is classified as a human carcinogen [84], [85], [86], is often found on chromated Al surfaces [87]. Therefore, corrosion experts are currently leading efforts to develop more health- and environment-friendly alternatives.

**Anodizing.** Anodizing is an oxidation process in which the thin Al natural oxide layer is thickened by strong anodic polarization in a suitable electrolyte. Factors such as the nature of the alloy, the electrolyte, current density, anodizing time, and voltage determine the final structure and composition of the anodic layer [88]. Anodizing is known to be an effective pre-treatment to improve metal-coating adhesion [89] and was found to drastically reduce FFC filament density and growth rate on the epoxy-coated AAs 6060, 3005 and 3103 after 2000 h of exposure to 82 % RH at 40 °C. Spoelstra observed that without anodizing FFC resistance of AA 3005 was higher

than that of AA 6060, but after the specimens were anodized, their FFC susceptibility was very similar [28]. A drastic reduction of FFC severity on organic coated AA 2024 by anodizing was also reported by Doublet [90]. The experimental and industrial procedures for anodizing can be summarized in three major stages: pre-treatment, anodizing and post-treatment.

*The pre-treatment* processes are intended to reduce surface rugosity. They consist of degreasing followed by chemical cleaning or electropolishing. Degreasing is carried out with the use of solvents like acetone and ethanol. Electropolishing is a finishing process that removes a thin layer of the Al substrate and leaves a micro-smooth and ultra-clean surface [91]. *The Anodizing process* is illustrated in **Figure 2-9** and consists of an electrochemical cell in which the AA is designated as the anode by connecting it to the positive terminal of a DC power supply. The cathode (usually platinum (Pt)) is connected to the negative terminal. Electrons are extracted from the metal at the positive terminal and directed to the cathode, which results in Al oxidation and hydrogen gas production in the anode and cathode respectively [92], [93].

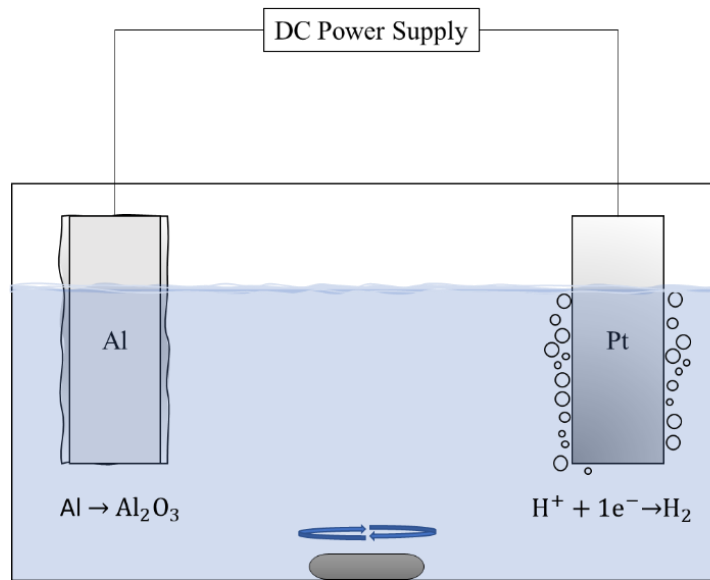


**Figure 2-9.** Schematic anodizing process of Al.

After anodizing, *post-treatment* procedures are performed to achieve the final surface properties. Anodized AAs are often sealed by immersion in boiling DI water. The oxide film  $\text{Al}_2\text{O}_3$  is converted into its hydrated form, boehmite ( $\text{AlOOH}$ ), and the swelling that results, reduces the surface porosity [94].

## 2.3.4 Filiform Corrosion Testing Methods

### 2.3.4.1 Accelerated exposure experiments

It is commonly accepted that corrosion is not an instantaneous event, it can take days or even several years to develop and spread according to the environmental conditions. Therefore, on-site testing methods are not the most convenient to evaluate the corrosion resistance of AAs. The corrosion resistance of painted metal, including FFC, is commonly evaluated using accelerated exposure tests. These techniques significantly reduce testing time and facilitate the material selection process [95], [96]. Extensive standards have been developed, from detailed testing

procedures to post-testing evaluation criteria. **Table 2-4** lists some common standards to evaluate the performance of coated metal exposed to corrosive environments.

**Table 2-4.** Common standards for coated Al corrosion testing.

<b>Standard</b>	<b>Title of the standard</b>	<b>Ref.</b>
QUALICOAT Specifications 2021	Specifications for a quality label for liquid and powder coatings on Al for architectural applications	[97]
AAMA 2603-02	Voluntary Specification, Performance Requirements and Test Procedures for Pigmented Organic Coatings on Al Extrusions and Panels	[98]
ASTM D 2803	Standard guide for testing FFC resistance of organic coatings on metal	[99]
ASTM D 1654	Standard Test Method for Evaluation of Painted or Coated Specimens Subjected to Corrosive Environments	[100]
ASTM D714	Standard Test Method for Evaluating Degree of Blistering of Paints	[101]
ASTM D2247	Standard Practice for Testing Water Resistance of Coatings in 100 % Relative Humidity	[102]
ISO 4628-2	Paints and varnishes Evaluation of degradation of coatings	[103]
ISO 9227	Corrosion tests in artificial atmospheres. Salt spray tests	[104]

In general, accelerated exposure tests involve exposing metal-coating systems to a synthetic damaging environment containing Cl<sup>-</sup> ions, high humidity, and temperatures above room temperature for several months [105]. For example, in the ISO 9227 standard, a cross-cut incision is to be made to cut the organic coating down to the metal. Then, the specimens are placed for 1000 h in an environmental chamber at 38 °C and 100 % RH using a 1 % acetic acid + 5 % Salt solution. Once the experiment is done, tape must be applied on the scribe and sharply pulled. The

degree of corrosion is determined by measuring the width of the pealed area and calculating the area fraction of surrounding blisters [104]. In ASTM D 2247 the coated samples are placed in a controlled heat-and-humidity cabinet for 1500 h at 38 °C and 100 % RH. The performance of the specimens is determined by the size and frequency of blisters on the surface [102]. The exact testing parameters are subjected to standardized or contractual specifications (between suppliers and customers). Multiple tests have shown that FFC usually occurs in environments between 35 % and 95 % RH; below 35 % RH, the humidity does not favor the formation of an undercoating electrolyte, and above 95 % RH, the form of corrosion is usually blistering rather than FFC [18], [106].

Although accelerated exposure tests are an effective approach to evaluate the performance of coated metals in extreme environments, the results can not be extrapolated to actual service conditions with accuracy [107]. The corrosion performance of different systems is assessed mainly by comparison, which allows for classification and categorization according to specific criteria, such as the number of threads (N) and length of the filaments (L) in the case of FFC testing. These parameters are calculated from qualitative results by visual examination with naked eyes or under an optical microscope (OM). These conventional methods are not only time-consuming but also restricted with a qualitative analysis of the filaments on the coated metals, providing limited information on mechanisms and kinetics. For this reason, electrochemical techniques have been established to obtain a better understanding of the FFC phenomenon and its mechanisms.

### 2.3.4.2 Electrochemical Evaluation

Overall, electrochemical methods are recognized for being effective tools to acquire essential information on corrosion mechanisms. Their attractiveness stems from the opportunity to investigate the corrosion behaviour of numerous materials directly on the solution of interest in a few hours instead of in a more aggressive environment for several months. These techniques are based on the measurement of current and/or voltage as a response to the application of an electric input on an electrochemical cell [108]. The collected data allows corrosion experts to determine critical parameters that will be later used in design decisions. For example, the open circuit potential (OCP), also known as corrosion potential ( $E_{\text{corr}}$ ) is widely used to predict galvanic coupling between different metals [109]. Nevertheless, electrochemical experiments are subjected to the correct interpretation of obtained results and must be carried out according to very strict procedures to ensure accuracy and reproducibility [110].

One of the main issues when studying Al by electrochemical techniques is the presence of the natural oxide layer; in non-passive metals, electrochemical results correspond to the characteristics of the metal surface, However, the electrochemical behaviour of passive metals, like Al, responds to a combined behaviour of the different surfaces on the alloy. According to the literature, there are three changing surfaces with varying electrochemical behaviour on AAs: anodic films, IMPs, and anodic pores [111]. The electrochemical characteristics of the anodic films on AAs are found to depend on the alloy compositions and the film's thickness (passive films between 5 and 10 nm were identified to be cathodic, while thicker films are usually inactive) [111]. **Figure 2-10** illustrates different features on the Al surface.

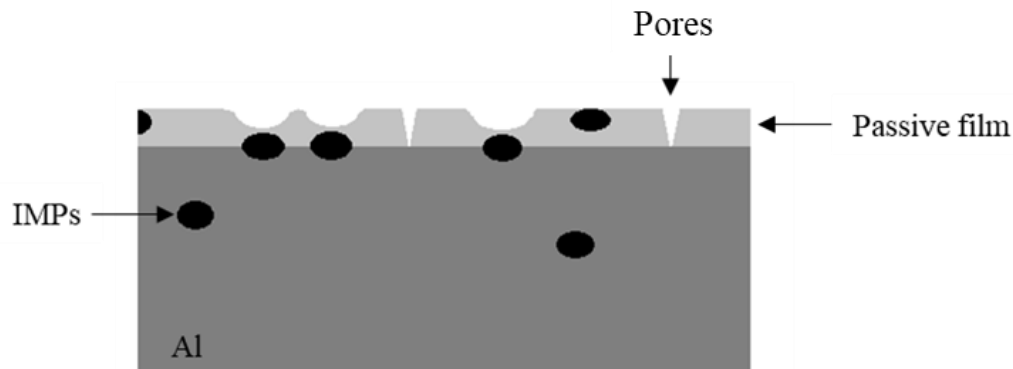


**Figure 2-10.** Schematic illustration of the AA surface with natural oxide films.

The passive nature of AAs is a challenge that has led to misinterpretation of electrochemical results. A common example is the general notion that a less negative  $E_{\text{corr}}$  indicates better corrosion resistance. While this behaviour can be observed on most common metals, AAs do not obey this trend because  $E_{\text{corr}}$  does not consider the micro-coupling occurring between the different features present on the Al surface [112]. In order to clear the controversy on the relation between the electrochemical responses and corrosion behaviour of AAs, a vast number of studies have focused on the identification and understanding of electrochemical parameters and their influence on the corrosion of AAs [113], [114]. In the last decade, considerable progress has been made in the electrochemical study of FFC on AAs [9], [30], [62], [115].

Potentiodynamic polarization (PDP) analyses are commonly conducted to predict the FFC resistance of AAs. These tests are commonly initiated by measuring the OCP, also denoted as  $E_{\text{corr}}$ , over time until a steady-state value is achieved [116]. After  $E_{\text{corr}}$  stabilization, voltage is swept at a regulated pace and  $E$  (potential) vs  $i$  (current density) curves are obtained as shown in **Figure 2-11**. For FFC investigation, PDP measurements are usually performed in an anolyte (deaerated and

acid electrolyte) and a catholyte (aerated and neutral/alkaline electrolyte) solution, simulating the under-coating conditions of FFC filaments [23], [31], [62], [117]. Each polarization curve is the sum of two curves corresponding to the anodic and cathodic electrochemical half-reactions. From these graphs, based on the mix potential theory and the conservation law, three FFC factors have been defined in literature: Resistance to FFC initiation ( $\Delta E_{PR}$ , V), the driving force for propagation ( $\Delta E_{corr}$ , V), and FFC current density ( $i_{FFC}$ , mA/cm<sup>2</sup>). These parameters will be discussed in the following paragraphs.

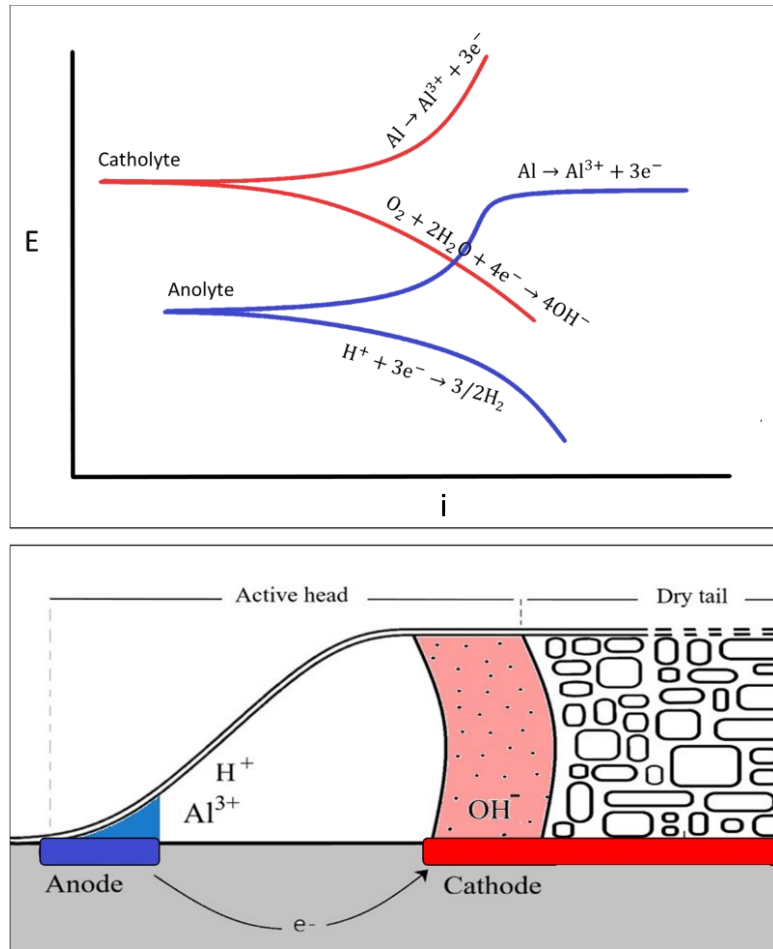


**Figure 2-11.** Schematic representation of polarization curves (semi-logarithmic) in anolyte (blue) and catholyte (red) with their respective reactions and their correspondence within an FFC filament.

### Resistance to FFC initiation ( $\Delta E_{PR}$ , V)

As mentioned earlier in this chapter, FFC initiates with the failure of the Al natural oxide layer due to a corrosive environment. Mol et al then confirmed that there was an inverse relationship between the number of FFC initiation sites and the passive range measured as the difference between the OCP and the pitting potential ( $E_{\text{pitting}}$ ) in the anolyte [31]. The passive range is the point on the PDP curve where the current suddenly increases as a result of the pitting initiation

stage, resulting in passivity collapse [118], [119], [120]. A small passive range corresponds to more rapid pitting and hence to a higher number of FFC initiations per scratch length. With regards to  $E_{\text{pitting}}$  of AAs, recent studies suggest that the sudden increase in current in the PDP curves on AAs could also be related to other forms of localized corrosion such as intergranular corrosion or the dissolution of IMPs [121]. In fact, highly heterogeneous AAs usually show two distinct inflection points corresponding to two pitting potentials that are associated with the dissolution of different active phases [122], [123]. In a word, the resistance to FFC initiation is quantitatively defined as  $\Delta E_{\text{PR}} = E_{\text{pitting}} - E_{\text{a, corr}}$  and is illustrated in **Figure 2-12**.

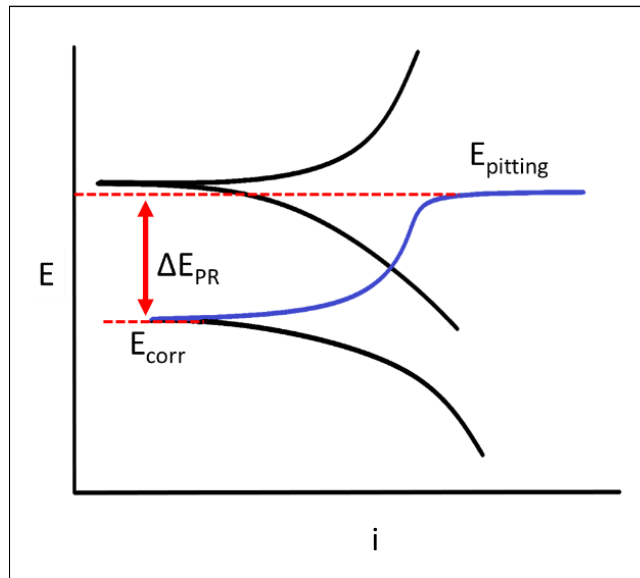


**Figure 2-12.** Schematic representation of polarization curves in anolyte and catholyte in semi-logarithmic coordinates. Graphic calculation of passive range is also shown.

**Tendency of FFC propagation:** the driving force for propagation ( $\Delta E_{\text{corr}}$ , V)

The propagation of a FFC filament from an initiation point is subjected to the presence of a more electrochemically noble site that promotes oxygen reduction when exposed to an aerated

environment [124]. The potential difference ( $\Delta E_{\text{corr}} = E_{c, \text{corr}} - E_{a, \text{corr}}$ ) between the anodic and cathodic sites in their respective electrolytes is considered to be the driving force for FFC propagation.  $\Delta E_{\text{corr}}$  has been found to be related to the number of filaments that emerged from initiation spots [62]. **Figure 2-13 (a)** presents the schematic calculation of the tendency of FFC propagation.

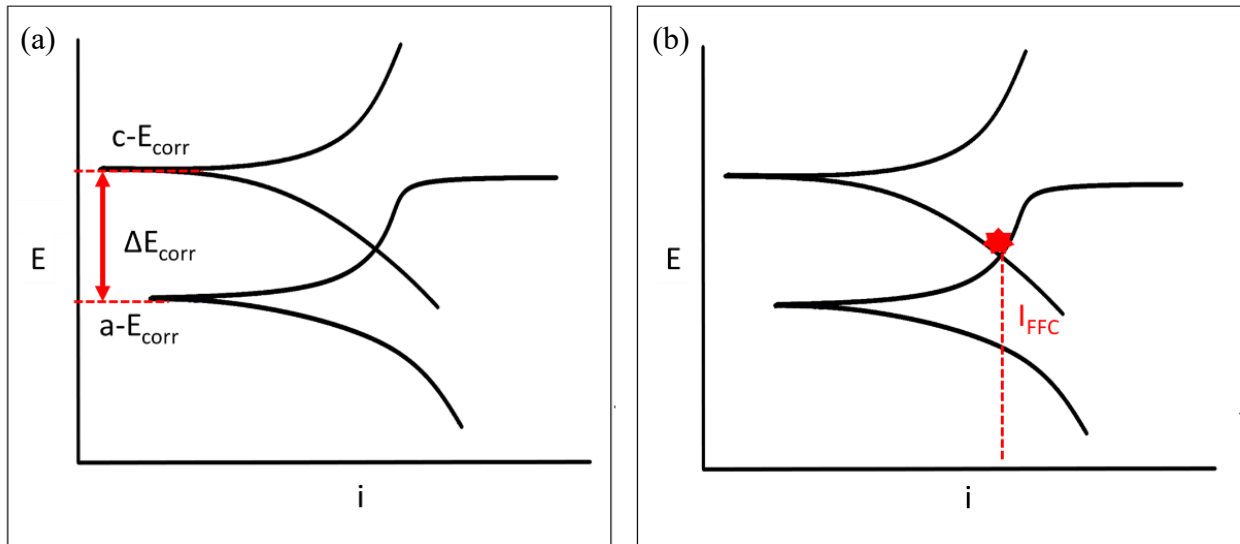


**Figure 2-13.** Schematic representation of polarization curves in the anolyte and catholyte in semi-logarithmic coordinates. Graphic calculation of (a) tendency to propagation and (b) FFC current density.

### FFC current density ( $i_{\text{FFC}}$ , mA/cm<sup>2</sup>)

Finally, based on the laws of conservation, the number of electrons produced by the anodic dissolution must be equivalent to the number of electrons consumed by the cathodic reaction. The current flows from the tip to the back of the head, as shown in **Figure 1-1**. This current is defined as the FFC current and can be calculated, according to the mixed-potential theory, as the intercept

of the anodic branch of the polarization curve in the anolyte and the cathodic branch of the polarization curve in the catholyte [9], [31], [78], as represented in **Figure 2-13 (b)**. FFC current has been proved to be proportional to the growing rate of the filaments, i.e., the kinetics of FFC [62]. In summary, resistance to FFC initiation ( $\Delta E_{PR}$ , V), the driving force for propagation ( $\Delta E_{corr}$ , V), and FFC current density ( $i_{FFC}$ , mA/cm<sup>2</sup>) together can offer better insight into the mechanisms and kinetics of FFC on AAs.

# CHAPTER 3 ELECTROCHEMICAL STUDY OF ALUMINUM FILIFORM CORROSION

The main objective of this chapter was to investigate the FFC behaviour of commercial AAs and the effects of various alloying elements on FFC by electrochemical techniques. To do so, electrochemical measurements were performed with microstructural characterization as supportive information. The present chapter is divided into 4 sections: experimental procedures, alloy characterization, discussion on the electrochemical parameters of FFC, and summary. Part of this Chapter has been published and presented as *D. Arango, J. Liu, "Electrochemical study of aluminum filiform corrosion" COM 2021: Advances in Metallurgy and Materials Engineering, Canada.*

## 3.1 EXPERIMENTAL PROCEDURES

### 3.1.1 Materials and Chemicals

A broad selection of AAs was chosen in the present research. One alloy from each series was selected according to the criteria: widely used commercial AA for outdoor applications. AA 1100 (high purity Al (99 %)) does not fulfill this condition but was selected as the "blank" comparison sample to reveal the effects of various alloying elements. AAs belonging to the 4XXX series were not covered in this study because their main application is for welding operations. **Figure 3-1** shows the selected AAs and illustrates their main alloying elements. All the specimens in this work are denoted using the commercial code followed by their main alloying element, e.g., AA1100, AA2024 (Cu), AA3003 (Mn), AA5052 (Mg), AA 6061 (Mg, Si) and AA 7075 (Zn).

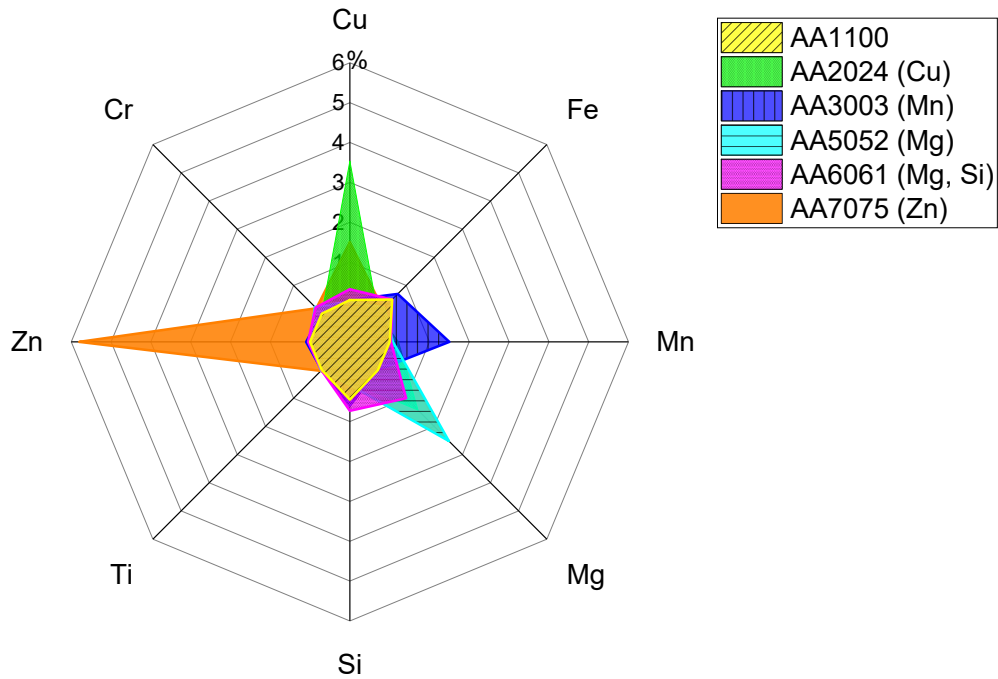


**Figure 3-1.** Radar chart of selected AAs and their main alloying elements.

The selected commercial AAs are in the common tempers in which they are employed. All samples were obtained from the same supplier, McMaster. **Table 3-1** presents the chemical compositions of the selected AAs and their corresponding heat treatment. The main alloying element is underlined. Additionally, numerous solutions were carefully prepared and used in this study. Deionized water (DI), nitric acid (HNO<sub>3</sub>), hydrochloric acid (HCl), hydrofluoric acid (HF), potassium permanganate (KMnO<sub>4</sub>) and sodium hydroxide (NaOH) were used to prepare the etchants for microstructural characterization. The etchants used are in Keller's and Weck's reagents, and their compositions are available in **Table 3-2**. DI, HCl, Aluminum chloride (AlCl<sub>3</sub>), sodium dihydrogen phosphate (NaH<sub>2</sub>PO<sub>4</sub>), and disodium hydrogen phosphate (Na<sub>2</sub>HPO<sub>4</sub>) were used to prepare the electrolytes for the electrochemical measurements.

**Table 3-1.** Chemical Composition (wt.%) of the investigated specimens.

	Cu	Fe	Mn	Mg	Si	Zn	Al	Temper
AA1100	0.05	0.5	0	0	0.45	0	99	O
AA2024 (Cu)	<u>3.53</u>	0.22	0.6	1.42	0	0	94.83	T351
AA3003 (Mn)	0.05	0.7	<u>1.5</u>	0	0.6	0.1	97.05	H14
AA5052 (Mg)	0.01	0.22	0.08	<u>2.52</u>	0.08	0.01	96.82	H32
AA6061 (Mg, Si)	0.32	0.5	0.03	<u>1</u>	<u>0.73</u>	0.05	97.14	T6511
AA7075 (Zn)	1.5	0.17	0.04	2.4	0.08	<u>5.8</u>	89.79	T651

### 3.1.2 Methods

#### 3.1.2.1 Microstructural characterization

AA samples were abraded using successive grades of SiC papers down to 1200 grit, followed by polishing with high-alumina powder till 0.5  $\mu\text{m}$ . Three techniques were used to identify the microstructure of the samples: optical microscopy (OM), scanning electron microscopy (SEM) and energy dispersive X-ray (EDS). Metallographic etching for AAs 1100, 2024, and 7075 was accomplished by using Keller's reagent, whereas AAs 3003, 5052, and 6061 were etched by using Weck's reagent. The compositions of the different reagents are listed in **Table 3-2**. Next to the metallurgical preparation of the specimens, numerous images were taken using an optical microscope (Olympus) coupled with a computerized imaging system Olympus stream software. The grain size, IMPs size and area fraction are averaged values of at least 30 measurements per image, on a total of 3 images per alloy using the software Image J 97.0.188 (Academic) from OriginLab Corporation.

**Table 3-2.** List of etchants used in the microstructure revealing.

<b>AAs</b>	<b>Etchant</b>	<b>Composition</b>
1100, 2024, 7075	Keller's reagent	190 ml DI 5 ml HNO <sub>3</sub> 3 ml HCl 2 ml HF
3003, 5052, 6061	Weck's reagent	100 ml DI 3g KMnO <sub>4</sub> 1 g NaOH

SEM images were taken using the backscattered electron signal of a Tescan scanning electron microscope. The elemental composition of the matrix and IMPs identification involved the use of an energy dispersive X-ray spectrometer supplied by Oxford Instruments INCA. The analysis was performed at an energy range between 10 kV and 15 kV. The specimens were previously mounted in conducting resin, ground, polished down to mirror finish and ultrasonically washed for 10 minutes in acetone.

### **3.1.2.2 Electrochemical measurements**

Prior to the experiment, the test specimens were abraded using successive grades of SiC papers down to 1200 grit, washed with DI water, and dried in air. As illustrated in **Figure 3-2**, the electrochemical measurements were carried out using a standard three-electrode cell with a thermostatic water jacket, a graphite rod as the counter electrode (CE), an Ag/AgCl ([KCl]=4M, 0.197 V vs. Standard Hydrogen Electrode) as a reference electrode (RE), and the AA substrate as the working electrode (WE) with a surface area of 1 cm<sup>2</sup>. The potentiostat used was a Princeton Applied Research Versastat 4 potentiostat/galvanostat.

CE	Graphite Rod
RE	Ag/AgCl ([KCl]=4M)
WE	AA
CATHOLYTE	10mM H <sub>2</sub> NaPO <sub>4</sub> 6.2mM HNa <sub>2</sub> PO <sub>4</sub> 2mM NaOH pH=7 (Aerated)
ANOLYTE	5% NaCl 0.1 M AlCl <sub>3</sub> 1mM HCl pH=2 (Deaerated with N <sub>2</sub> )

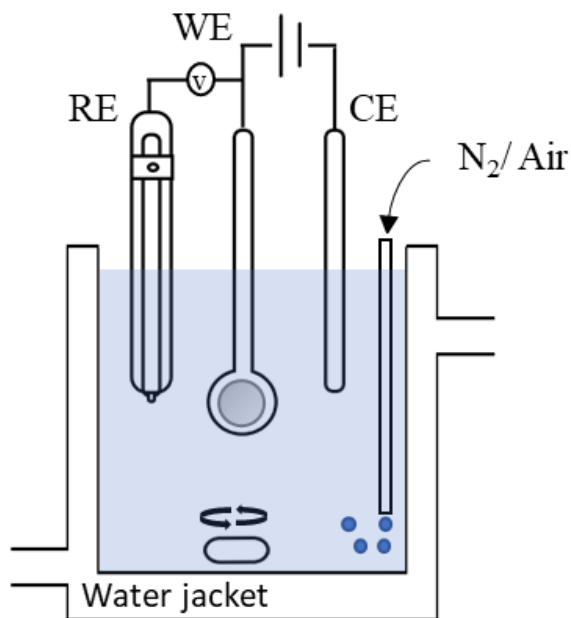


**Figure 3-2.** Conventional three-electrode cell used for electrochemical measurements. The experimental parameters are also listed.

Each sample was immersed in the anolyte and catholyte for 5 and 3.8 h respectively before starting the polarization measurements to stabilize the OCP. PDP measurements were performed from  $-400$  mV up to  $+400$  mV vs. OCP at a scan rate of  $0.2$  mV/sec in solutions at  $25$  °C. The anolyte consisted of a solution of  $5\%$  NaCl +  $0.1$ M AlCl<sub>3</sub> acidified to pH =2 with concentrated HCl and actively deaerated with nitrogen (N<sub>2</sub>) gas. The catholyte used was an aerated phosphate buffer solution  $10$ mM NaH<sub>2</sub>PO<sub>4</sub> and Na<sub>2</sub>HPO<sub>4</sub> (pH = 7). Both electrolytes were stirred at  $600$  rpm during the experiment. **Table 3-3** lists the characterization techniques employed along with the experimental objectives.

**Table 3-3.** Summary characterization and testing methods used.

	<b>Technique</b>	<b>Objective</b>	<b>Equipment Info</b>
<b>Microstructural Characterization</b>	OM	Microstructure revealing	Olympus
	SEM	Phases identification	Tescan scanning electron microscope
	EDS	Elemental composition of Al-matrix and IMPs	Oxford Instruments
<b>FFC Electrochemical parameters</b>	OCP	Evolution of corrosion potential	
	PDP	<ul style="list-style-type: none"><li>• The electrochemical response of the specimens</li><li>• FFC electrochemical parameters calculation</li></ul>	Princeton Applied Research

### **3.2 CHARACTERIZATION OF ALLOYS**

Mechanical properties and corrosion resistance of AAs are strongly related to their microstructure [125]. Multiple studies have identified that the microstructure of a metal strongly depends on the alloying elements, mechanical processing, and heat treatments [126], [127] [128]. These three factors lead to the formation of distinct phases with different sizes, shapes, and distribution as a consequence of equilibrium reactions and alloying elements solubility [129]. In the present segment, some general microstructural features of the selected AAs were identified using OM, SEM, and EDS in order to gather the information that will help to explain the FFC susceptibility of various AAs.

### 3.2.1 AA1100

AA1100 belongs to the 1XXX series that include all grades of commercially pure unalloyed Al. This alloy contains small amounts of Fe and Si as a consequence of the smelting process of alumina [130]. **Figure 3-3** shows the OM images of the AA1100 sample a) before and b) after etching. The images revealed an average grain size of  $35.37 \pm 8.5 \mu\text{m}$  and elongated IMPs mostly distributed near the grain boundaries. The IMPs exhibited a length of  $3.64 \pm 1.27 \mu\text{m}$  with an aspect ratio of about 5 : 1. Also a area fraction of 3.96 %. The low solubility of Fe on Al has been well-documented [131]. Therefore, Fe was expected to be the main constituent of the IMPs observed.

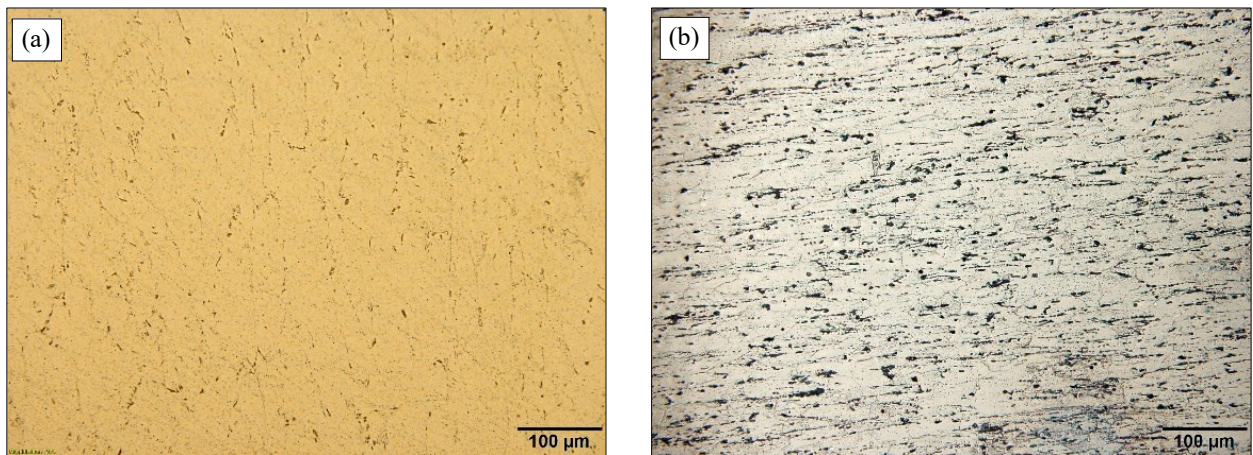


**Figure 3-3.** OM Images of AA1100 (a) as polished and (b) after etching using Keller's reagent for 15s.

A BSE SEM image of sample AA1100 is shown in **Figure 3-4** (a). Results from mapping-based EDS analysis on the selected area are also displayed in **Figure 3-4** (b). In agreement with the literature, Fe-rich IMPs were observed. Further point-based EDS tests were carried out and the presence of  $\text{Al}_{12}\text{Fe}_3\text{Si}_2$ ,  $\text{Al}_6\text{Fe}$ , and  $\text{Al}_3\text{Fe}$  was established. Such IMPs have been also reported in

the literature [132], [133]. The matrix exhibited a composition of 100 % Al. Even though there was trace Cu in the alloy, it was not possible to identify its distribution on the sample surface due to the detection limits of the applied technique. In addition, several studies on AA1100 agree that small additions of Cu (in this case 0.05 %, see table 3-1) are found to be in solid solution [134].

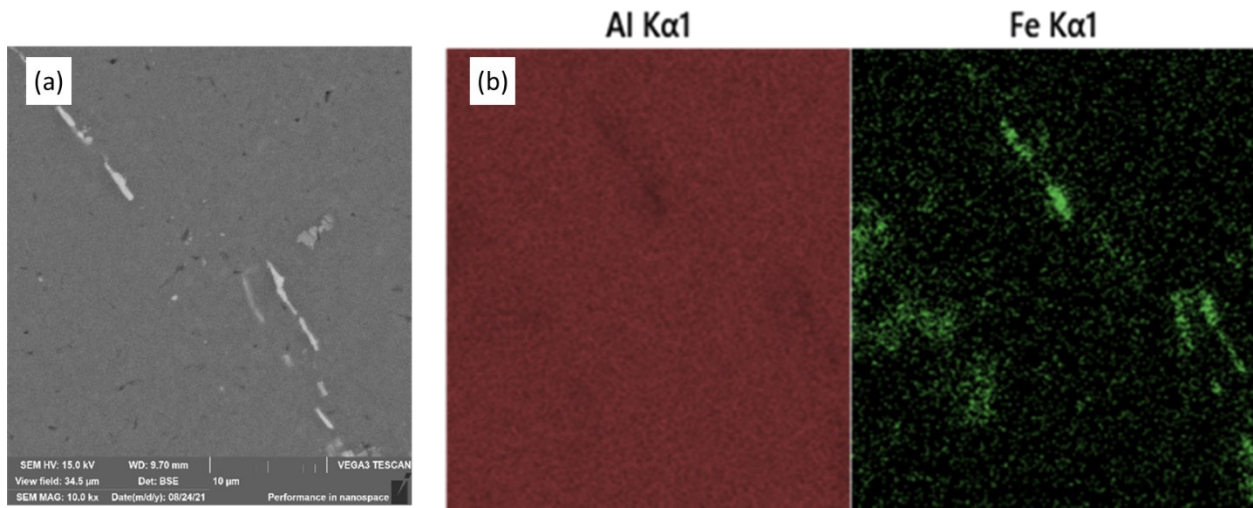


**Figure 3-4.** (a) BSE-SEM imaging for as polished AA1100 and (b) EDS maps of Al (red) and Fe (green) distribution on the framed area.

### 3.2.2 AA2024 (Cu)

Al-Cu alloys are a very important family of alloys with great mechanical properties as Cu is known to provide a significant strengthening effect [135]. The OM images for the AA2024 (Cu) sample as polished and after etched are shown in **Figure 3-5** (a) and (b) respectively. From both images, it is possible to identify a multi-phase microstructure consisting of an Al-matrix with IMPs uniformly distributed on the alloy surface with a area fraction of 4.26 %. The average grain size was found to be  $81.98 \pm 14.9 \mu\text{m}$

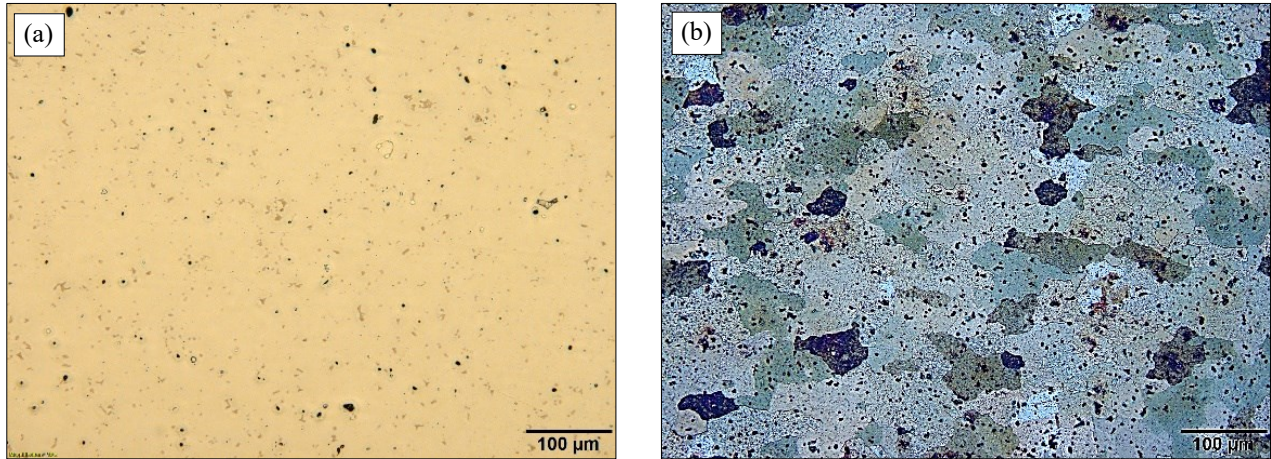


**Figure 3-5.** OM Images of AA2024 (Cu) (a) as polished and (b) after etching using Keller's reagent for 10s.

The BSE - SEM micrograph observed in **Figure 3-6** (a) clearly shows two kinds of IMPs. One of them is visually much darker with a nearly circular shape. The second is brighter with an irregular shape. The EDS-mapping results for these two specific particles framed in the SEM image are shown in **Figure 3-6** (b). While the darker IMPs consist of Al, Cu, and Mg, the presence of Al, Cu, Mn, Fe, and Si was identified in the bright irregular IMPs. Most of the particles are 'duplex', containing both IMPs. Such IMPs have also been observed by other authors [136]. The average sizes for the IMPs Al-Cu-Mg and Al-Cu-Mn-Fe-Si are  $3.49 \pm 1 \mu\text{m}$  and  $4.31 \pm 1.5 \mu\text{m}$  respectively.

The point-based EDS analyses on multiple areas of the sample revealed that the matrix was composed of about 96.3 % Al, 2 % Cu, and 1.7 % Mg. In addition, EDS analysis results in combination with the available literature for AA2024-T361 allowed us to assign the dark IMPs as the hardening phase  $\text{Al}_2\text{CuMg}$ , known as the S-phase. The second type was assigned as  $\text{Al}_6\text{CuFe}(\text{Mn})$ . These results agreed with the previous studies [137], [138], [139].

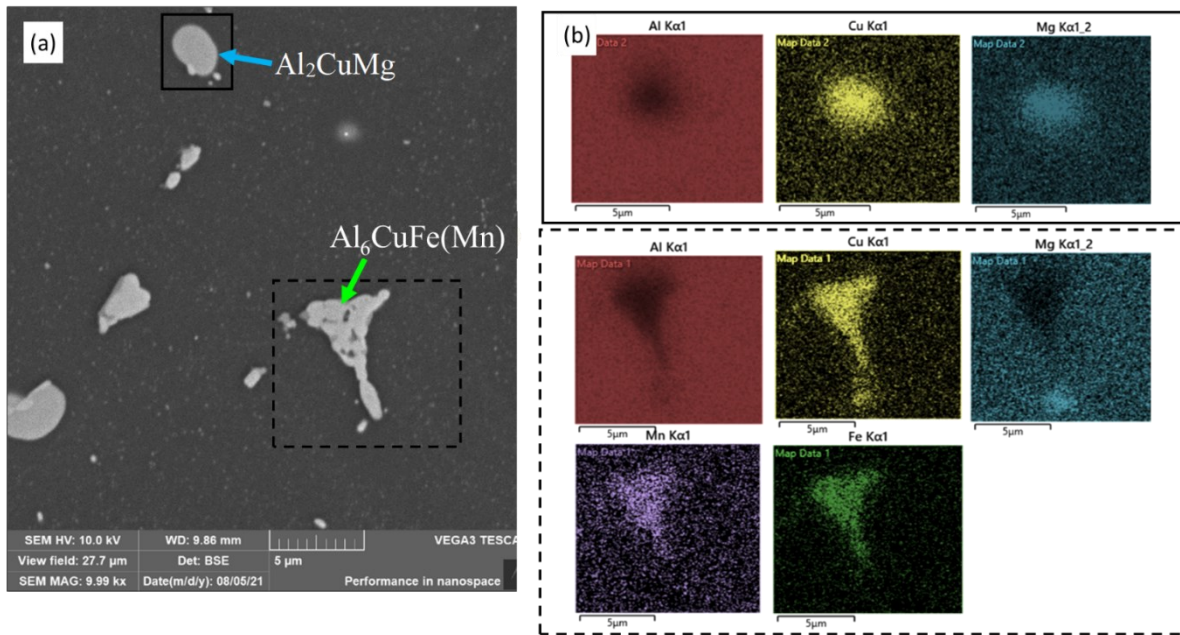


**Figure 3-6.** (a) BSE-SEM imaging for as polished AA2024 (Cu) and (b)EDS maps of chemical elements distribution on the framed areas showing Al-Cu-Mg as rounded dark IMPs and Al-Cu-Fe-Mn as irregularly shaped bright IMPs.

### 3.2.3 AA 3003 (Mn)

The 3XXX series are medium strength AAs alloyed mainly with Mn. AA3003 is the most representative alloy of this family and consists of the addition of Mn to AA1100. Mn significantly increases the mechanical properties of AAs while maintaining good formability [140]. Existing literature examining Al-Mn alloys reported that adding Mn would initially supersaturate the solid solution and subsequently precipitate as IMP constituents during heat treatment [141]. The OM images for the AA3003(Mn) sample as polished and after etched are shown in **Figure 3-7** (a) and (b) respectively. **Figure 3-7** (a) shows large IMPs corresponding to a area fraction of around 5.18 % of the total surface area were also observed uniformly distributed in the matrix.

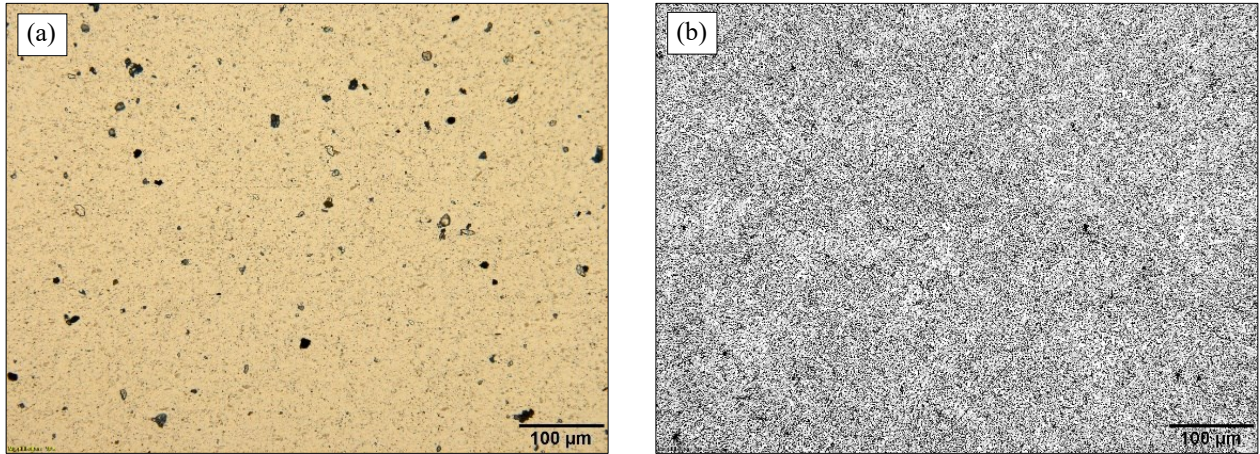


**Figure 3-7.** OM Images of AA3003 (Mn) (a) as polished and (b) after etching using Weck's reagent for 15s.

**Figure 3-8** (a) shows BSE SEM micrograph for AA3003(Mn). In accordance with the literature, two different types of IMPs are identified and well distinguished by their shape. One type has a stretched ellipse form and the second one is characterized by its irregular shape. Mapping-EDS (**Figure 3-8** (b)) and point-based analysis showed that the elongated IMPs corresponds to the phase  $\text{Al}_6(\text{Mn}, \text{Fe})$ , and the irregular IMPs can be assigned to the phase  $\alpha\text{-Al Fe}(\text{Mn}) \text{Si}$  [142], [143], [144]. The matrix composition was identified as 99.3 % Al and 0.7 % Mn. In addition, the black areas observed in **Figure 3-8** (a) were identified as defects that appear as hollows on the micrograph, probably produced by the polishing process.  $\text{Al}_6(\text{Mn}, \text{Fe})$  IMPs were observed to have a length of  $4.38 \pm 1.6 \mu\text{m}$  and aspect ratio of about 8:1, while  $\alpha\text{-Al Fe}(\text{Mn}) \text{Si}$  IMPs average size was  $2.78 \pm 1 \mu\text{m}$ . Furthermore,  $\text{Al}_6(\text{Mn}, \text{Fe})$  IMPs only represented 0.9 % of the total AA surface area.

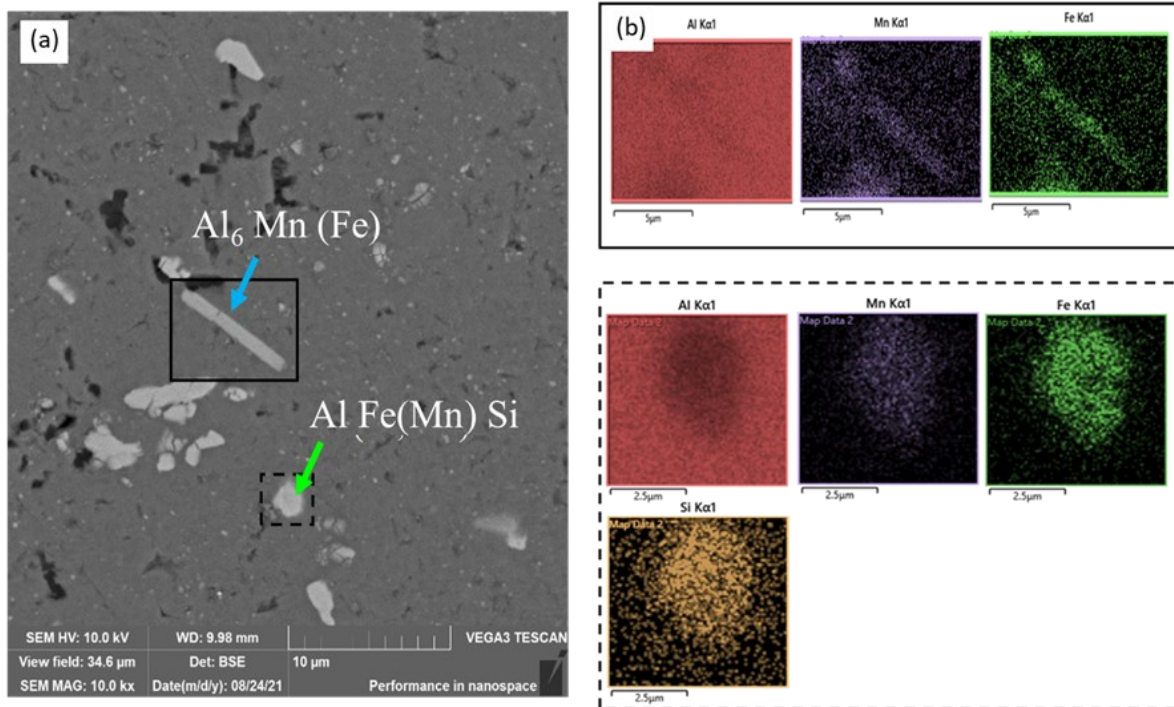


**Figure 3-8.** (a) BSE-SEM imaging for as polished AA3003 (Mn) and (b) EDS maps of chemical elements distribution on the framed areas showing Al-Fe-Mn as the elongated IMPs and Al-Fe-Mn-Si as the irregular shaped IMPs.

### 3.2.4 AA 5052 (Mg)

AA 5052 belongs to the 5XXX series. The addition of Mg provides the alloy with a medium to high strength as well as very good weldability and cold formability [145]. Mg possesses high solubility on Al, so it is largely present in solid solution. However, in presence of Si, it tends to precipitate as  $Mg_2Si$  [146]. **Figure 3-9** presents the OM images of the AA5052(Mg) sample after polishing (a) and after etching (b). The OM images reveal a refined grain structure with a uniform distribution of IMPs that correspond to 1 % of the total surface. The average grain size was 3.6  $\mu m$

with a standard deviation of  $\pm 0.8 \mu\text{m}$ . A large number of small dispersoids are also seen on the surface and attributed by several authors to  $\text{MnAl}_6$  [147].

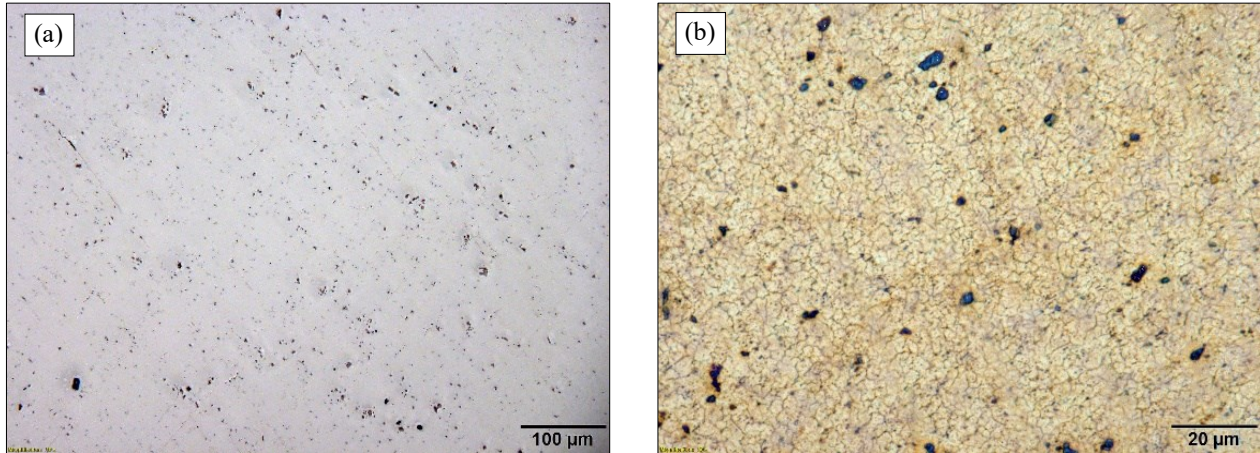


**Figure 3-9.** OM Images of AA5052 (Mg) (a) as polished and (b) after etching using Weck's reagent for 20 s.

**Figure 3-10** (a) shows a BSE SEM micrograph for AA5052 (Mg) and (b) the corresponding EDS mapping images for the selected regions. Region 1 (framed in solid line) shows Al, Fe containing IMPs, and region 2 (framed in dashed line) reveals two types of IMPs that can be distinguished by their contrast in the BSE image. The gray particles in region 2 were found to contain Al, Fe, Mn, Cr, and Si and the smaller black particles exhibited the presence of Mg and Si. The compositions of the IMPs and the matrix were detected by point-based EDS analysis. Three types of IMPs were identified:  $\text{Al}_3\text{Fe}$ ,  $\text{Al Fe}(\text{Mn, Cr}) \text{Si}$  and  $\text{Mg}_2\text{Si}$  with average sizes of  $1.53 \pm 0.5 \mu\text{m}$ ,  $2.56 \pm 0.6 \mu\text{m}$  and  $0.68 \pm 0.3 \mu\text{m}$  respectively. These findings agree with previous studies that have identified both,  $\alpha\text{-Al}_8\text{Fe}_2\text{Si}$  and  $\beta\text{-Al}_5\text{FeSi}$  with Mn and Cr replacing some of Fe atoms [148]. The Al-rich matrix is composed of 97.1 % Al and 2.9 % Mg.

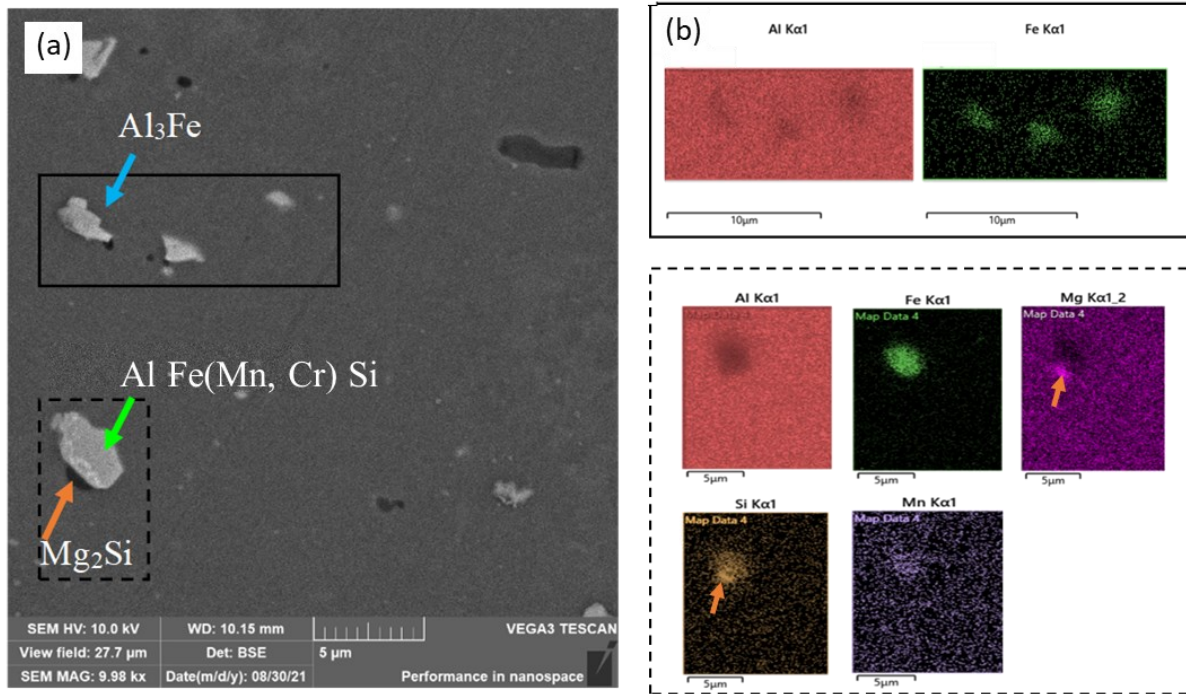


**Figure 3-10.** (a) BSE-SEM images of as polished AA5052 (Mg) and (b) EDS maps of chemical elements distribution on the framed areas showing gray Fe-containing IMPs and black  $Mg_2Si$  IMPs.

### 3.2.5 AA 6061 (Mg, Si)

AA6061 is an Al-Mg-Si alloy with good plasticity, low density, high strength, and great formability [149]. The OM micrographs before (a) and after (b) the etching process are presented in **Figure 3-11**. The images clearly show IMPs covering around 2.63 % of the total surface and mainly populated at the vicinity of the grain boundaries. The average grain size was found to be 18.32  $\mu m$  with a standard deviation of  $\pm 3.5 \mu m$ . The elongation of the grains is evident, and the area ratio measured was 1 : 2.

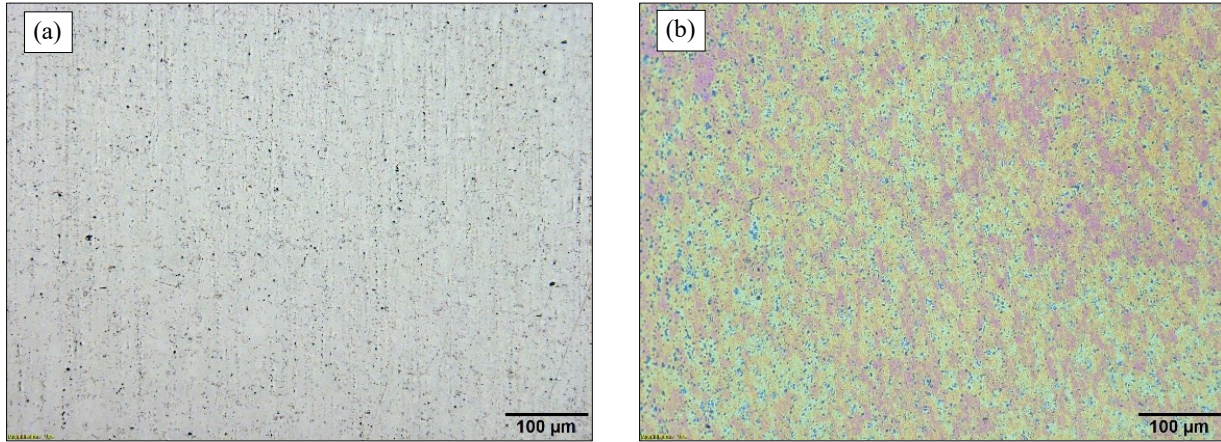


**Figure 3-11.** OM Images of 6061 (Mg) (a) as polished and (b) after etching using Weck's reagent for 15s.

**Figure 3-12** (a) presents a BSE SEM micrograph for the AA 6061(Mg, Si) sample after polishing. The evident contrast between the IMPs observed reveals an important variation in their composition. The EDS analysis shown in **Figure 3-12** (b) revealed that the bright IMPs are mainly composed of Al, Fe, and Si, whereas the dark IMPs contain Mg and Si. These results are consistent with the literature as the presence of  $Mg_2Si$  is a well-recognized strengthening phase on AA 6061. In addition, IMPs such  $\alpha$ -AlFeSi,  $\beta$ -AlFeSi have been previously observed and categorized as Al-Fe-Si phases. Al-Fe-Si IMPs are known to improve the ductility of AAs [150], [151], [152]. The size of the IMPs was found to be  $3.85 \pm 1.2$  for Al-Fe-Si and  $1.49 \pm 0.3$  for  $Mg_2Si$  with a area fraction of 1.5 and 1.13% respectively. The composition of the matrix is around 98.7 % Al, 0.8 % Mg, and 0.5 % Si.

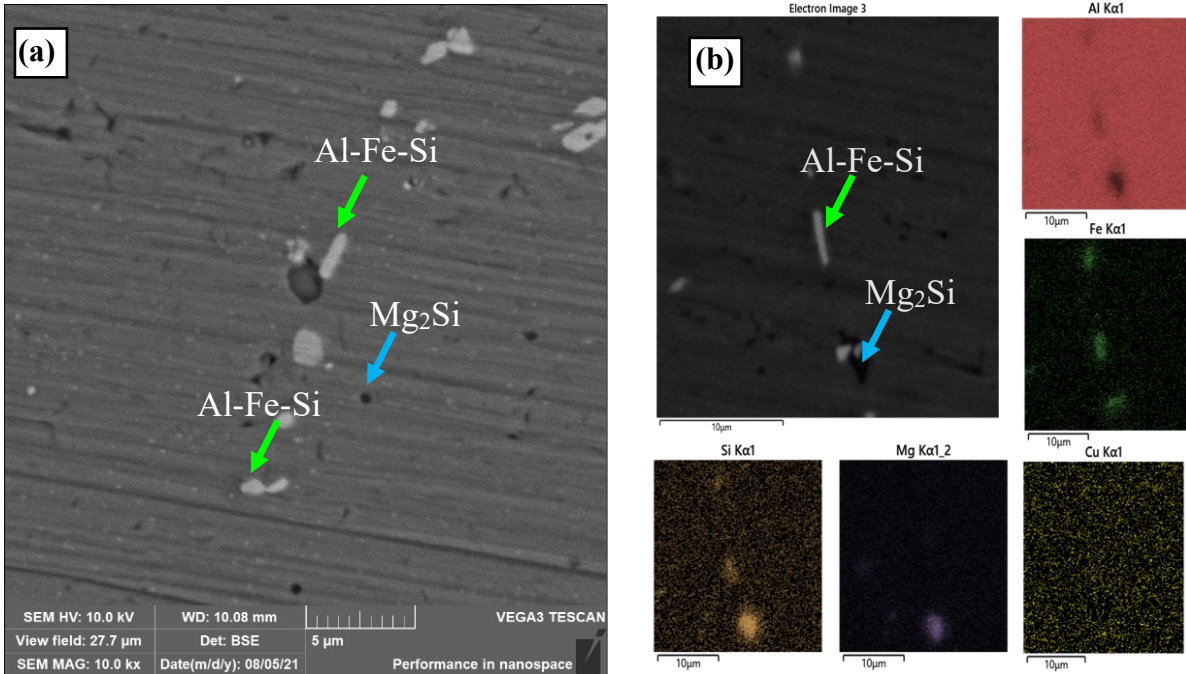


**Figure 3-12.** (a) BSE-SEM image of as polished AA6061 (Mg, Si) and (b) BSE micrograph EDS maps of chemical elements distribution showing bright Fe-containing IMPs and dark Mg<sub>2</sub>Si.

### 3.2.6 Alloy 7075 (Zn)

AAs alloys belonging to the 7XXX series are widely used in the aircraft and automobile industry due to their exceptionally high strength, fracture toughness, and stress corrosion cracking properties [153]. Zn, by itself, is highly soluble in Al and usually found in solid solution [154]. The OM images for the AA7075 (Zn) sample are shown in **Figure 3-13**. The overall microstructure reveals IMPs primarily distributed near the grain boundaries. The average grain size is 54.7 μm with a standard deviation of ±11 μm.

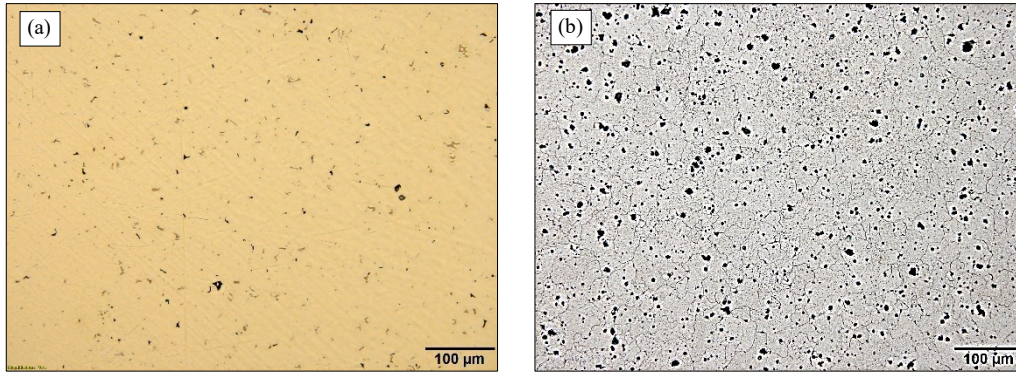


**Figure 3-13.** OM Images of AA7075 (Zn) (a) as polished and (b) after etching using Keller's reagent for 10s.

A BSE SEM image of the sample is shown in **Figure 3-14** (a). The contrast between the two types of IMPs can be seen in the BSE image. One of them, brighter than the matrix with an average size of  $3.47 \pm 1.1 \mu\text{m}$  and a area fraction of 1 %, and the other one darker than the matrix with an average size of  $2.57 \pm 0.9 \mu\text{m}$  and a area fraction of 0.25 %. EDS mapping analysis was conducted on the entire area of the micrograph, the results are shown in **Figure 3-14** (b). The darker IMPs are rich in Mg and Si. Point-based EDS calculations suggest an approximate atomic ratio of 2:1. Thus, the darker IMPs can be assigned to the phase  $\text{Mg}_2\text{Si}$ ; these IMPs were also previously observed in AA5052 (Mg) and AA6061 (Mg, Si). The brighter IMPs are rich in Cu and Fe and can be identified as  $\text{Al}_7\text{Cu}_2\text{Fe}$ , in some cases additives elements such as Cr or Mn can substitute some Fe atoms [155], [156], [157]. EDS results also revealed the chemical composition of the matrix correspond to 93.6 % Al, 0.5 % Cu, 3 % Mg, and 2.6 % Zn.

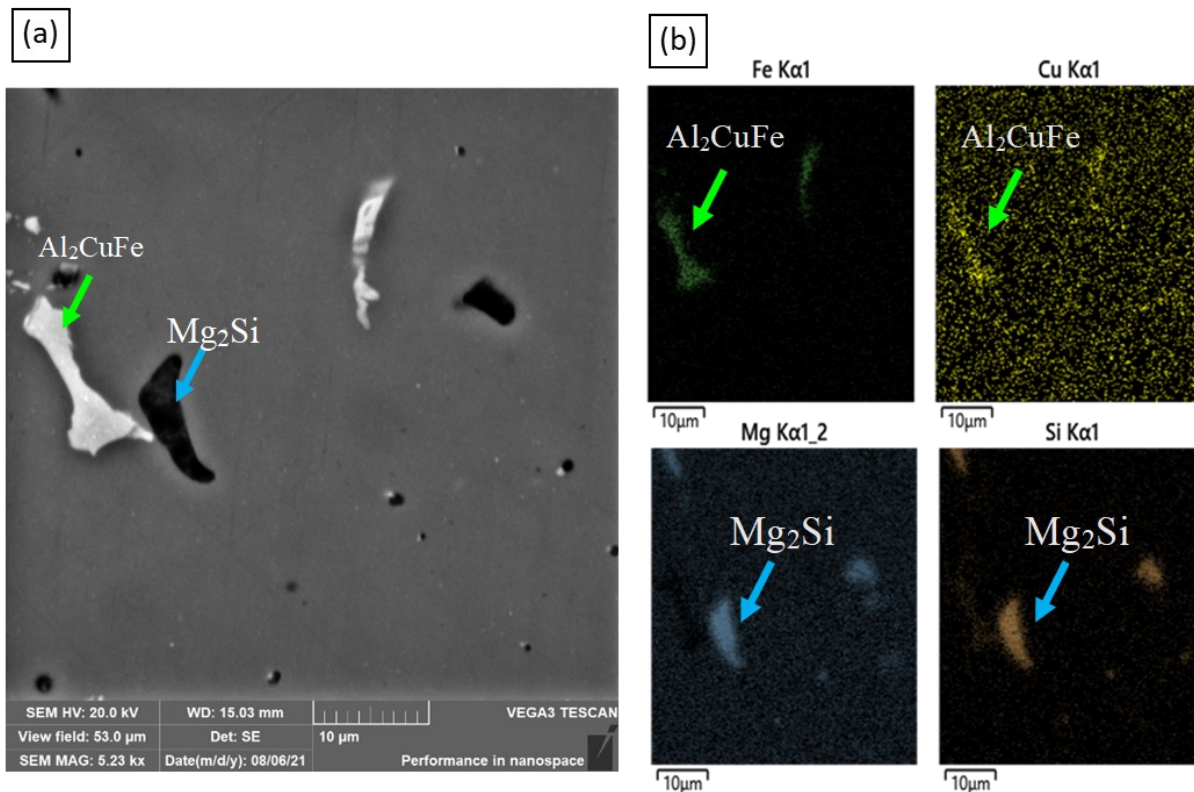


**Figure 3-14.** (a) BSE-SEM image of as polished AA7075 (Zn) and (b) EDS maps of chemical elements distribution showing bright Al-Cu-Fe containing IMPs and dark  $\text{Mg}_2\text{Si}$ .

As confirmed in the microstructural characterization, AAs consist of a matrix rich in alloying elements and IMPs mainly distributed in the matrix and at the grain boundaries. In summary, the matrix composition and IMPs obtained by SEM and EDS analysis for each alloy are listed in **Table 3-4**. These particles have different physical and electrochemical properties from those of the matrix and may constitute cathodic or anodic sites [158].

In order to support and explain the electrochemical behaviour of these AAs and adequately correlate it with their FFC performance, it is important to identify the role of the IMPs on the electrochemical response of each specimen. It has been reported that large IMPs particles (1 to 10

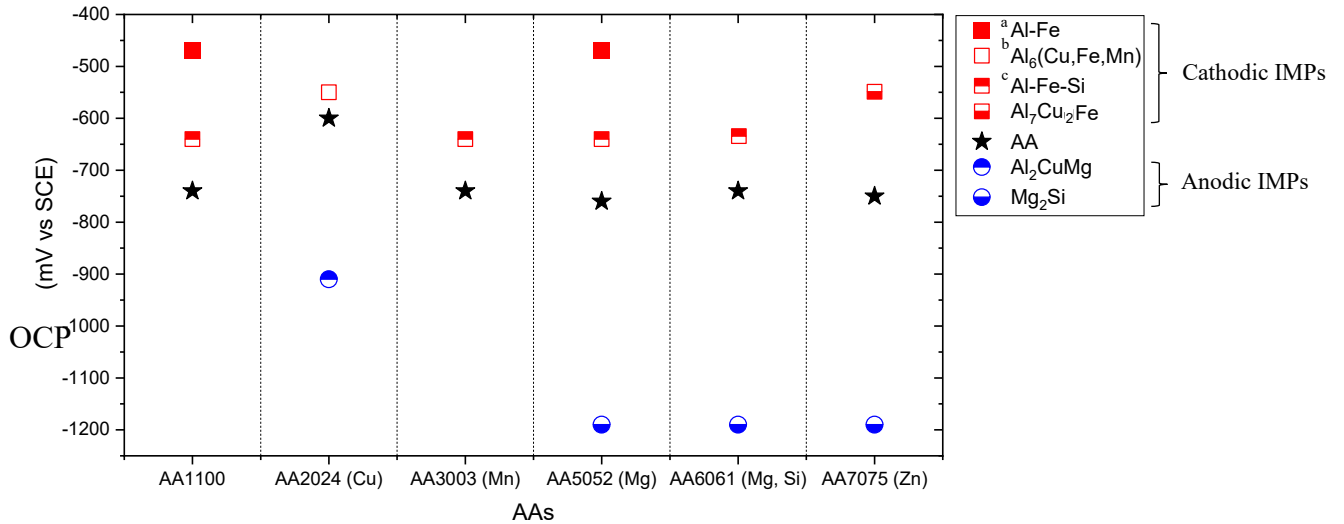
$\mu\text{m}$ ) are more common and have a major impact on corrosion resistance than dispersoids [159]. Therefore, considering their high volume-fraction and influence on corrosion, large particles will be given first attention in this study.

**Table 3-4.** Summary of the matrix composition and IMPs obtained by EDS point base analysis at different locations for each alloy.

Al Alloy	Matrix Composition (Atomic %)						IMPs	Average Size (Diameter) ( $\mu\text{m}$ )
	Al	Cu	Mn	Mg	Si	Zn		
AA1100	100	-	-	-	-	-	Al <sub>6</sub> Fe, Al <sub>3</sub> Fe	3.64 ± 1.3
							Al- Fe- Si	
AA2024 (Cu)	96.3	2	-	1.7	-	-	Al <sub>2</sub> CuMg	3.49 ± 1
							Al <sub>6</sub> CuFe(Mn)	4.31 ± 1.5
AA3003 (Mn)	99.7	-	0.3	-	-	-	Al Fe(Mn) Si	4.38 ± 1.6
							Al <sub>6</sub> (Fe, Mn)	2.78 ± 1
AA5052 (Mg)	97.1	-	-	2.9	-	-	Al <sub>3</sub> Fe	1.53 ± 0.5
							Al Fe(Mn, Cr) Si	2.56 ± 0.6
							Mg <sub>2</sub> Si	0.68 ± 0.3
AA6061 (Mg, Si)	98.7	-	-	0.8	0.5	-	Al- Fe- Si	3.85 ± 1.2
							Mg <sub>2</sub> Si	1.49 ± 0.3
AA7075 (Zn)	93.9	0.5	-	3	-	2.6	Al <sub>7</sub> Cu <sub>2</sub> Fe	3.47 ± 1.1
							Mg <sub>2</sub> Si	2.57 ± 0.9

**Figure 3-15** presents the  $E_{\text{corr}}$  values found in the literature for various alloys and their respective IMPs. Despite the variation between one paper to another in the reported  $E_{\text{corr}}$  values for IMPs, their cathodic or anodic behaviour is consistent. Even though the  $E_{\text{corr}}$  values of the alloys are mainly attributed to the matrix solid solution and the natural oxide layer [112], localized corrosion highly depends on the anodic or cathodic nature of IMPs with respect to the matrix, which is critical for the FFC behaviour presented in the next section. Generally speaking, IMPs containing Mg tend to be anodic relative to the matrix, whereas those containing Fe tend to be more cathodic [159].

When cathodic IMPs are present on an exposed surface, galvanic cells are created between these particles and the matrix, promoting the Al matrix dissolution. In contrast, anodic IMPs will dissolve preferentially [160].



- The Al-Fe IMPs include particles in which Fe atoms are replaced by Mn: Al<sub>6</sub>Fe, Al<sub>3</sub>Fe and Al<sub>6</sub>(Fe, Mn).
- The OCP Measurement was reported in aerated 0.1 M NaCl, the addition of H<sub>2</sub>O<sub>2</sub> was not stated.
- The Al-Fe-Si IMPs include particles in which Fe atoms are replaced by Mn and Cr: α-AlFeSi, β-AlFeSi, Al Fe(Mn, Cr) Si. The OCP measurement was reported in aerated 0.01 M NaCl.

**Figure 3-15.** Summary of  $E_{\text{corr}}$  distribution of IMPs in a standard 0.1M NaCl, H<sub>2</sub>O<sub>2</sub> solution [161], [112], [162].

### 3.3 ELECTROCHEMICAL PARAMETERS OF FFC

As reported earlier in Chapter 1, FFC on AAs proceeds with an anodic reaction in the head of the filament, where the electrolyte is characterized by a low pH, low O<sub>2</sub> concentration, and high Cl<sup>-</sup> concentration. The cathodic reaction takes place in the back of the head, where the electrolyte is characterized with a high pH, high O<sub>2</sub> concentration, and low Cl<sup>-</sup> concentration [163], [18]In the

present section, the electrochemical response of the selected AAs will be evaluated in these two described simulated environments, i.e., anolyte and catholyte. The objective here is to characterize the FFC susceptibility of AAs 1100, 2024 (Cu), 3003 (Mn), 5052 (Mg), 6061 (Mg, Si), and 7075 (Zn) using an electrochemical approach. Three FFC electrochemical parameters will be adopted and calculated according to the literature and the different stages (i.e., initiation, propagation, and growth) of FFC on coated AAs [31] [62]. **Table 3-5** provides a brief description of these three parameters.

**Table 3-5.** Electrochemical parameters of FFC.

<b>FFC</b>		
<b>Parameter</b>		
Resistance to FFC initiation	$(\Delta E_{PR}, V)$	$\Delta E_{PR} (= E_{pitting} - E_{a, corr})$
Tendency to FFC propagation	$(\Delta E_{corr}, V)$	$\Delta E_{corr} (= E_{c, corr} - E_{a, corr})$
Propagation kinetic	$(i_{FFC}, A/cm^2)$	Intercept point between the anodic curve in the anolyte and cathodic curve in the catholyte.

### 3.3.1 Resistance to FFC initiation

FFC initiation of AAs has been strongly linked to the corrosion resistance of the Al passive film. In a previous study, Spoelstra found that there were many initiation points of FFC on anodized AAs [64]. Mol et al then confirmed that there was an inverse relationship between the number of FFC initiation sites and the passive range measured as the difference between the OCP and the pitting potential ( $E_{pitting}$ ) in the anolyte for Cu and Zn binary alloys [31]. Therefore,  $E_{pitting}$  (which corresponds to the rupture of the passive film) is a useful parameter to predict the FFC initiation

of AAs.  $E_{\text{pitting}}$  is usually determined from a typical polarisation curve as the point where the current suddenly increases as a result of the pitting initiation stage, resulting in passivity collapse. [164] In this study, as mentioned in Section 2.3.4.2, the passive range is defined as  $\Delta E_{\text{PR}} (= E_{\text{pitting}} - E_{\text{a, corr}})$ ,  $E_{\text{a, corr}}$  is the OCP value measured in the  $\text{N}_2$ -deaerated anolyte.

The PDP curves of AAs after 5h of OCP stabilization in  $\text{N}_2$ -deaerated anolyte are presented in **Figure 3-16**. The results clearly show a passive range in all samples, except for AA1100 which presents an active polarization behaviour with a high current increasing rate with increasing potential. To compare the  $E_{\text{pitting}}$  in a more consistent way,  $E_{\text{pitting}}$  is defined here as the potential where the current continuously exceeds  $1 \text{ mA/cm}^2$  [165]. The values of  $E_{\text{pitting}}$ ,  $E_{\text{a, corr}}$  and  $\Delta E_{\text{PR}}$  for all six samples are shown in **Table 3-6**. With an initial approach,  $\Delta E_{\text{PR}}$  results suggest that the resistance to FFC initiation follows a tendency of AA 2024 (Cu) > 5052 (Mg) > AA7075 (Zn) > 3003 (Mn) > AA6061 (Mg, Si) > AA1100, and adding alloying elements reduces the propensity for FFC initiation.

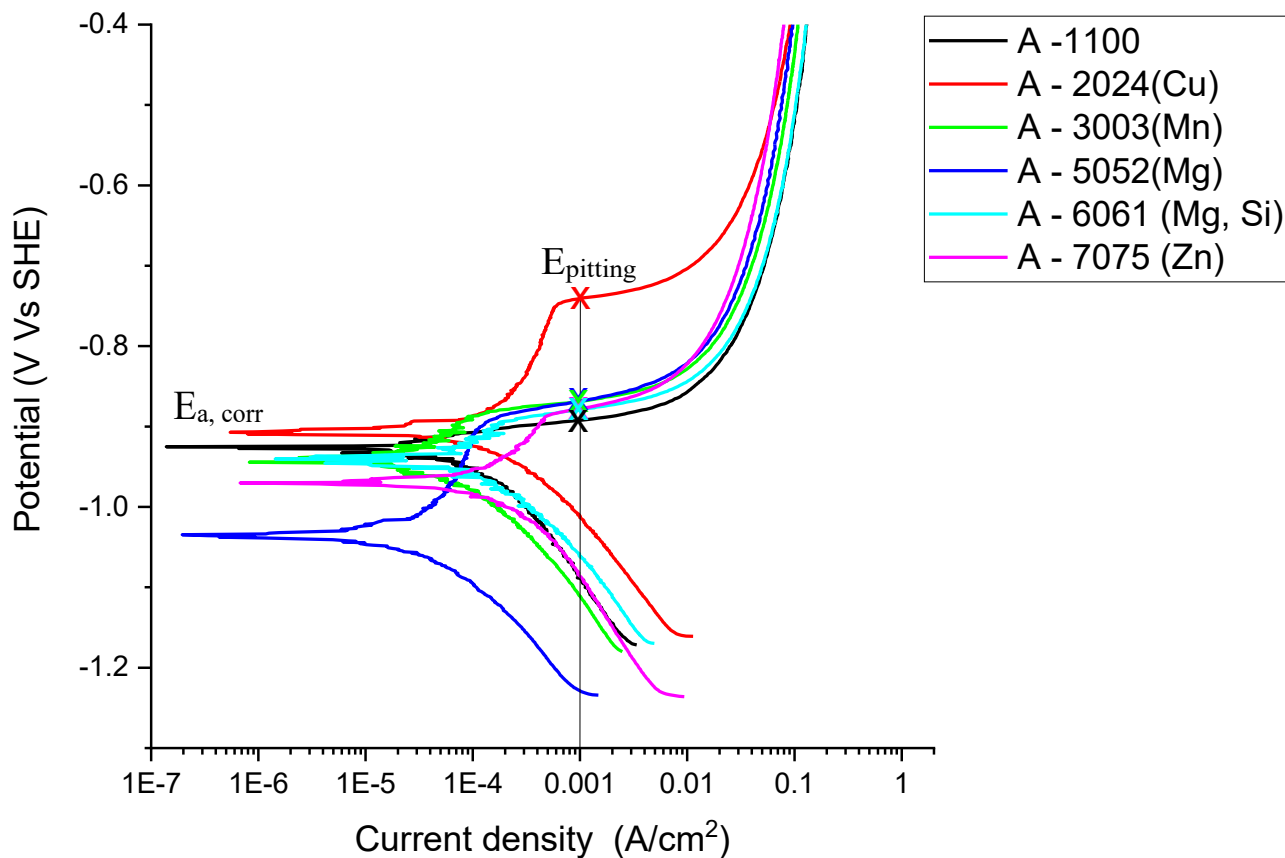


**Figure 3-16.** PDP curves of AAs in the N<sub>2</sub>-deaerated anolyte.

**Table 3-6.** E<sub>pitting</sub>, E<sub>a, corr</sub> and ΔE<sub>PR</sub> of AAs from PDP curves in N<sub>2</sub>-deaerated anolyte.

AAs	E <sub>a, corr</sub> (V vs. SHE)	E <sub>pitting</sub> (V vs. SHE)	ΔE <sub>PR</sub> (V vs. SHE)
AA1100	-0.922	-0.882	-0.045
AA2024 (Cu)	-0.897	-0.736	-0.170
AA3003 (Mn)	-0.944	-0.864	-0.079
AA5052 (Mg)	-1.035	-0.867	-0.168
AA6061 (Mg, Si)	-0.938	-0.879	-0.059
AA7075 (Zn)	-0.971	-0.881	-0.089

Compared with **Table 3-6**, different information has been reported before [133], [166]. For example, the worst resistance to pitting corrosion is usually ascribed to Cu containing AAs. AAs belonging to the 2XXX series are known for being the most susceptible to pitting, followed by the 7XXX, 6XXX, 3XXX, 5XXX, and 1XXX series [167]. However, these contradictions are not surprising given the fact that recent publications have reported the inadequacy of only using  $E_{\text{pitting}}$  to indicate the relative susceptibility to pitting corrosion of some passive alloys [112], [168]. Particularly, the addition of Cu to AAs has been observed to increase  $E_{\text{pitting}}$ , which may give the impression of superior pitting corrosion resistance. Nevertheless, optical analysis has evidenced an increase in the pitting damage with Cu addition in AAs [169]. From an extensive study of the corrosion resistance of several AAs ranging from 2XXX to 7XXX series, Uyime Donatus concluded that AAs develop severe localized corrosion at values close or equal to their OCP followed by passivation mainly on non-pitting sites [170]. Thus, it should be noted that there is a possibility that the anodic dissolution of Al takes place before the passive region.

Besides the conventional measure of  $E_{\text{pitting}}$ , the shape of anodic polarization curves provides useful information about the corrosion behaviour of metals [171], [172]. Generally speaking, different zones can be observed in the anodic branch of PDP curves: the active, passive, and trans-passive regions. In the *active region* the current increases with the rise of potential which indicates that oxidation takes place. In the *passive region*, the corrosion rate is reduced and the slope (V vs. i) significantly increases. Finally, in the *trans-passive region*, the passive film is broken down and the current suddenly increases. This behaviour is reflected in the PDP curves as a plateau and occurs after the passive region [173]. To have a deeper understanding of the corrosion behaviour and corrosion mechanisms on the evaluated specimens, we can now re-examine and magnify the

obtained PDP curves. The PDP anodic branches are presented in **Figure 3-17**. These results revealed 3 different trends:

i) AA 1100 did not exhibit a passive region, thus there is no  $E_{\text{pitting}}$ . The anodic current density continuously increased with the positive shift of applied potential, indicating active dissolution. As expected from the literature, the pure  $\text{Al}_2\text{O}_3$  that forms the oxide layer of AA1100 is not stable at low pH and high potentials. Therefore, during anodic polarization the protective oxide film dissolves, exposing the bare metal surface and promoting active corrosion at all anodic potentials. It has been observed that Al dissolution is most uniform in pure Al than highly alloyed Al due to its low surface roughness, and high uniformity in solid solution concentration [174]. Several published reports show active dissolution of AAs under specific conditions [175], [176].

ii) AAs 3003(Mn) and 6061(Mg, Si) showed multiple current density fluctuations below  $E_{\text{pitting}}$ . This phenomenon is known as metastable pitting and is defined as the development of small pits around cathodic particles that passivate rapidly within a few seconds [177].

iii) AAs 2024(Cu), 5052(Mg), and 7075(Zn) revealed two plateaus, which have been reported in the literature and associated with the dissolution of different active phases [178], [122], [123].

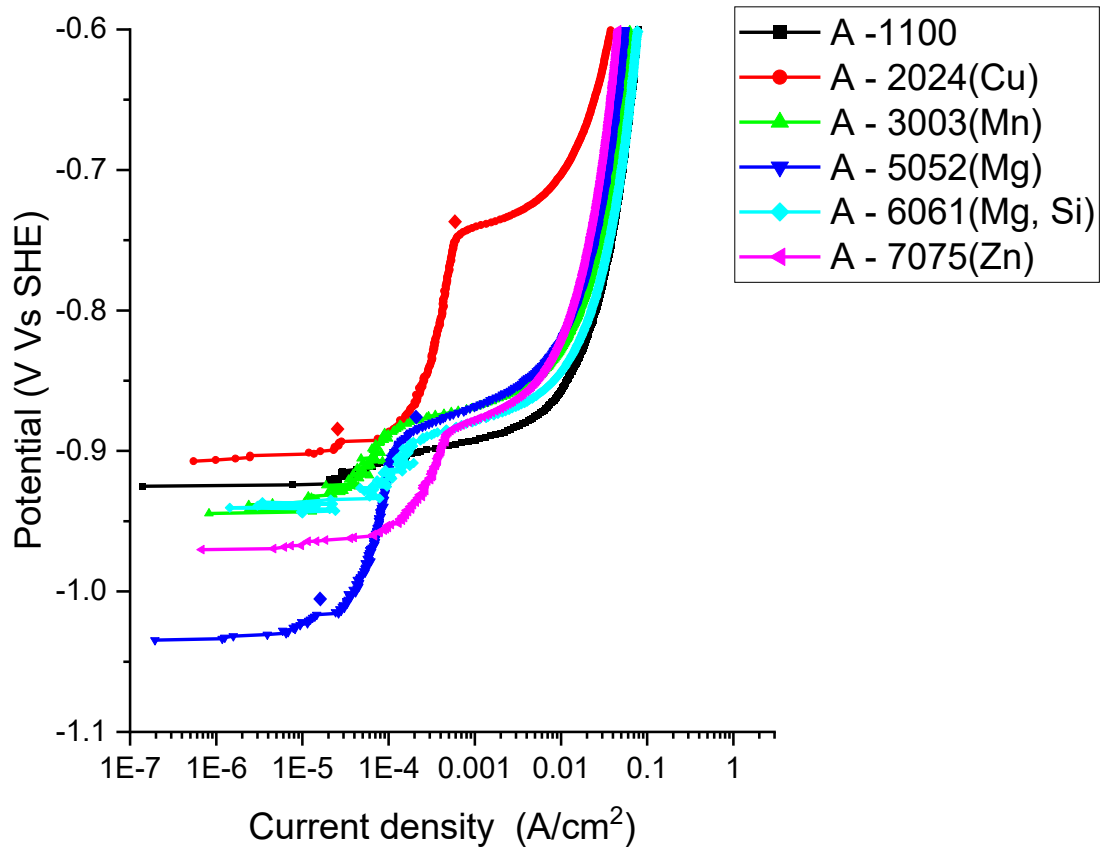


**Figure 3-17.** Anodic branches from PDP curves of AAs in the N<sub>2</sub>-deaerated anolyte (denoted as A-).

According to Mariano Iannuzzi, highly heterogeneous alloys, such as high-strength Al alloys, often show two distinctive pitting potentials ( $E_{\text{pitting1}}$  and  $E_{\text{pitting2}}$ ) [179]. Interestingly, from our experiments, this behaviour is observed only in specimens that possess both, anodic and cathodic IMPs. These findings correlate with what has been found in previous studies [180], [178], [171], [181]. Two pitting potentials on the PDP curves of AAs have been also observed by other authors in aerated and deaerated NaCl solutions. Even though there is still considerable disagreement with

respect to the meaning of each potential,  $E_{\text{pitting1}}$  is often attributed to the dissolution of anodic IMPs present in the AA. Therefore,  $E_{\text{pitting1}}$  could be attributed to the dissolution of  $\text{Al}_2\text{CuMg}$  IMPs on AA2024(Cu) and the dissolution of  $\text{Mg}_2\text{Si}$  IMPs in 5052(Mg) and 7075(Zn).

As seen in **Figure 3-15**, both Mg-containing phases are active to the matrix and are susceptible to active dissolution or Mg dealloying. This is important because the poor resistance to pitting corrosion of AA 2024 (Cu) could be attributed to Mg dealloying from  $\text{Al}_2\text{CuMg}$  IMPs that left Cu-rich remnants. Cu is extremely cathodic to the matrix and has been found to trigger pitting on the surrounding Al matrix. This is commonly referred to as dealloying corrosion and has been proved by rotating ring-disk electrode (RRDE) experiments on  $\text{Al}_2\text{CuMg}$  particles [182]. In contrast, the corrosion of  $\text{Mg}_2\text{Si}$  IMPs is not as detrimental as Cu-containing particles. These particles tend to form oxide/hydroxide corrosion products like  $\text{SiO}_2$ ,  $\text{MgO}$ , and  $\text{Mg}(\text{OH})_2$  which, as it is generally accepted, protect the remnants and reduce the galvanic coupling with the matrix [159], [40], [183]. The anodic dissolution of Al and therefore the initiation of FFC on AAs containing  $\text{Mg}_2\text{Si}$  IMPs, usually does not occur before  $E_{\text{pitting2}}$  and is attributed to pitting on the Al matrix especially around the cathodic IMPs, which remain intact after the corrosion process. Both mechanisms are summarized and shown in **Figure 3-18**.

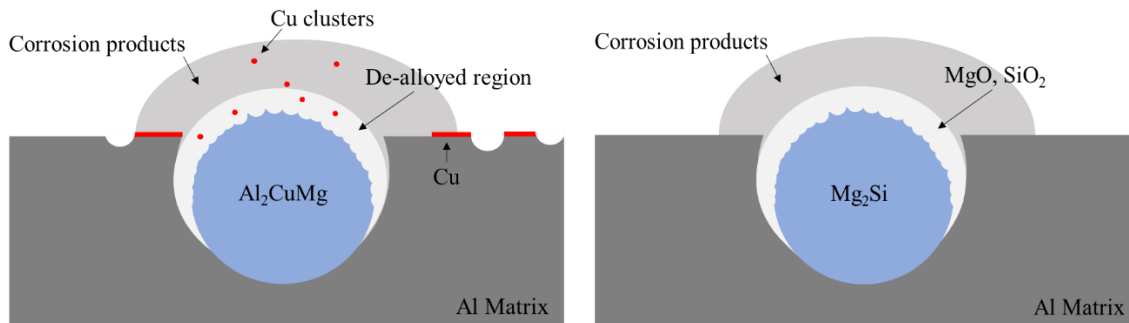


**Figure 3-18.** Schematic representation of corrosion of the anodic IMPs Al<sub>2</sub>CuMg (left) and Mg<sub>2</sub>Si (right).

### 3.3.2 Driving force for propagation

As stated in Chapter 2, every initiation point does not essentially propagate into a filament. In some cases, these points may become occluded cells due to corrosion products. The propagation of a FFC filament from an initiation point is subjected to the presence of a more electrochemically noble site that promotes oxygen reduction when exposed to an aerated environment [18]. Some authors have proposed that the potential difference ( $\Delta E_{\text{corr}}$ ) between the tip of the filament head (anodic site) and the back of the head (cathodic) sites in their respective electrolytes is the driving force for FFC propagation. This  $\Delta E_{\text{corr}}$  has also been found to be related to the number of filaments that emerged from initiation spots [184]. Therefore, the  $E_{\text{corr}}$  of each AA in the anolyte ( $E_{\text{a, corr}}$ ) and the catholyte ( $E_{\text{c, corr}}$ ) were calculated and related to their tendency to FFC propagation.

Usually, the  $E_{\text{corr}}$  value of a metal takes several hours to stabilize when immersed in an aqueous media. For passive metals, like Al, its evolution over time provides important information about the modifications of the natural oxide layer. Jr Davis et al. even described monitoring  $E_{\text{corr}}$  changes over time as a technique to predict the corrosion resistance of AAs [12].

In the present study, the working electrodes were immersed in their respective electrolyte (anolyte and catholyte) for 5 and 2.8 hours respectively to attain stable values. The  $E_{\text{corr}}$  evolution curves of each AAs immersed in the anolyte are shown in **Figure 3-19**. It is observed that the  $E_{\text{corr}}$  changed rapidly at the beginning of the immersion. A reasonable criterion for the steady-state was chosen according to previous literature: a change of less than 5 mV over 30 minutes [185]. Stable values were achieved in less than one hour of immersion for the specimens AAs 1100, 2024 (Cu), 3003 (Mn), 5052 (Mg), and 6061 (Mg, Si) whereas the  $E_{\text{corr}}$  of AA7075 (Zn) reached stability after about 3.8 h of immersion.

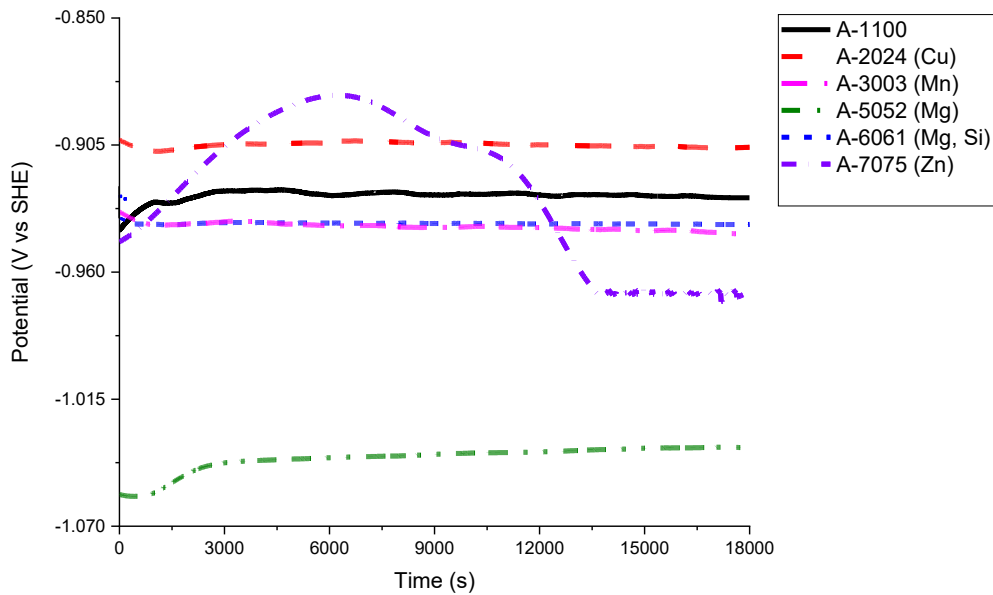


**Figure 3-19.**  $E_{\text{corr}}$  evolution after 18000s of immersion in anolyte (denoted as A-) for the alloys (a) 1100, 2024(Cu), AA3003(Mn), 5052(Mg), 6061(Mg, Si) and 7075(Zn).

Regarding the observed  $E_{\text{corr}}$  evolution curves in **Figure 3-19**, three scenarios were identified and summarized in **Table 3-7**.

- (i) As time advanced, the  $E_{\text{corr}}$  of AAs 1100 and 5052 (Mg) was shifted in the direction of more electropositive values, from -0.94 to -0.93 and -1.05 to -1.01 V vs. SHE, respectively. According to the literature, the rise in potential is commonly observed on alloys that exhibit passivity [186], [187], [188].
- (ii) In the case of AAs 2024 (Cu), 3003 (Mn), and 6061 (Mg, Si)  $E_{\text{corr}}$  values shift towards a more negative potential and then attain a steady value, from -0.90 to -0.91, -0.93 to -0.95 V, and -0.93 to -0.94 V vs. SHE, respectively. This behaviour is often attributed to an increase in the driving force for the corrosion process [189].
- (iii)  $E_{\text{corr}}$  for AA 7075 (Zn) gradually increased as the immersion time increased from -0.94 to -0.88 V vs. SHE, then it decreased until reaching a steady value at -0.96 V vs SHE.

Despite the shapes of the curves, all the specimens reached the steady-state condition, which indicated that a dynamic balance was established between the development of the corrosion activity and the deposit of corrosion products on the surface of AAs [190].

As expected,  $E_{\text{corr}}$  evolution for all the alloys in the catholyte gradually increased over time and then reached stability (**Figure 3-20**). This is a common behaviour on AAs under no corrosive environments where the passive film is stable, and passivation occurs [191].

**Table 3-7.** Summary OCP evolution trend during 5h of immersion in N<sub>2</sub> de-aerated anolyte [40], [192], [112], [191], [188].

AAs in the anolyte	Observation	Description	OCP vs. time curve shape
1100, 5052 (Mg)	OCP gradually shifts to more positive values	Passivation occurs	
2024 (Cu), 3003 (Mn), 6061(Mg, Si)	OCP gradually shifts to more negative values	Corrosion occurs	
7075 (Zn)	OCP rises and then drops	Passivation followed by corrosion	

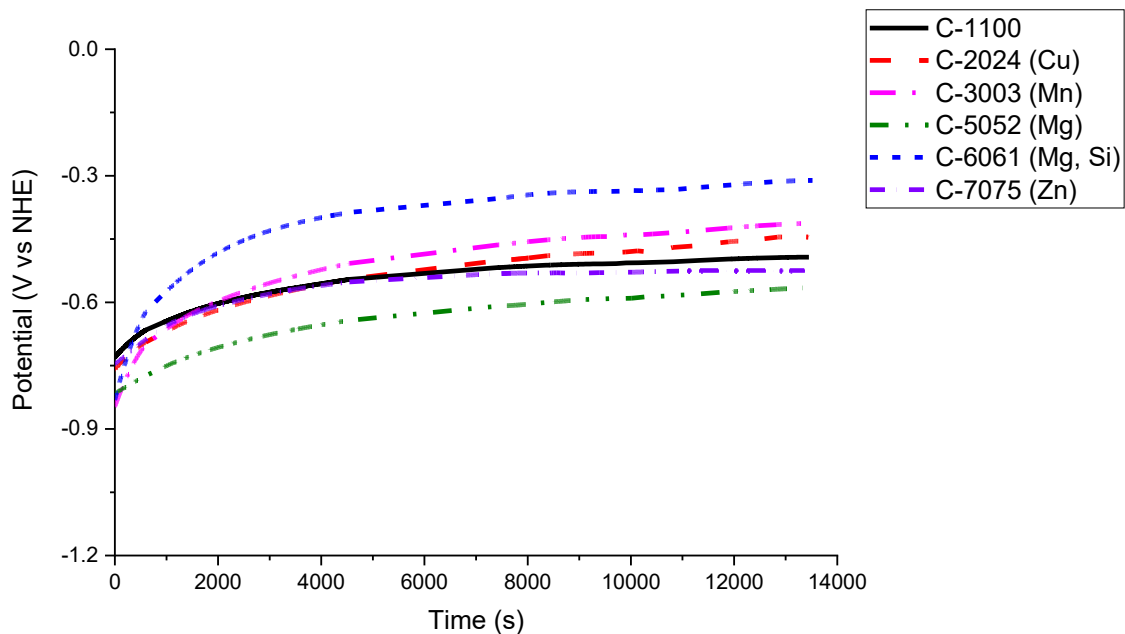


**Figure 3-20.**  $E_{\text{corr}}$  evolution during 13800 s of immersion in catholyte (denoted as C-) for the alloys (a) 1100, 2024(Cu), AA3003(Mn), 5052(Mg), 6061(Mg, Si), and 7075(Zn).

**Figure 3-21** presents the averaged OCP values of the evaluated AAs in the anolyte ( $E_{a, \text{corr}}$ ) and catholyte ( $E_{c, \text{corr}}$ ), as well as the potential difference  $\Delta E_{\text{corr}} (=E_{c, \text{corr}} - E_{a, \text{corr}})$  of each alloy at room temperature. As expected, the  $E_{\text{corr}}$  values in the aerated catholyte are more positive compared to those measured in the anolyte. The presence of oxygen and low concentration of corrosive species like  $\text{H}^+$  and  $\text{Cl}^-$  in the catholyte enhances the passivation and stability of the passive films. As stated in Chapter 2, the protective film is usually nobler than the metal substrate. While in deaerated and chlorinated acid solution the Al surfaces are less noble due to the instability of the oxide layer and high conductivity of the electrolyte [193]. These results are consistent with the well-known  $E_{\text{corr}}$  profile on Al FFC filaments, in which  $E_{\text{corr}}$  values tend to be lower in the direction of the tail and higher towards the trailing edge [191].

The measured corrosion potentials exhibited a variation of 0.2 and 0.12 V between the highest and the lowest value in the catholyte and the anolyte, respectively. By comparing the  $E_{\text{corr}}$  values obtained for all the specimens, it can be observed that AA 5052 (Mg) exhibited the lowest  $E_{\text{corr}}$  value in both electrolytes. Whereas AAs 2024 (Cu) and 6061 (Mg, Si) exhibited nobler  $E_{\text{corr}}$  values in the anolyte and catholyte respectively. The results from **Figure 3-21** suggest that alloying elements can significantly change the potential of AAs in both directions. However, the  $E_{\text{corr}}$  values of different alloys in each media cannot be directly compared and relate to their corrosion susceptibility, same as it is for steel [194], [112].

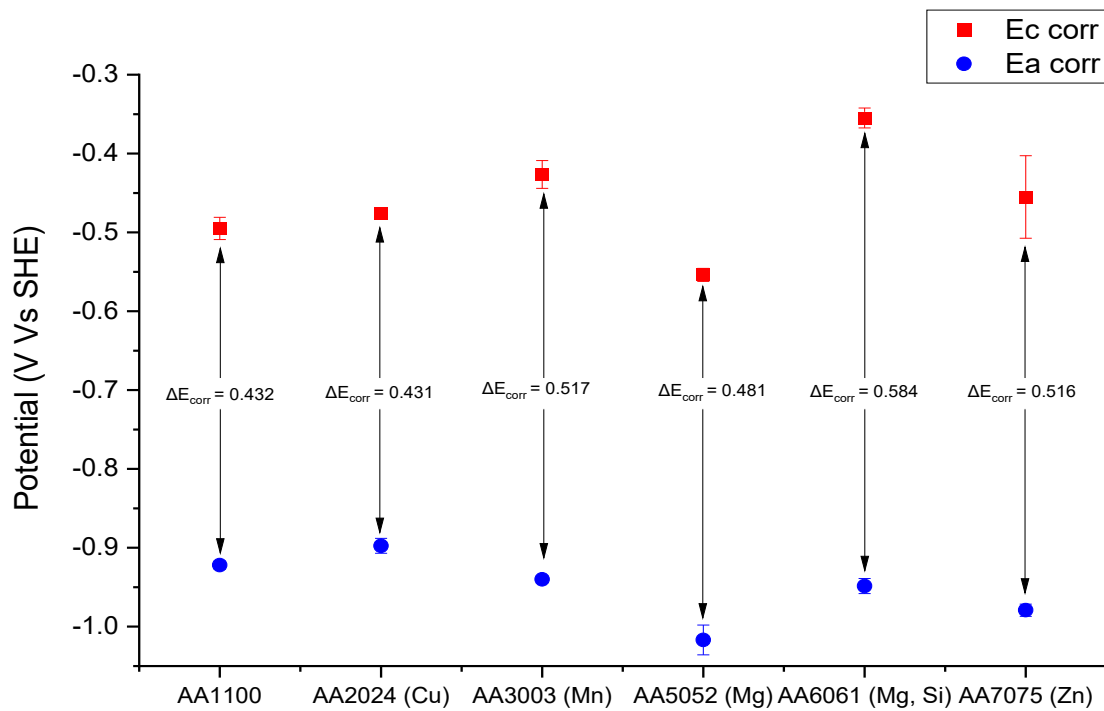


**Figure 3-21.**  $E_{\text{corr}}$  and the driving force  $\Delta E_{\text{corr}}$  values of AAs in the  $\text{N}_2$ -deaerated anolyte and aerated catholyte.

As shown in **Figure 3-21**, the driving force for FFC propagation follows the trend AA 6061 (Mg, Si) > 7075 (Zn), 3003 (Mn) > 5052 (Mg) > 2024 (Cu), 1100. AAs with a low tendency to FFC propagation like 1100 and 5052 (Mg) exhibited passivation in both electrolytes; A different scenario was observed for AAs 3003 (Mn), 6061 (Mg, Si), and 7075 (Zn), which showed a higher driving force for propagation. These alloys exhibited de-passivation in the anolyte but passivation in the catholyte. Thus, a surface that enhances the anodic reaction in the anolyte and an oxide film that is sustainable for cathodic reactions in the catholyte results in a higher  $\Delta E_{\text{corr}}$  and a higher tendency for FFC propagation. The role of the natural oxide film on the FFC behaviour of Al was also identified by Huirset et al. [62]. The case of AA2024 (Cu) is always special and attention that must be paid to study Cu-containing AAs has been well documented and highlighted [112]. Even though there was no passivation of the AA2024 (Cu) surface in the anolyte, the measured  $E_{\text{corr}}$  values were high enough to keep a small  $\Delta E_{\text{corr}}$ . Additionally, alloys with a higher tendency to FFC propagation exhibited the highest  $E_{\text{c, corr}}$  while those with a low tendency to FFC propagation exhibited lower values. This indicates that the driving force  $\Delta E_{\text{corr}}$  is mainly influenced by the cathodic reaction in the back of the filament head.

### 3.3.3 Kinetics of propagation

The  $E_{\text{corr}}$  measurements in anolyte and catholyte, indicate that  $E_{\text{c, corr}}$  is consistently higher than  $E_{\text{a, corr}}$  for all the samples ( $E_{\text{c, corr}} > E_{\text{a, corr}}$ ), thus, the flux of electrons goes from the tip of the filament to the back of the head (simulated in the anolyte and catholyte respectively). However, these results do not provide information about the speed of FFC propagation on different AAs. This kinetic information is available via analysis of the polarization curves obtained in the anolyte and catholyte by applying the conservation law of charge to the system, as described in Equation 3.1.

$$\sum i_A = \sum i_C \quad \text{Eq 3.1}$$

At a mixed point, the total electrons released from the anode are equal to the total electrons gained by the cathode. It is worth mentioning that the surface area of the anodic site is much smaller than that of the cathodic site. Conventionally, an effective cathode/anode area ratio is assumed to be 100 [31]. Herein, the current density on the measured PDP curves in the catholyte is multiplied by a factor of 100. The current density at which the conservation of charge is met is known as,  $i_{\text{FFC}}$ , and it is often related to the final length of FFC filaments.

**Figure 3-22** presents the polarization curves of each alloy in the anolyte and catholyte at room temperature. The rate of FFC propagation is determined by the anodic current density at the mixed potential (Fedrizzi et al., 1998). It is observed that  $i_{\text{FFC}}$  (mA/cm<sup>2</sup>) follows the trend 7075 (Zn) > 6061 (Mg, Si) > 3003 (Mn) > 5052 (Mg) > 1100 > 2024 (Cu). These results go with the tendency in which AAs 7075 (Zn), 6061 (Mg, Si), and 3003 (Mn) have higher values than AAs 5052 (Mg), 2024 (Cu), and 1100. Therefore, longer filaments are expected to take place in that first group.

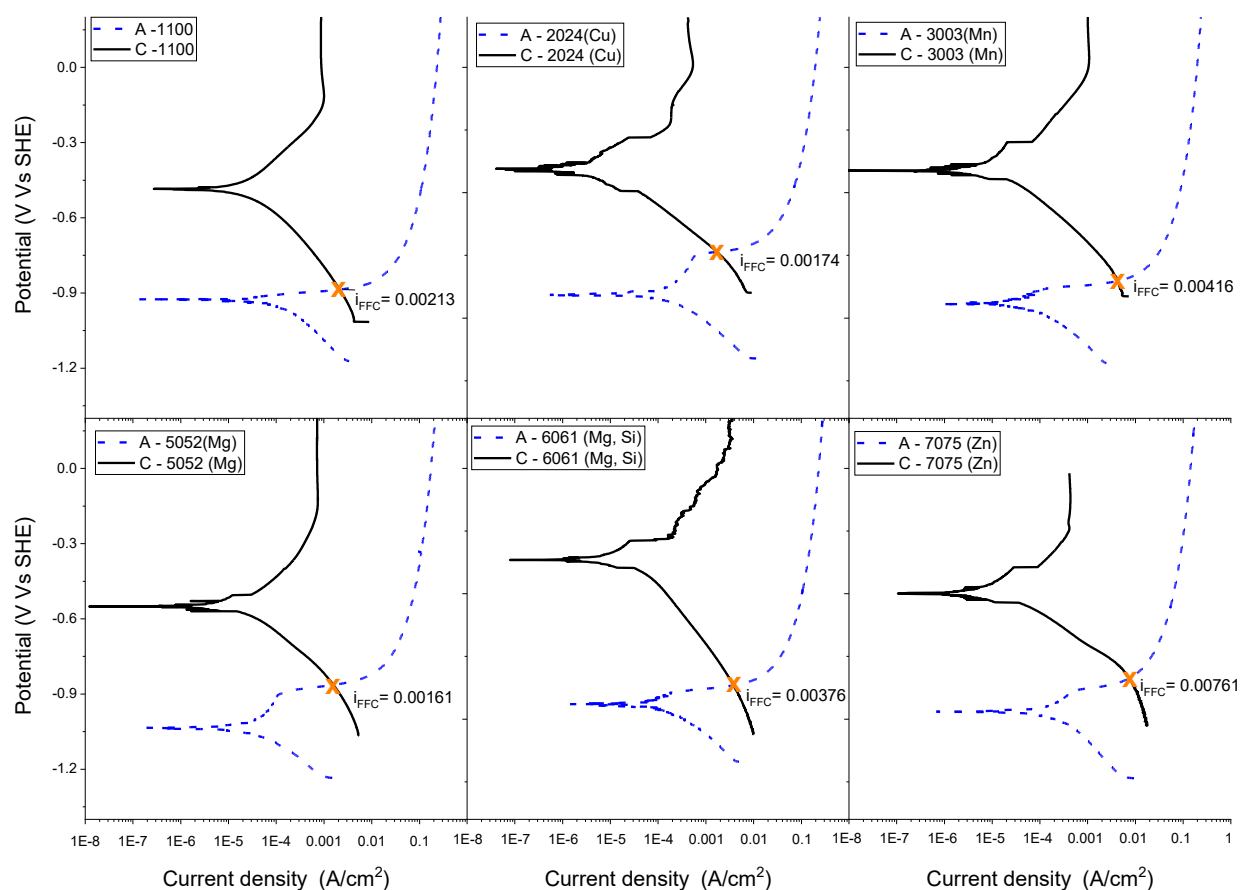


**Figure 3-22.** Polarization curves of AAs obtained in the  $N_2$ -deaerated anolyte (denoted as A-), and in the aerated catholyte (denoted as C-) at 25 °C. FFC current density ( $i_{FFC}$ ) is taken as the intercept of the anodic and cathodic curves assuming an effective cathode/anode area ratio of 100.

When the formation of the mobile head occurs, the dissolution rate at the tip of the head is driven to increase from the corrosion current ( $i_{corr}$ ) in the anolyte to  $i_{FFC}$ . The rate increases because the cathodic kinetics of the cathode (back of the head) are demanding electrons. **Table 3-8** lists the results for  $i_{FFC}$  and  $i_{corr}$  measured in the anolyte by the extrapolation of the cathodic branch method as it performed linear behaviour for over 100 mV. This method was suggested by McCafferty and widely used by other authors [195], [196], [197]. It is important to notice that  $i_{FFC}$  doesn't follow

any trend along with  $i_{\text{corr}}$  in the anolyte. However, examining the cathodic branches of the PDP curves in the catholyte presented in **Figure 3-23**, the alloys with higher propagation kinetics ( $i_{\text{FFC}}$ ) exhibited higher current densities. The above confirms that the cathodic reduction of oxygen in the catholyte controls the rate of anodic dissolution and the advance of the filament. This has also been confirmed previously [198], [78], [199].

**Table 3-8.**  $i_{\text{FFC}}$  and  $i_{\text{corr}}$  measured in the anolyte by the extrapolation of the cathodic branch method.

AAs	$i_{\text{corr}}$ (A/cm <sup>2</sup> )	$i_{\text{FFC}}$ (A/cm <sup>2</sup> )
AA1100	1.30E-04	2.50E-03 ±7.1E-04
AA2024 (Cu)	2.24E-04	1.03E-03 ±1.8E-05
AA3003 (Mn)	9.30E-05	3.95E-03 ±3.5E-04
AA5052 (Mg)	4.40E-05	2.09E-03 ±7.2E-04
AA6061 (Mg, Si)	1.50E-04	4.54E-03 ±1E-03
AA7075 (Zn)	2.58E-04	7.55E-03 ±3.5E-4

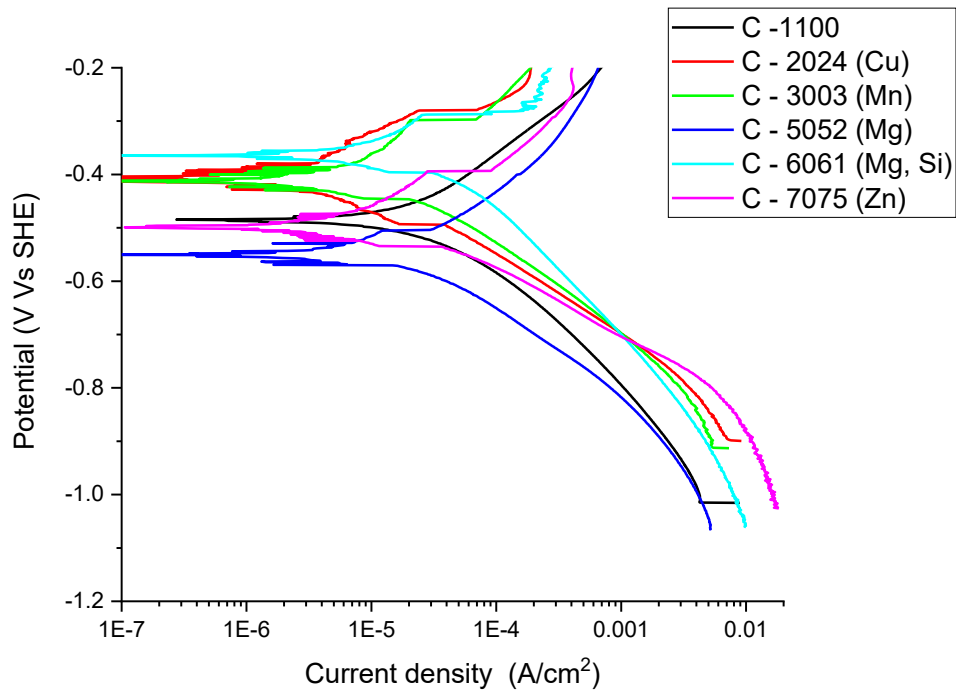


**Figure 3-23.** PDP curves of the specimens in the aerated at 25 °C.

### 3.4 SUMMARY

In summary, the values of  $\Delta E_{PR}$ ,  $\Delta E_{corr}$ , and  $i_{FFC}$  for all the alloys are presented in **Table 3-9**, conclusions are below:

- The initiation stage of FFC ( $\Delta E_{PR}$ ) depends on the presence of IMPs that promote micro galvanic coupling that weakens the naturally formed oxide films of AAs and causes the development of FFC initiation spots.
- The tendency to FFC propagation ( $\Delta E_{corr}$ ) is not affected significantly by IMPs because  $E_{corr}$  values are mainly attributed to the composition of the matrix, and the passive film stability in

both electrolytes (Joseph R. Davis). (AA 6 061 (Mg, Si) > 7075 (Zn), 3003 (Mn) > 5052 (Mg) > 2024 (Cu), 1100

- Finally, the kinetics of propagation ( $i_{\text{FFC}}$ ) is mainly controlled by the reduction of oxygen in the local cathode. Numerous FFC filaments with long lengths are expected in the alloys with higher  $\Delta E_{\text{corr}}$  and  $i_{\text{FFC}}$ , which correspond to AAs 3003 (Mn), 6061(Mg, Si) and 7075 (Zn).

**Table 3-9.** Electrochemical parameters of FFC for the AAs evaluated.

AA	$\Delta E_{\text{corr}}$ (V) ( $E_{\text{a, corr}} - E_{\text{c, corr}}$ )	$\Delta E_{\text{PR}}$ (V) ( $E_{\text{pitting}} - E_{\text{a, corr}}$ )	$i_{\text{FFC}}$ (A/cm <sup>2</sup> )
1100	0.045	0.432	0.0025
2024 (Cu)	0.170	0.431	0.0010
3003 (Mn)	0.079	0.517	0.0039
5052 (Mg)	0.168	0.481	0.0020
6061 (Mg, Si)	0.059	0.584	0.0045
7075 (Zn)	0.089	0.516	0.0075

# **CHAPTER 4 ELECTROCHEMICAL STUDY OF ANODIZED ALUMINUM FILIFORM CORROSION**

Chapter 3 discussed the susceptibility of freshly polished AAs to FFC. However, commercially coated AAs usually require a surface stabilization treatment before coating. Stabilization is achieved through applying different pre-treatments mentioned in Chapter 2 section 2.3.3. The present chapter has two main objectives: to investigate the effects of anodizing on the FFC behaviour of AAs selected in Chapter 3 by electrochemical techniques and to validate the electrochemical results obtained for bare and anodized samples via accelerated exposure tests. To do so, AA1100, AA2024 (Cu), AA3003 (Mn), AA5052 (Mg), AA 6061 (Mg, Si) and AA 7075 (Zn) were pretreated (electropolished, anodized, and sealed), and electrochemical measurements were performed afterwards. In addition, bare and anodized specimens were coated with epoxy resin and subjected to an accelerated exposure test (80 % RH, 40 °C) for 1000 h. The present chapter is divided into 4 sections: experimental procedures, anodic film characterization, electrochemical parameters of FFC on anodized AAs, and accelerated exposure test results.

## **4.1 EXPERIMENTAL PROCEDURES**

### **4.1.1 Materials and Chemicals**

The materials evaluated were the AAs selected in Chapter 3: AA1100, AA2024 (Cu), AA3003 (Mn), AA5052 (Mg), AA 6061 (Mg, Si) and AA 7075 (Zn). The composition of these alloys is outlined in **Table 3-1**. Additionally, a series of solutions were carefully prepared and used in this

study. Perchloric acid ( $\text{HClO}_4$ ) and ethanol ( $\text{C}_2\text{H}_5\text{OH}$ ) were used to prepare the electrolyte for the electrochemical polishing process. DI and phosphoric acid ( $\text{H}_3\text{PO}_4$ ) were used to prepare the anodizing solution. Moreover, as reported in Chapter 3, DI water,  $\text{HCl}$ ,  $\text{AlCl}_3$ ,  $\text{NaH}_2\text{PO}_4$  and  $\text{Na}_2\text{HPO}_4$  were used to prepare the electrolytes for the electrochemical measurements.

## 4.1.2 Methods

### 4.1.2.1 Samples preparation

AA samples were abraded using successive grades of SiC papers down to 1200 grit, degreased with ethanol via sonication and rinsed with acetone. In this study, the pre-treatment of AAs' surface consisted of 3 steps: electropolishing, anodizing, and sealing. Electropolishing and anodizing were carried out using a two-electrode electrochemical cell (shown in **Figure 2-9**) with a thermostatic water jacket, a platinum (Pt) mesh as the CE, and the AA substrate as the WE with a surface area of  $1 \text{ cm}^2$ . The DC power supply used was a Letour LT6005H.

**Electropolishing** was carried out in a 1:4 volume solution of  $\text{HClO}_4$ :  $\text{C}_2\text{H}_5\text{OH}$  under vigorous magnetic stirring (1500 rpm), at  $10 \text{ }^\circ\text{C}$ , and a DC voltage of 8 V for 2 minutes. The samples were sequentially cleaned with DI water and then anodized. **Anodizing** took place in a 100 g/L  $\text{H}_2\text{SO}_4$  solution at  $18 \text{ }^\circ\text{C}$  under a constant current density of  $1 \text{ A/dm}^2$  for 30 minutes at a stirring rate of 600 rpm. Finally, the hydrothermal **Sealing** process was performed by submerging the AA samples in boiling DI water for 30 minutes and dried in air. **Figure 4-1** shows a schematic illustration of the anodized AAs preparation. For simplification purposes, AAs that were electropolished, anodized and sealed will be referred to as **a-AAs** while the bare alloys will be identified as AAs in

this work. Furthermore, anodizing will refer to the entire process (electropolishing, anodizing and sealing).

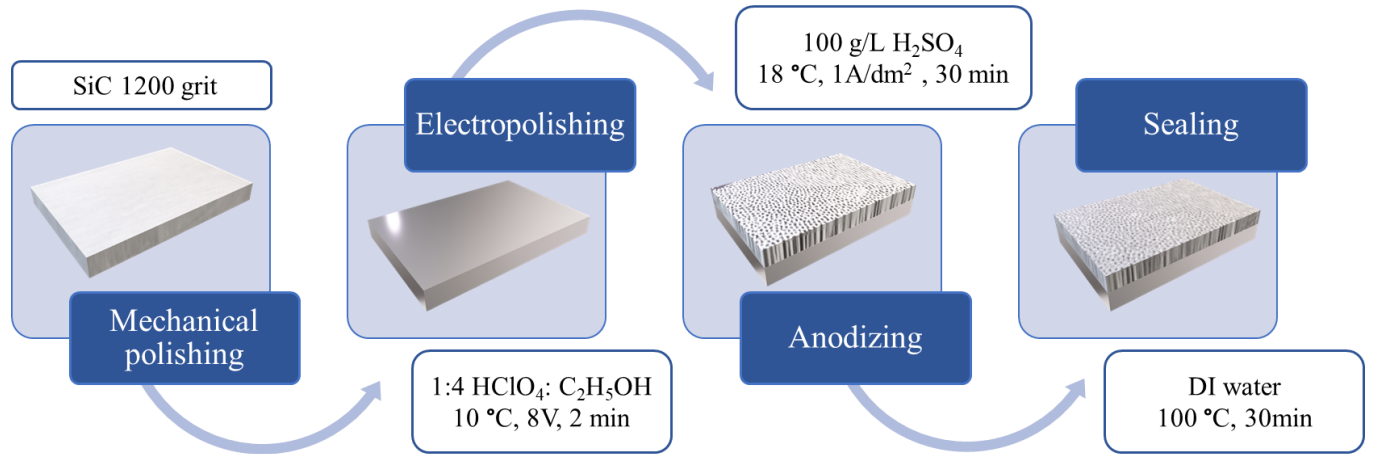


**Figure 4-1.** Process diagram of a-AAs preparation.

#### 4.1.2.2 Anodic film characterization

The characterization of the a-AAs was done using SE and BSE -SEM in order to gather information that will help to explain the FFC susceptibility of various a-AAs. SEM images were taken using a Tescan scanning electron microscope. Average defect size ( $\mu\text{m}^2$ ), defect density ( $\mu\text{m}^{-2}$ ) and percentage of the affected area were calculated for all the samples using the software Image J97.0.188 (Academic) from OriginLab Corporation.

#### 4.1.2.3 Electrochemical measurements

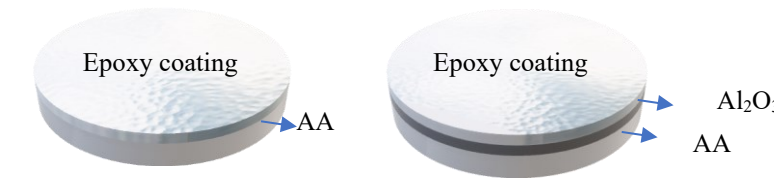
Prior to the experiment, a-AAs were washed with DI water and dried in air. The electrochemical measurements were carried out as described in Chapter 3.1.2.2.

#### 4.1.2.4 Accelerated exposure testing

Bare and anodized AA disks with a diameter of 2.5 cm were cleaned with ethanol and dried in air. A clear epoxy coating was applied on the surface of the samples using a spin-coater (2000 rpm for 4 minutes). The epoxy mixture was prepared by mixing the commercial epoxy resin (west system 105) with a hardener agent (west system 205) in a 2 : 1 ratio. After preparation, the coating was hardened for 7 days at room temperature. Before accelerated exposure testing, the coated specimens were scribed using a tungsten carbide scribing tip that penetrated the organic coating and oxide layer on the metal surface, leaving a uniform bright line with a length of about 1 cm. A prepared sample is shown in **Figure 4-2** (a), the edges of the samples were sealed with a commercial lacquer to avoid FFC to occur in undesired places. Three samples were prepared for each AA or a-AA. The evaluated specimens are listed in **Table 4-1**.

**Table 4-1.** Accelerated exposure test evaluated specimens.

Bare	Anodized
AA1100	a - AA1100
AA2024 (Cu)	a - AA2024 (Cu)
AA3003 (Mn)	a - AA2003 (Mn)
AA5052 (Mg)	a - AA5052 (Mg)
AA6061 (Mg, Si)	a - AA6061 (Mg, Si)



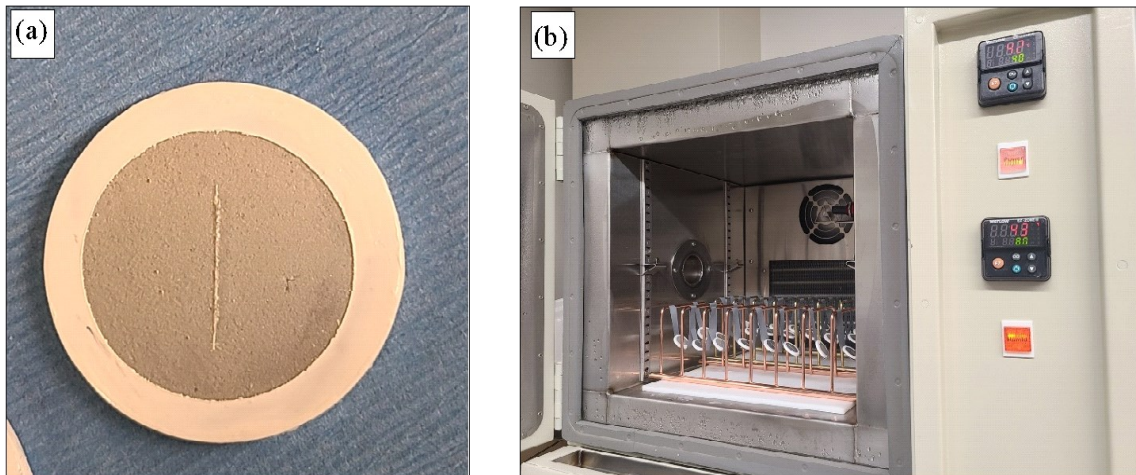


**Figure 4-2.** (a) An epoxy coated AA before accelerated exposure testing, note that the edges are covered and a scribe was made in the center of the disk, and (b) samples placed in a humidity chamber.

FFC was initiated by immersing the specimens in a saturated  $\text{AlCl}_3$  solution for two hours. After activation, the disks were washed with DI water and placed in an environmental testing chamber (Benchtop) at 80 % RH at 40 °C for 1000 h, as shown in **Figure 4-2** (b). In order to evaluate FFC resistance of AAs and a-AAs two parameters were defined (i.e., number of threads (N) and length of the filaments (L)), and calculated by visual examination with naked eyes and OM. All the reported results are average values, and the standard deviations are also reported. The error margins for the qualitative parameters N and L are subjected to human interpretation which is inevitable in accelerated exposure tests as mentioned in Chapter 2, section 2.3.4.1.

## 4.2 ANODIC FILM CHARACTERIZATION

### 4.2.1 General observations

a-AA samples were successfully prepared by the process described in **Figure 4-1**. The changes on the sample's surfaces after each process were evident and occurred similarly on all AA samples.

**Figure 4-3** shows a picture of AA2024 (Cu) after (a) electropolishing and after (b) anodizing.

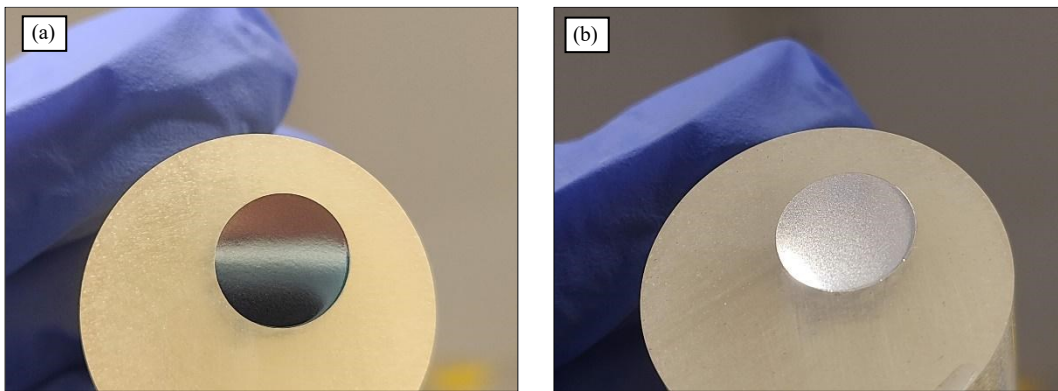


**Figure 4-3.** AA2024 (Cu) after (a) electropolishing and (b) anodizing.

A shiny appearance was consistently observed in all the samples after electropolishing. Guang Yang reported that the final properties of the anodized surface were subject to the formation and dissolution of an oxide layer, of which the function is to dissolve the macroscopic roughness in a process known as anodic level [200]. Such a layer was observed in the present study and shown in **Figure 4-4**. The shiny appearance was due to the applied high current density and the electrolyte composition that caused the crests closer to the top surface to be dissolved faster than the valleys; resulting in smoothing the AA surface [201].

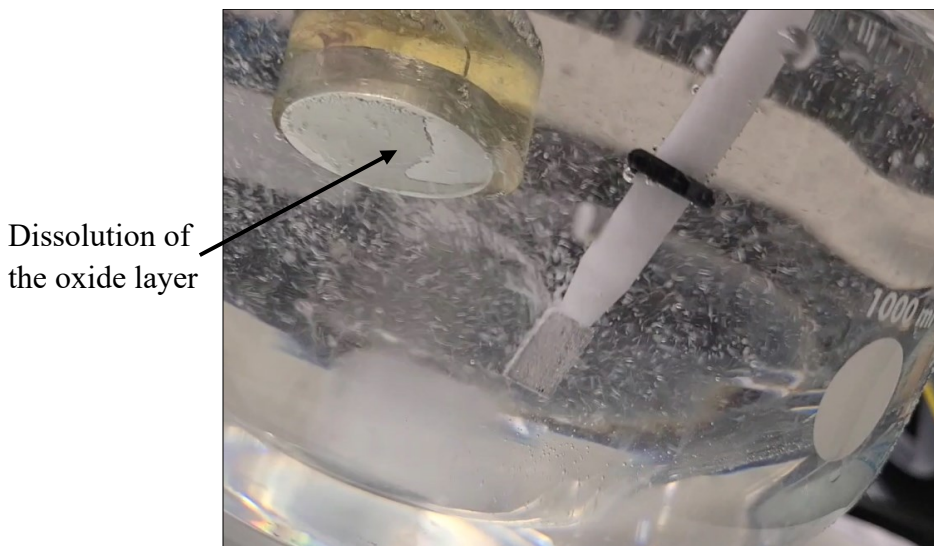


**Figure 4-4.** Formation and dissolution of an oxide layer on AA7075 (Zn) during the electropolishing process in  $\text{HClO}_4$ :  $\text{C}_2\text{H}_5\text{OH}$  at  $10\text{ }^\circ\text{C}$  with a DC voltage of 8 V.

After the anodizing process, every a-AA sample exhibited a uniform gray matte finish, consistent with the development of an anodic oxide layer (see **Figure 4-3 (b)**). During anodizing, a protective porous oxide film is generated on the AA surface. In this thesis, the term “anodic film” refers to the oxide film developed by the anodizing process and the term “natural oxide film” refers to the spontaneously formed oxide film when AAs are exposed to environmental conditions.

#### **4.2.2 Anodic film morphology**

The final properties of anodic films are strongly linked with the anodization parameters and the alloy composition. As demonstrated in **Figure 3-15**, the Al-rich matrix and IMPs present on AAs surface responded differently to the electrochemical conditions. Therefore, the morphology and barrier properties of anodic films are expected to variate from one alloy to another. **Figure 4-5** shows the SE SEM micrographs for (a) a-AA1100, (b) a-AA2024 (Cu), (c) a-AA3003 (Mn), (d) a-AA5052 (Mg), (e) a-AA6061 (Mg, Si) and (f) a-AA7075 (Zn). Except for a-AA5052, numerous

holes and surface defects were observed in the anodic layers formed. a-AA1100 exhibited the second most uniform anodic film with an average defect area of 7.8% and defect density of 0.00157 (number of defects per  $\mu\text{m}^2$ , i.e.,  $\mu\text{m}^{-2}$ ). The micrographs for a-AA3003 (Mn) and a-AA 6061 (Mg, Si) were similar, and the calculated parameters were close as well. The defects on a-AA7075 (Zn) are relatively larger ones with an average size of 107.12  $\mu\text{m}^2$ . On the other hand, the a-AA2024 (Cu) sample showed smaller defects with an average size of 3.15  $\mu\text{m}$ . The average defect size ( $\mu\text{m}^2$ ), defect density ( $\mu\text{m}^{-2}$ ) and percentage of affected area calculated for all the samples are presented in **Table 4-2**.

**Table 4-2.** Average defect size ( $\mu\text{m}^2$ ), defect density ( $\mu\text{m}^{-2}$ ) and percentage of the defect area calculated for a-AA samples.

	<b>Average size (<math>\mu\text{m}^2</math>)</b>	<b>Defect density (<math>\mu\text{m}^{-2}</math>)</b>	<b>Defect area (%)</b>
<b>a - AA1100</b>	58.35	0.00157	7.80
<b>a - AA2024</b>	3.15	0.00793	2.28
<b>a - AA3003</b>	35.80	0.00235	10.23
<b>a -AA 5052</b>	-	-	0
<b>a - AA6061</b>	47.16	0.00378	13.79
<b>a - AA7075</b>	107.12	0.00120	11.81

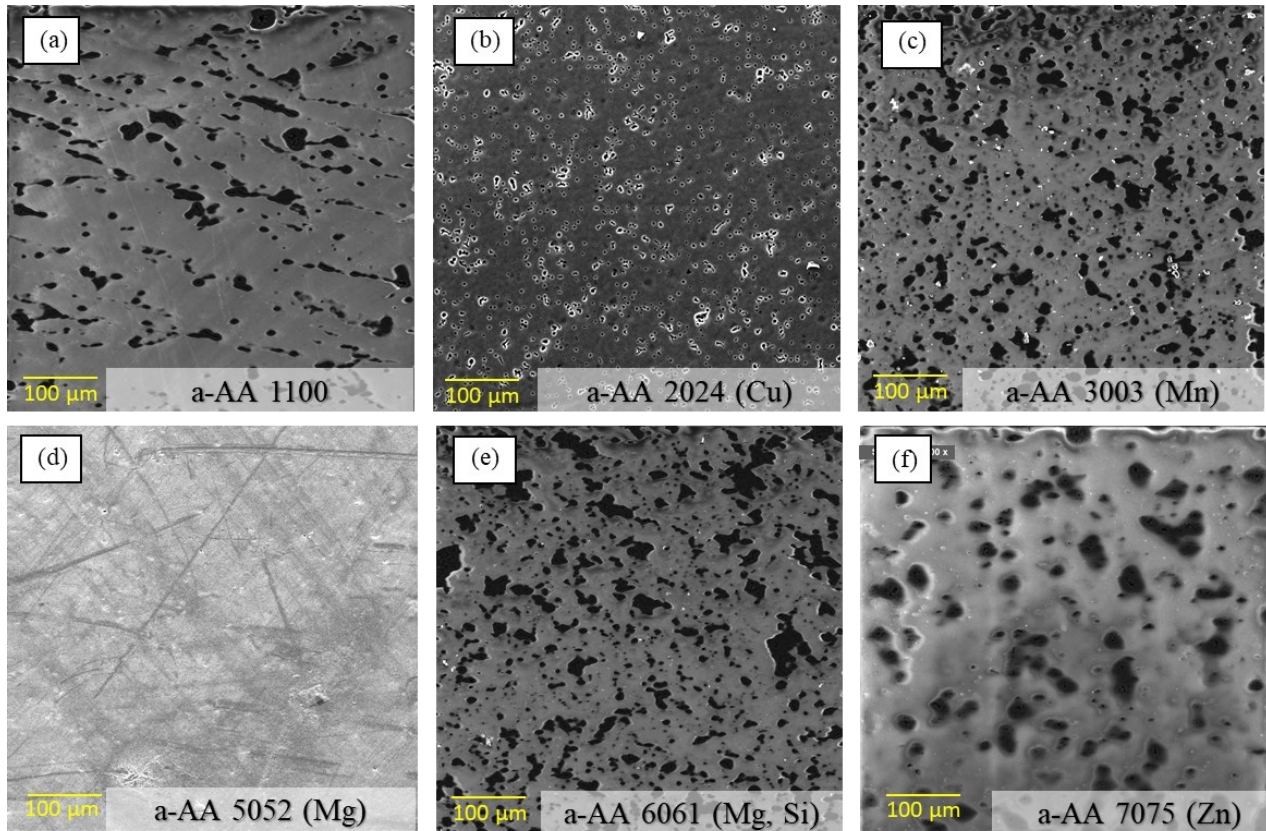


**Figure 4-5.** Surface SE-SEM images of anodic films for a-AAs (a) 1100, (b) 2024 (Cu), (c) 3003 (Mn), (d) 5052 (Mg), (e) 6061 (Mg, Si) and (f) 7075 (Zn).

Through the use of SE and BSE images, it was possible to identify a preferential distribution of defects on the anodic films. **Figure 4-6** (a) and (b), present superimposed pictures of SE (yellow) and BSE (blue) SEM images after contour image processing for (a) a-AA2024 (Cu) and (b) a-AA3003(Mn). The SE image provides morphological contrast, therefore the yellow contour allowed us to identify defects and holes on the anodic film surface, whereas the BSE image prioritizes composition contrast, thus the blue contour revealed composition changes most likely due to the presence of IMP. In the a-AA samples for 1100, 3003 (Mn), 6061 (Mg, Si) and 7075 (Zn), the defects were found to surround numerous IMPs and seen to occur preferentially at spots

with a high density of IMP. For the sake of simplicity, it was decided to show the superimposed images only for a-AA3003(Mn) here. However, it is important to clarify that the other mentioned a-AAs (1100), 6061 (Mg, Si) and 7075 (Zn)) revealed the same behaviour.

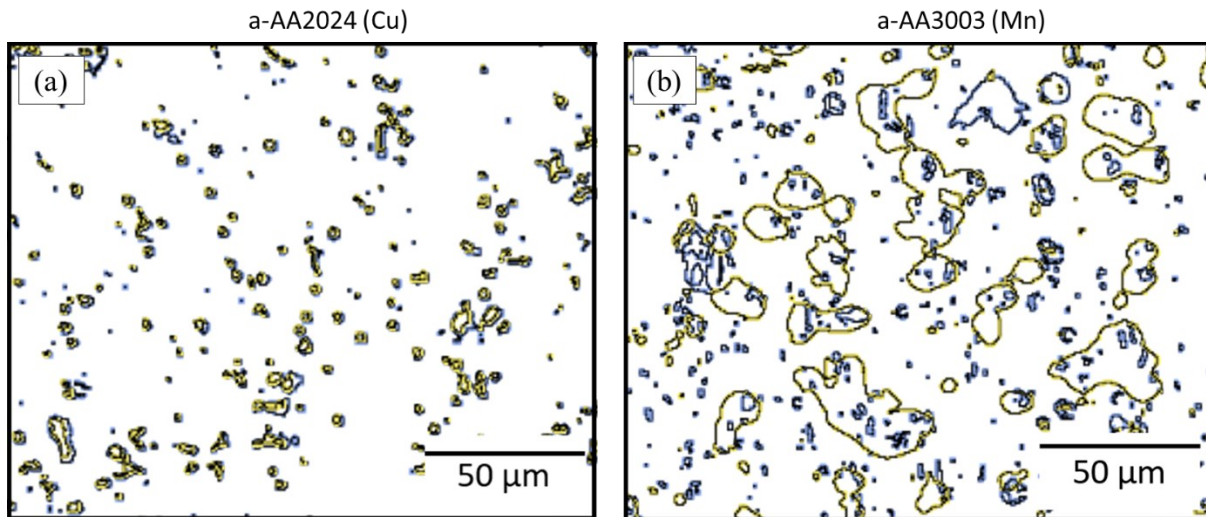


**Figure 4-6.** Superposed images of SE (yellow) and BSE (blue) SEM micrographs after contour image processing for (a) a-AA2024 (Cu) and (b) a-AA3003(Mn).

Till here, a-AA2024 (Cu) was left out. Interestingly, different behaviour is seen only on a-AA2024 (Cu), in which defects on the anodic film corresponded to the presence of individual small IMPs; this explains the small defect size previously reported. A significant difference between a-AA2024 (Cu) and the rest of the alloys is that a-AA2024 (Cu) does not have Si or Si-containing IMPs. In fact, it mainly possesses Cu-containing IMPs. These results confirm that the morphology and quality of obtained anodic films are not only affected by the anodizing process, but also by the IMPs of AAs.

While the chemical composition of the AA matrix has been reported not to significantly affect the morphology of the anodic film [40], the influence of IMPs on its growth rate and morphology has been well documented. Recent findings on aerospace alloys suggest that IMPs can be oxidized at a greater or lower rate than the matrix [202], [203]. Various authors have reported that Si and Al–Fe–Si particles could delay the growth of anodic layers in the vicinity of the particles [204], [205]. This is a potential reason for the large defect size found in all Si-containing AAs. Conversely, Cu and Fe containing IMPs have been identified to be simultaneously oxidized with the matrix. These IMPs can lead to anodic films with local enrichment of Cu–O and Fe–O in the metal/oxide interface. This results in a film with modified electrical properties that support strong oxygen evolution [205]. Oxygen evolution causes the rupture of the anodic film, contributing to high defect density. It is thus reasonable to assume that the anodic film morphology observed in a-AAs 2024 (Cu) can be attributed to the as-described phenomenon. Moreover, the rupture of oxides provides a path for electrolyte penetration and compromises the corrosion resistance of anodized AAs [206]. Furthermore, the Mg-containing IMPs are the most reactive ones in response to anodizing and have been found to be enriched on the anodic layer and in turn, slightly increase the thickness of the anodic layer [207].

### **4.3 ELECTROCHEMICAL PARAMETERS OF FFC**

The three FFC electrochemical parameters: resistance to FFC initiation ( $\Delta E_{PR}$ , V), driving force for propagation ( $\Delta E_{corr}$ , V), and FFC kinetics of propagation ( $i_{FFC}$ , mA/cm<sup>2</sup>) that were defined in **Table 3-5** and calculated in Chapter 3, section 3.3 for AA samples were determined for a-AA specimens.

These three parameters have been proposed in the literature in order to determine the susceptibility of AAs to the different stages of FFC mechanism (initiation, propagation and growing). FFC electrochemical parameters are calculated from PDP curves in de-aerated anolyte and aerated catholyte with the intention of replicating the chemical conditions inside a FFC filament. Since these parameters depend on the surface of the specimens, anodizing is expected to significantly modify them. It is important to clarify that growth in  $E_{PR}$  and drops on  $E_{corr}$  and  $i_{FFC}$  values are positive for FFC resistance.

### 4.3.1 Resistance to FFC initiation ( $\Delta E_{PR}$ )

The PDP curves for (a) AAs and (b) a-AAs after 4h of OCP stabilization in  $N_2$ -deaerated anolyte are presented in **Figure 4-7**. It is observed that all the curves for a-AAs are shifted to lower current values with respect to those of corresponding AA samples; indicating anodizing can improve the overall corrosion resistance of AAs in  $N_2$ -deaerated anolytes. Focusing on the results for a-AAs in **Figure 4-7** (b), all the specimens exhibited two pitting potentials, except a-AA6061 (Mg, Si) that showed only one pitting potential. Two breakdown potentials on anodized AAs have been previously reported in the literature. The first one is attributed to the breakdown of the passive film, and the second to pitting initiation and propagation on AAs [208]. The passive range is taken as the difference between  $E_{a, corr}$  and the second and/ higher one, denoted as  $E_{pitting}$ .

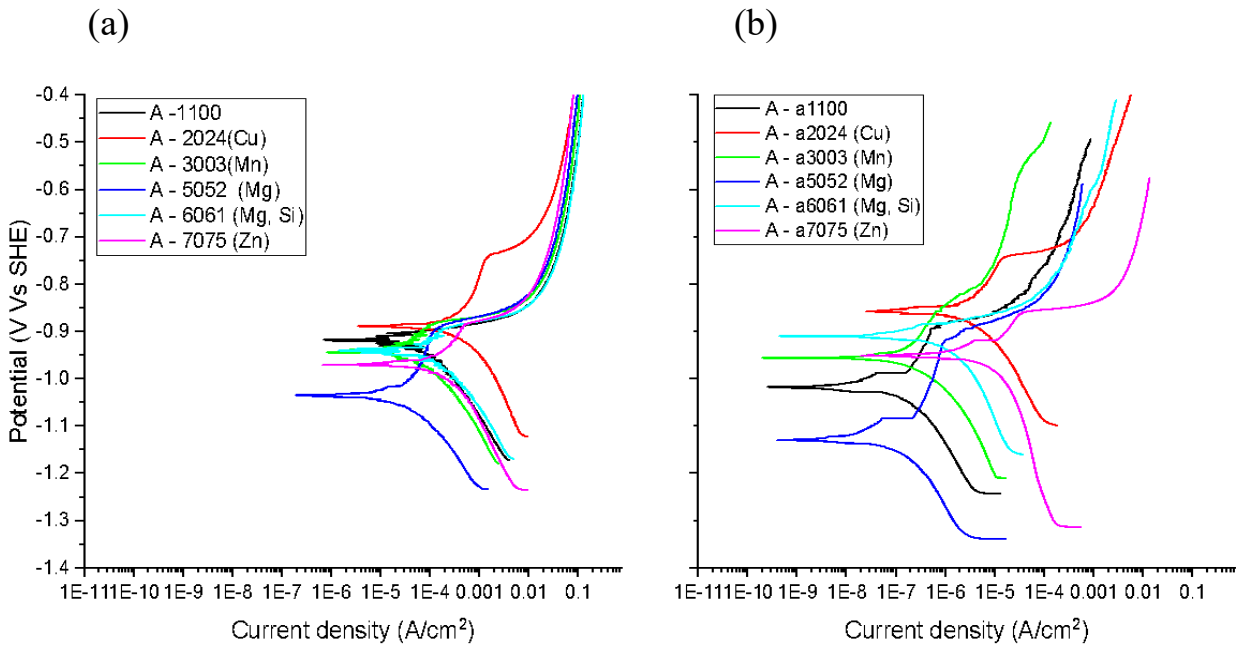


**Figure 4-7.** PDP curves of (a) AAs and (b) a-AAs in  $N_2$ -deaerated anolytes (denoted as A-).

A passive range is observed in all specimens. The values of  $E_{\text{pitting}}$ ,  $E_{a, \text{corr}}$  and  $\Delta E_{\text{PR}}$  for all six a-AA samples are shown in **Table 4-3**. With an initial approach,  $\Delta E_{\text{PR}}$  results suggest that the resistance to FFC initiation follows a tendency of 5052 (Mg) > AA1100 > 3003 (Mn) > AA 2024 (Cu) > AA7075 (Zn) > AA6061 (Mg, Si) after anodizing.

**Table 4-3.**  $E_{\text{pitting}}$ ,  $E_{a, \text{corr}}$  and  $\Delta E_{\text{PR}}$  of a-AAs from PDP curves in  $N_2$ -deaerated anolytes.

AAs	$E_{a, \text{corr}}$ (V vs. SHE)	$E_{\text{pitting}}$ (V vs. SHE)	$\Delta E_{\text{PR}}$ (V vs. SHE)
a-AA1100	-1.019 ±5E-05	-0.882 ±4E-03	0.137 ±4E-03
a-AA2024 (Cu)	-0.856 ±2E-03	-0.736 ±1E-03	0.120 ±3E-03
a-AA3003 (Mn)	-0.955 ±5E-04	-0.826 ±5E-03	0.129 ±6E-03
a-AA5052 (Mg)	-1.130 ±1E-03	-0.909 ±3E-03	0.221 ±3E-03
a-AA6061 (Mg, Si)	-0.910 ±7E-04	-0.867 ±1E-02	0.043 ±1E-02
AA7075 (Zn)	-0.953 ±1E-03	-0.856 ±1E-05	0.097 ±1E-03

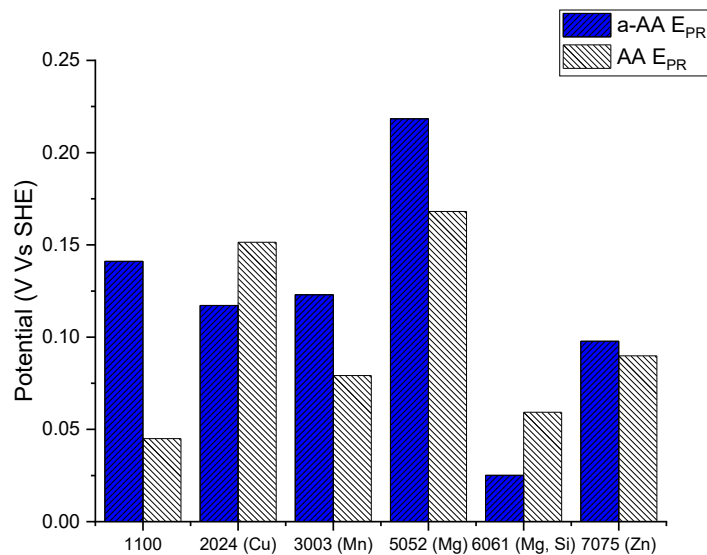


**Figure 4-8.** Estimated  $\Delta E_{PR}$  for a-AAs (blue) and AAs in  $N_2$ -deaerated anolyte.

**Figure 4-8** shows the estimated  $\Delta E_{PR}$  for a-AAs (blue) and AAs in  $N_2$ -deaerated anolytes. The  $\Delta E_{PR}$  of AAs 1100, 3003 (Mn), 5052 (Mg), and 7075 (Zn) increased 0.092 V, 0.049 V, 0.052 V and 0.007 V respectively; that is, the resistance to FFC initiation ( $\Delta E_{PR}$ ) is increased by anodizing. Conversely, for the AAs 2024 (Cu) and 6061 (Mg, Si), a decrease in  $\Delta E_{PR}$  of 0.005 V and 0.016 V were observed respectively after anodizing.

### 4.3.2 Driving force for propagation ( $\Delta E_{\text{corr}}$ )

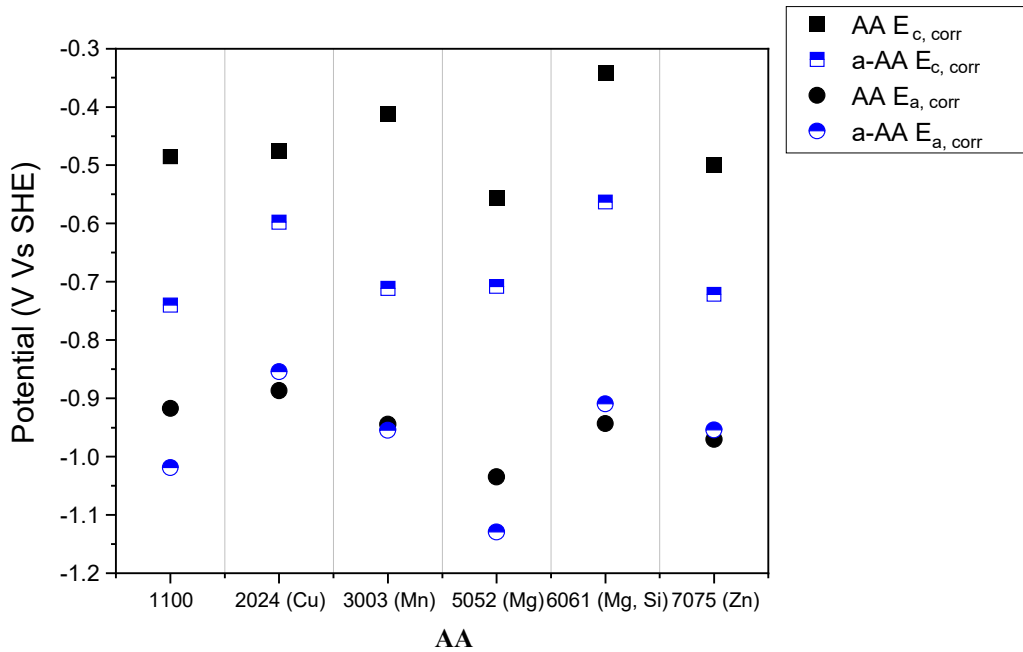


**Figure 4-9.**  $E_{\text{corr}}$  values of a-AAs (blue half symbols) in the anolyte (circle characters) and catholyte (square characters).  $E_{\text{corr}}$  values for AAs (black full symbols) are also displayed.

**Figure 4-9** illustrates the averaged  $E_{\text{corr}}$  values for a-AA samples (blue half symbols) after 4h immersion in the anolyte (circle characters) and catholyte (square characters). For comparison purposes, the  $E_{\text{corr}}$  results reported in Chapter 3, Figure 3-21 are also displayed for AA samples (black full symbols) in the same figure. Similar to AAs, the  $E_{c, \text{corr}}$  values for a-AA specimens are more positive compared to those measured in the anolyte. By comparing the  $E_{\text{corr}}$  values obtained for all specimens, a-AAs 2024 (Cu) and 6061 (Mg, Si) exhibited nobler  $E_{\text{corr}}$  in both anolyte and catholyte. Whereas the lowest  $E_{c, \text{corr}}$  and  $E_{a, \text{corr}}$  were identified to be for a-AAs 1100 and 5052 (Mg) respectively. It was observed that the anodizing pre-treatment shifted the  $E_{c, \text{corr}}$  values of all AAs to a more negative direction. This behaviour has been reported in the literature for pure Al,

AA7075 and Mg-rich AAs and in NaCl solutions [209], [210] [211]. In addition, it has been reported that the formation of  $\gamma$ -AlOOH on anodized AA2024 and 2.5 % Mg AA after the hydrothermal sealing could lower the  $E_{\text{corr}}$  in NaCl solutions [212], [213].

The  $E_{\text{corr}}$  variations are subjected to the enrichment of alloying elements on the alloy surface. For commercial AAs with multiple alloying elements, co-enrichment takes place leading to anodic films with complex compositions and numerous localized processes, depending on the oxidation and migration rate of the individual species. Enrichment of Cu and Si has been mainly observed at the oxide/metal interface [214], while Mg enrichment has been observed to occur on the anodic layer surface [215]. Elements that are prone to anodic reactions (oxidation) tend to be oxidized during the anodizing process and enriched at the surface, while elements that promote cathodic reactions are enriched in the interface matrix/oxide. The composition of anodic films on different types of AAs as mentioned above together with the mixed potential theory can be used to explain the negative shift in the potential in the catholyte [204], [216]. On the other hand,  $E_{\text{a, corr}}$  values did not exhibit much variation with the anodizing process; this is not particularly surprising given the fact that the anodic layer has been reported not to be stable under strong acid or alkaline conditions.

**Table 4-4** presents the averaged  $\Delta E_{\text{corr}}$  ( $=E_{\text{c, corr}} - E_{\text{a, corr}}$ ) values of the evaluated a-AAs at room temperature. The driving force for FFC propagation, i.e.,  $\Delta E_{\text{corr}}$ , follows the trend a-AA 6061 (Mg, Si) > 3003 (Mn) > 5052 (Mg), 7075 (Zn) > 2024 (Cu), 1100. **Figure 4-10** compares the  $\Delta E_{\text{corr}}$  values for a-AA (blue) and AA (black) samples.  $\Delta E_{\text{corr}}$  is consistently lower for all a-AAs compared with the corresponding AAs. As anticipated, anodizing decreases the tendency to filament propagation

for all the studied AAs. Additionally, it is observed that AA 5052 (Mg) exhibited the smallest reduction in  $\Delta E_{\text{corr}}$  probably adjudicated to the similarity between the natural oxide film formed and the anodic film obtained on AA 5052. The  $\Delta E_{\text{corr}}$  drop in all a-AA specimens can be attributed to two parts: the slower kinetics of  $\text{O}_2$  reduction on the a-AAs in the catholyte, and the higher corrosion resistance of a-AAs in the anolyte.

**Table 4-4.** Averaged  $E_{\text{c, corr}}$  and  $\Delta E_{\text{corr}}$  values of the evaluated a-AAs at room temperature.

AAs	$E_{\text{c, corr}}$ (V vs. SHE)	$\Delta E_{\text{corr}}$ (V vs. SHE)
a-AA1100	-0.740 ±5.0E-03	0.432 ±2.5E-03
a-AA2024 (Cu)	-0.597 ±1.5E-03	0.412 ±7.5E-04
a-AA3003 (Mn)	-0.711 ±9.5E-03	0.532 ±4.7E-03
a-AA5052 (Mg)	-0.707 ±3.5E-03	0.478 ±1.7E-03
a-AA6061 (Mg, Si)	-0.563 ±1.7E-02	0.602 ±8.2E-03
AA7075 (Zn)	-0.721 ±5.5E-03	0.471 ±2.7E-03

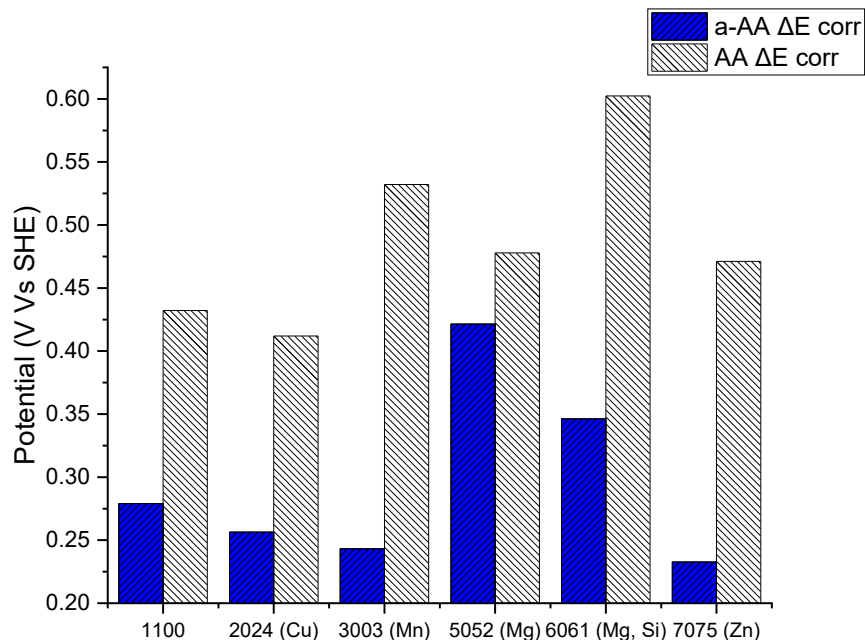


**Figure 4-10.**  $\Delta E_{corr}$  values of a-AAs (blue) and AAs calculated as  $E_{c, corr} - E_{a, corr}$  from PDP measurements in simulated anolytes and catholytes.

### 4.3.3 Kinetics of propagation ( $i_{FFC}$ )

**Figure 4-11** shows PDP curves for AA (black) and a-AA (blue) collected in aerated catholytes and deaerated anolytes. The PDP curves for AA samples are shown here only for comparative purposes. It was evident that all curves for AAs were drastically shifted to lower current values in both anolyte and catholyte, leading to a decrease in the kinetics of Al dissolution in both electrolytes. These observations are consistent with the fact that anodic films can protect the AAs substrate by hindering penetration of corrosive media toward the base AAs [217].

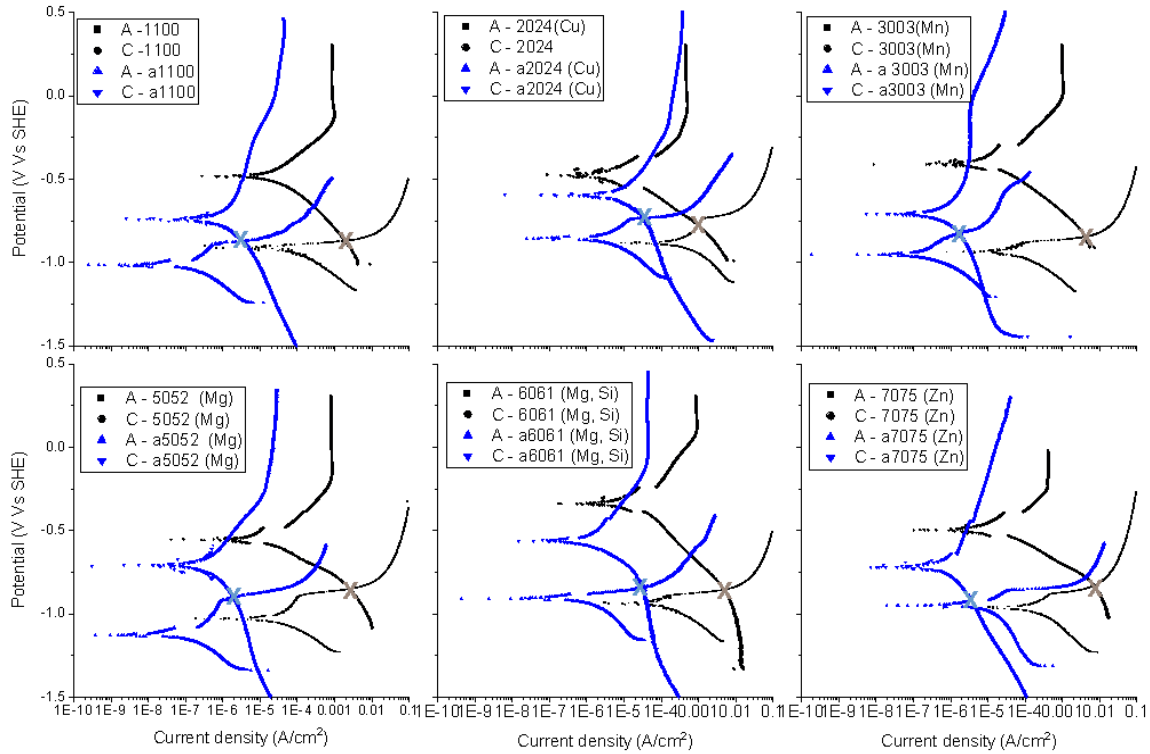


**Figure 4-11.** Polarization curves of AA (black) and a-AA (blue) samples were obtained in  $N_2$ -deaerated anolytes (denoted as A-), and in aerated catholytes (denoted as C-) at 25 °C. FFC current density ( $i_{\text{FFC}}$ ,  $A/cm^2$ ) is taken as the intercept of the anodic and cathodic curves assuming an effective cathode/anode area ratio of 100.

**Table 4-5** lists the  $i_{\text{FFC}}$  values for a-AAAs. It is observed that  $i_{\text{FFC}}$  ( $mA/cm^2$ ) follows the trend 6061 (Mg, Si), 2024 (Cu) > 7075 (Zn) > 1100 > 3003 (Mn), 5052 (Mg). Therefore, longer filaments are expected to take place in anodized 6061 (Mg, Si) and 2024 (Cu). As it was observed in chapter 3 for AA samples, the a-AA that exhibited the higher kinetics to FFC propagation also exhibited the nobler potential in the catholyte. In a word, electrochemical results suggest the dominant influence of the cathodic reactions in the catholyte on the propagation speed of FFC filaments.

**Table 4-5.**  $i_{\text{FFC}}$  of a-AAs from PDP curves in  $\text{N}_2$ -deaerated anolyte.

AAs	$i_{\text{FFC}}$ ( $\text{A}/\text{cm}^2$ )
a-AA1100	$3.258\text{E-}6 \pm 3.8\text{E-}07$
a-AA2024 (Cu)	$2.961\text{E-}5 \pm 4.2\text{E-}06$
a-AA3003 (Mn)	$1.565\text{E-}6 \pm 8.5\text{E-}08$
a-AA5052 (Mg)	$1.780\text{E-}6 \pm 1.6\text{E-}07$
a-AA6061 (Mg, Si)	$3.048\text{E-}5 \pm 1.7\text{E-}06$
AA7075 (Zn)	$3.617\text{E-}6 \pm 3.1\text{E-}07$

**Figure 4-12** compares the  $i_{\text{FFC}}$  values for a-AA (blue) and AA (black) samples. It is observed that anodizing significantly decreased the kinetics of FFC in all AA samples. The  $i_{\text{FFC}}$  exhibited by a-AAs 1100, 3003 (Mn), 5052 (Mg) and 7075 (Zn) was three orders of magnitude lower than the bare metal. Moreover, the  $i_{\text{FFC}}$  values calculated for a-AAs 2024 (Cu) and 6061 (Mg, Si) were 2 orders of magnitude smaller than those of the bare sample. Another observation emerging from the data comparison is that anodizing had a lower efficiency on AA 2024 (Cu); this is the same for the other two parameters. A reasonable explanation was reported to be that Cu could significantly lower the barrier properties of the anodic layer, which could cause a disordered structure and hinder the sealing process [218].

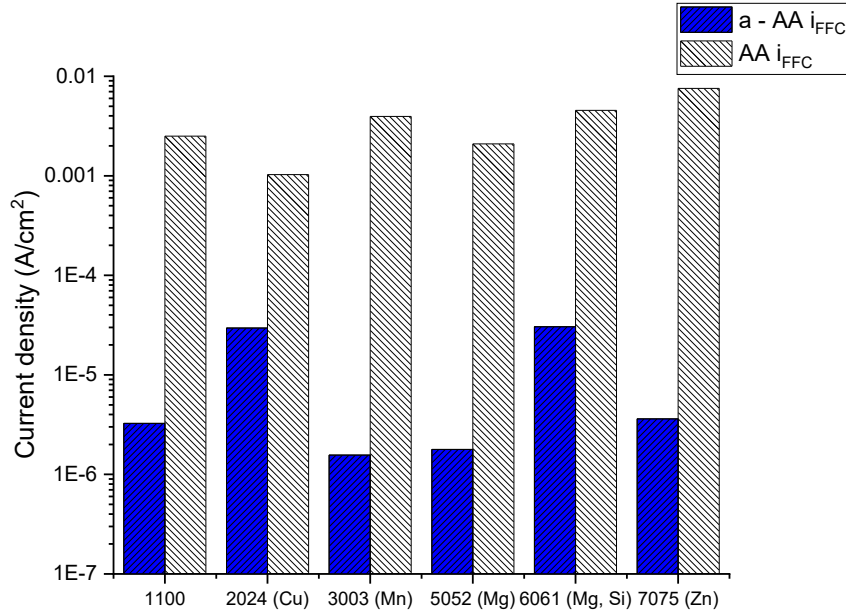


**Figure 4-12.**  $i_{corr}$  values for a-AA (blue) and AA (black) samples calculated as the intercept of the anodic and cathodic PDP curves.

#### 4.3.4 Electrochemical measurements summary

In summary, pre-treating AAs with anodizing can effectively lower the susceptibility of AAs to FFC. The improved FFC resistance can be attributed to the obtained anodic films on AA surface. Additionally, the electrochemical results emphasize that the three FFC parameters,  $\Delta E_{PR}$ ,  $\Delta E_{corr}$  and  $i_{FFC}$ , are influenced by the quality and composition of the obtained anodic film. Specific conclusions are summarized below and also in Figure 4-13.

- The resistance to FFC initiation ( $\Delta E_{PR}$ ) depends on the stability and properties of the anodic film, i.e., the surface status. FFC initiation resistance on a-AAs follows a tendency of 5052 (Mg) > AA1100 > 3003 (Mn) > AA 2024 (Cu) > AA7075 (Zn) > AA6061 (Mg, Si). Anodizing can effectively increase the resistance to FFC initiation for AAs 1100, 3003 (Mn), 5052 (Mg) and

7075 (Zn) by a factor of 3.13, 1.55, 1.29 and 1.08 respectively. However, anodizing adversely affects the FFC initiation on AAs 2024 (Cu) and 6061 (Mg, Si) by decreasing the  $\Delta E_{PR}$  values by a factor of 0.77 and 0.42 respectively.

- FFC tendency to propagation of a-AA follows a tendency of 6061 (Mg, Si) > 3003 (Mn) > 5052 (Mg), 7075 (Zn) > 2024 (Cu), 1100. The tendency to FFC propagation was reduced in all specimens by the anodizing process.  $\Delta E_{corr}$  values were reduced by a factor of 1.56, 1.61, 2.22, 1.14, 1.75 and 2.04 for AAs 1100, 2024 (Cu), 3003 (Mn), 5052 (Mg), 6061 (Mg, Si) and 7075 (Zn) respectively.
- Finally, the kinetics of propagation ( $i_{FFC}$ ) is mainly controlled by the reduction of oxygen in the local cathode. FFC propagation kinetics for a-AA samples follows a tendency of 6061 (Mg, Si), 2024 (Cu) > 7075 (Zn) > 1100 > 3003 (Mn), 5052 (Mg). Longer filaments are expected in a-AAs 6061 (Mg, Si) and 2024 (Cu). In addition, anodizing resulted in a drastic reduction of  $i_{FFC}$  values for all the samples.  $i_{FFC}$  was reduced by a factor of 767.3, 34.7, 2523.9, 1174.15, 148.9 and 2087.3 for AAs 1100, 2024 (Cu), 3003 (Mn), 5052 (Mg), 6061 (Mg, Si) and 7075 (Zn) respectively. The anodic film act as a barrier layer that slows down the transfer of electrons by reducing the rate of the anodic and cathodic reactions.

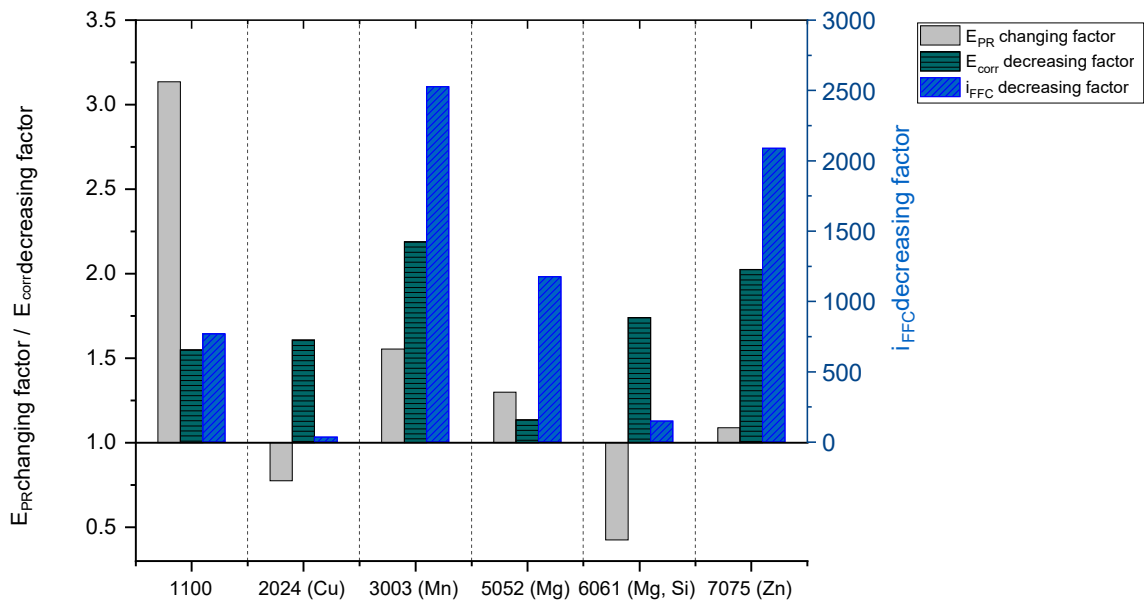


**Figure 4-13.** Graph of  $E_{PR}$  changing factors and  $E_{corr}$  and  $i_{FFC}$  decreasing factors for AAs after anodizing.

## 4.4 ACCELERATED EXPOSURE TEST

### 4.4.1 General observations

A clear epoxy film about  $10.26 \pm 2.6 \mu\text{m}$  thick was obtained on all the samples. FFC filaments were successfully replicated after 1000 h exposure to 80 % RH at 40 °C on AA and a-AA samples. In some AA 3003 (Mn) specimens a few filaments were observed to appear from defects on the coating far from the scribe. Only filaments that emerged from the scribe were taken into account for the analysis. For all samples, no blistering was observed on the areas where no FFC attack was observed. **Figure 4-14** displays pictures showing the development of FFC on AA 3003 (Mn) bare and anodized as a function of time up to 6 weeks (i.e., 1000 h) of exposure. Overall, it was observed that 1) FFC started at individual sites along the scribe; 2) the length of filaments increased with time and FFC was significantly less severe on a-AAs compared with AAs. All the AAs and a-AAs followed the same observation. That is, as predicted from the electrochemical measurements, a drastic decrease in FFC susceptibility was observed on all a-AA samples.

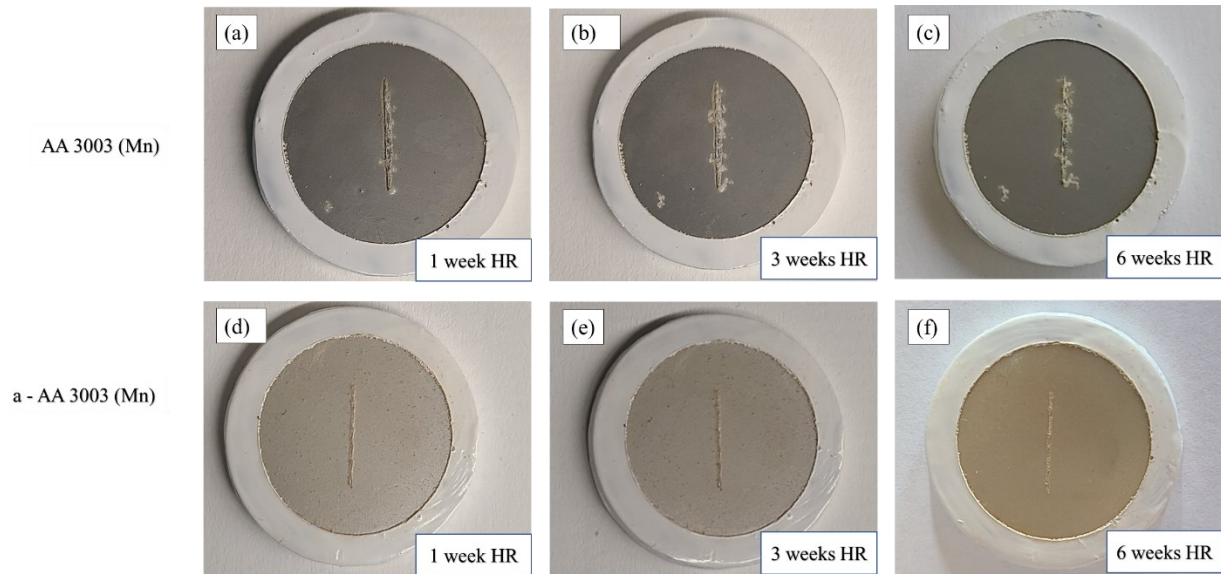


**Figure 4-14.** Development of FFC from a scribe on AA 3003(Mn) (a)(b)(c) and a-AA 3003(Mn) (e)(f)(g) after 1 week, 3 weeks and 6weeks of accelerated exposure testing.

In order to observe the morphology of developed filaments, **Figure 4-15** shows OM images of an isolated FFC filament on AA 2024 (Cu) before (a) and after (b) removing the epoxy coating and corrosion products. All filaments observed on all samples presented a similar shape and morphology. The filaments shape consisted of two regions: head and tail (**Figure 4-15 (a)**), as described and expected in Chapter 2 Section 2.3.

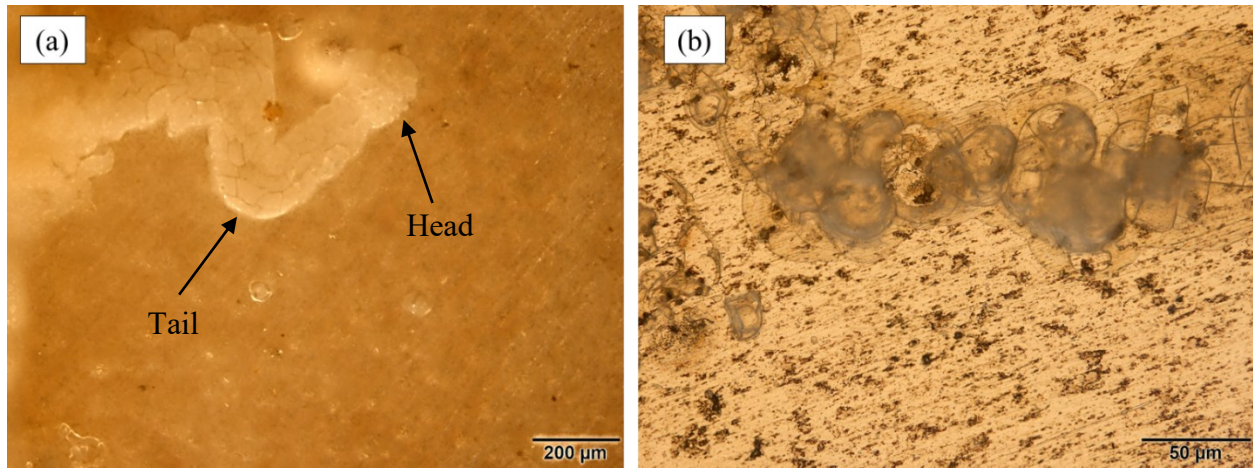


**Figure 4-15.** OM images of an isolated FFC filament after 1000 h accelerated exposure to 80 % RH at 40 °C before (a) and after (b) removing the epoxy coating and corrosion products were washed on AA 2024 (Cu) samples.

The filament head was revealed as a circular region followed by a tail filled with crackle corrosion products that can be observed through the transparent coating. According to the literature the corrosion product, mainly  $\text{Al}(\text{OH})_3$ , left behind in the FFC tail region would slowly get dehydrated and be converted to porous hydrated Al (III) oxide ( $\text{Al}_2\text{O}_3 \cdot x\text{H}_2\text{O}$ ) [163]. The width of the filaments tail is also observed to decrease as it gets closer to the head. This can be explained by the swelling of corrosion products. Those features have also been reported in previous studies [62]. The removal of the epoxy coating revealed the FFC attack on the AA surface (**Figure 4-15 (b)**). FFC was seen to advance leaving successive dark rings. This observation has been reported by several authors on Al and steel [219]. There has been disagreement concerning the development of these circles, but some authors have described them as a result of through-coating cathodic  $\text{O}_2$  reduction acting to increase local pH at the perimeter of the filament-head [163], [219]. The presence of these dark rings also suggests that the filament head advances in a saltatory way through successive

local anodic dissolution [220]. The FFC behaviour of these specimens was assessed mainly by comparison via visual examination with naked eyes and images taken by an OM. Two parameters were defined, the number of threads per cm (N) and the length of the filaments (L). In the following paragraphs, these parameters will be evaluated in AA samples (section 4.4.2) and a-AA samples (section 4.4.3).

#### **4.4.2 Results for AAs**

**Figure 4-16** presents pictures of the scribe area of epoxy coated AAs 1100, 2024 (Cu), 3003 (Mn), 5052 (Mg), 6061 (Mg, Si) and 7075 (Zn) after 1000 h accelerated exposure to 80 % RH at 40 °C. It was observed that AA 6061(Mg, Si) exhibited the most severe disbanding of the organic coating around the scribe while AA 5052 (Mg) samples were not susceptible to FFC under the same conditions evaluated, as no observable filament emerged from the scribe or any other area on the AA5052 (Mg) surface. In this case, it is believed that alloying element Mg can improve FFC resistance principally through the anodic dissolution of Mg and further reacting with  $\text{OH}^-$  to form  $(\text{Mg}(\text{OH})_2)$  at the cathode sites [221].

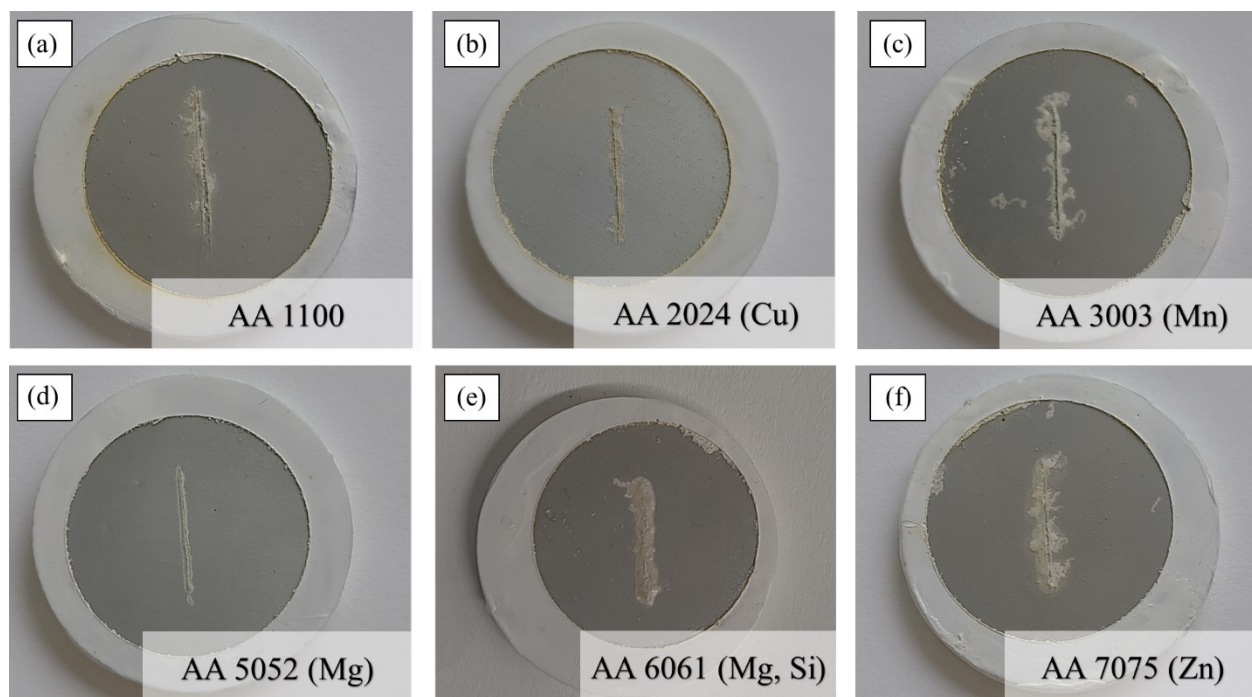


**Figure 4-16.** Images of epoxy coated AAs 1100, 2024 (Cu), 3003(Mn), 5052 (Mg), 6061 (Mg, Si) and 7075 (Zn) with scribes after 1000 h accelerated exposure to 80 % RH at 40 °C.

#### 4.4.2.1 Number of filaments (N)

Results for the number of filaments (N) observed for all AA samples are listed in **Table 19**. There was a significant derivation on the averaged N values among the different AAs. The greatest N (17 filaments/cm) was exhibited by AA 3003 (Mn). On the other hand, the lower N (besides the N=0 for AA 5052 (Mg)) was observed on AA1100 (6 filaments/cm). The N value followed the trend 3003 (Mn) > 6061 (Mg, Si) > 2024 (Cu) > 1100 > 5052 (Mg).

**Table 4-6** also compares the tendency to FFC initiation and propagation obtained from the calculated  $\Delta E_{PR}$  and  $\Delta E_{corr}$  in electrochemical measurements. The values were categorized as *high* or *low* according to  $\Delta E_{PR}$  and  $\Delta E_{corr}$  values with respect to the other AAs. That is, the highest

values of  $\Delta E_{\text{corr}}$  are rated as a *high* tendency to propagation while the lowest values are rated as a *low* tendency to propagation. The correlation between the electrochemical parameters of FFC and N is worth noting. Even though N did not follow the same trend as the electrochemical parameters  $\Delta E_{\text{PR}}$  and  $\Delta E_{\text{corr}}$ , the alloys with a high tendency to FFC initiation and propagation exhibited the greatest values of N.

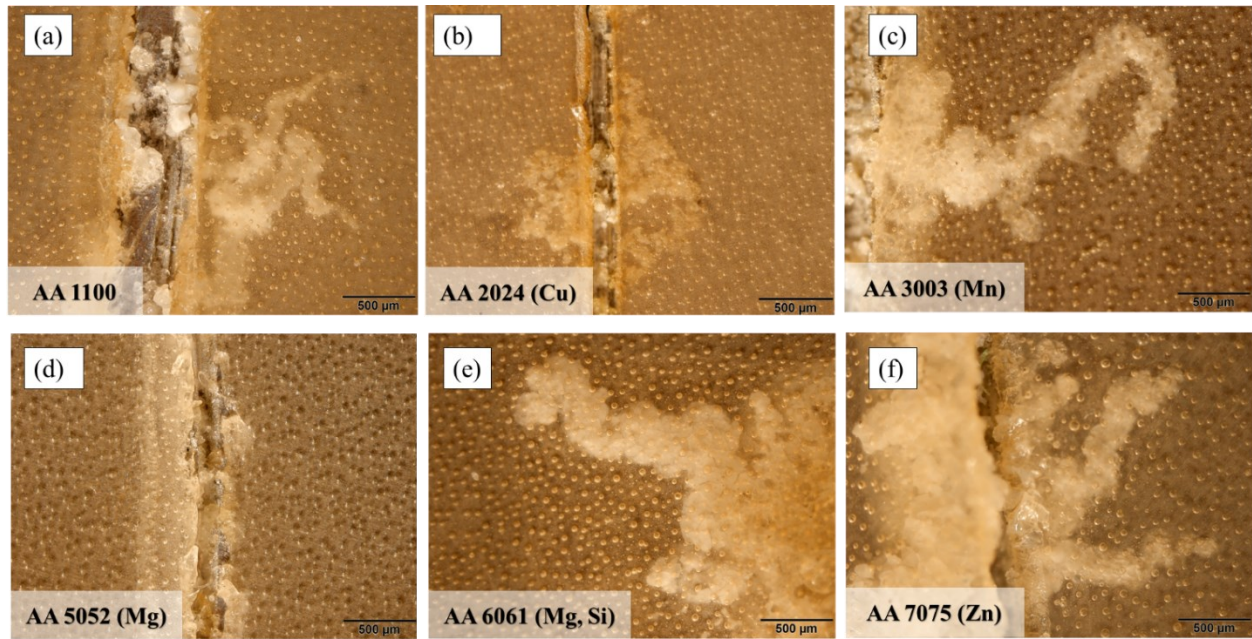
**Table 4-6.** Averaged N values of AAs after 1000h accelerated exposure testing (80 % RH, 40 °C).

AA	N (# of filaments/cm)	Tendency to FFC initiation and propagation from EC tests	
		$\Delta E_{\text{PR}}$	$\Delta E_{\text{corr}}$
1100	6 ±1	-	Low
2024 (Cu)	10.5 ±4.5	Low	Low
3003 (Mn)	17 ±2	High	High
5052 (Mg)	0 -	Low	Low
6061 (Mg, Si)	15.5 ±8.5	High	High
7075 (Zn)	14.5 ±5.5	Low	High

*Note: The values are compared with the tendency to FFC initiation and propagation obtained from electrochemical tests. The cell  $\Delta E_{\text{PR}}$  was left blank for 1100 as there was no  $\Delta E_{\text{PR}}$  for that sample.*

#### 4.4.2.2 Length of filaments (L)

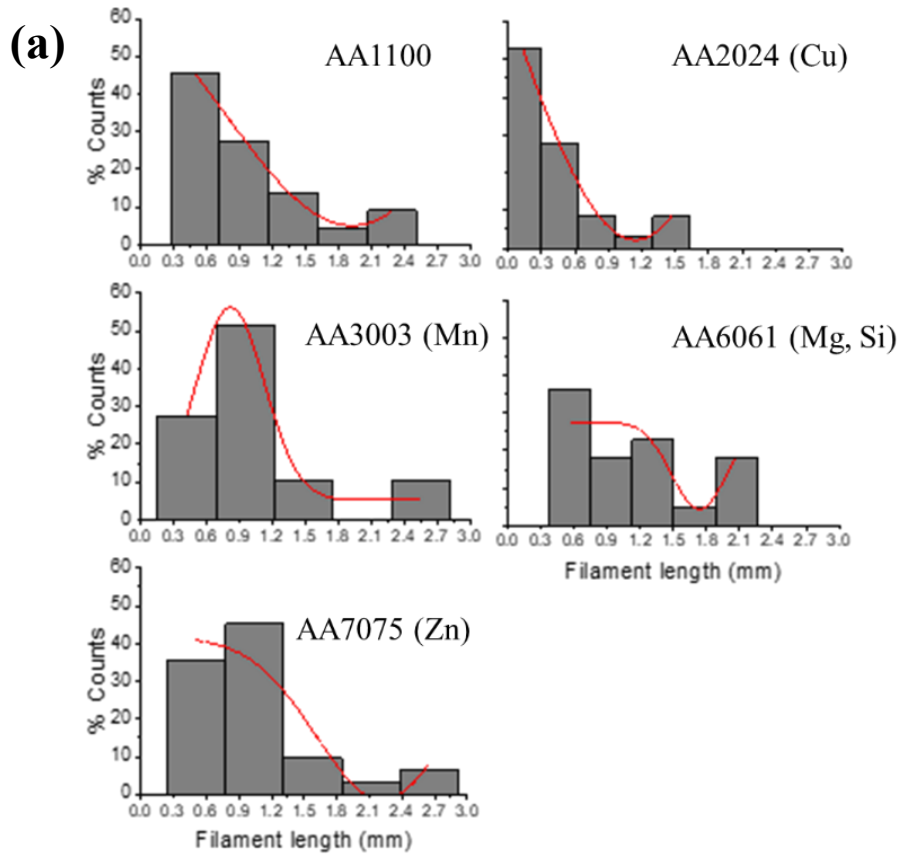
**Figure 4-17** presents OM images on the scribe areas of epoxy coated AAs (a) 1100, (b) 2024 (Cu), (c) 3003 (Mn), (d) 5052 (Mg), (e) 6061 (Mg, Si) and (f) 7075 (Zn) after 1000h accelerated exposure to 80% RH at 40°C. The scribe area was magnified to distinguish the individual filaments in greater detail.



**Figure 4-17.** OM images on the scribe area of epoxy coated AAs (a) 1100, (b) 2024 (Cu), (c) 3003 (Mn), (d) 5052 (Mg), (e) 6061 (Mg, Si) and (f) 7075 (Zn) after 1000h accelerated exposure to 80 % RH at 40 °C.

It is evident that FFC filaments initiate perpendicular to the scribe and change direction after the growth of a few microns. Filament length ( $L$ ) from the scribe was measured on AA samples considering the propagation path and deviations. A significant variation in the  $L$  values was also observed among different AAs. The averaged  $L$  calculated was 1.14, 0.56, 1.31, 1.34 and 1.33 mm for AAs 1100, 2024 (Cu), 3003 (Mn), 6061 (Mg, Si) and 7075 (Zn) respectively. The maximum  $L$  was found on an AA 7075 (Zn) sample with a length of 2.931 mm. **Figure 4-18** (a) shows the  $L$  distribution on each sample. The averaged  $L$  on AA samples followed the trend 7075 (Zn) > 6061 (Mg, Si) > 3003 (Mn) > 5052 (Mg) > 1100 > 2024 (Cu). This trend is the same as that observed trend for  $i_{FFC}$  on AA samples.

**Figure 4-18** (b) presents the relation between the calculated  $i_{FCC}$  from the electrochemical measurements and the measured  $L$  from the accelerated exposure testing. There is a remarkable correlation between these two parameters. The plotted data showed that  $i_{FCC}$  increases with increasing  $L$  values. The linearity of the tendency is not maintained for AAs with higher  $L$  values which can be attributed to the well-reported decrease in growth rate as the filaments advance. The slowed kinetics was due to the limited diffusion of  $O_2$  through the long tail of corrosion products and depletion of  $Cl^-$  concentration in the filament head [64].



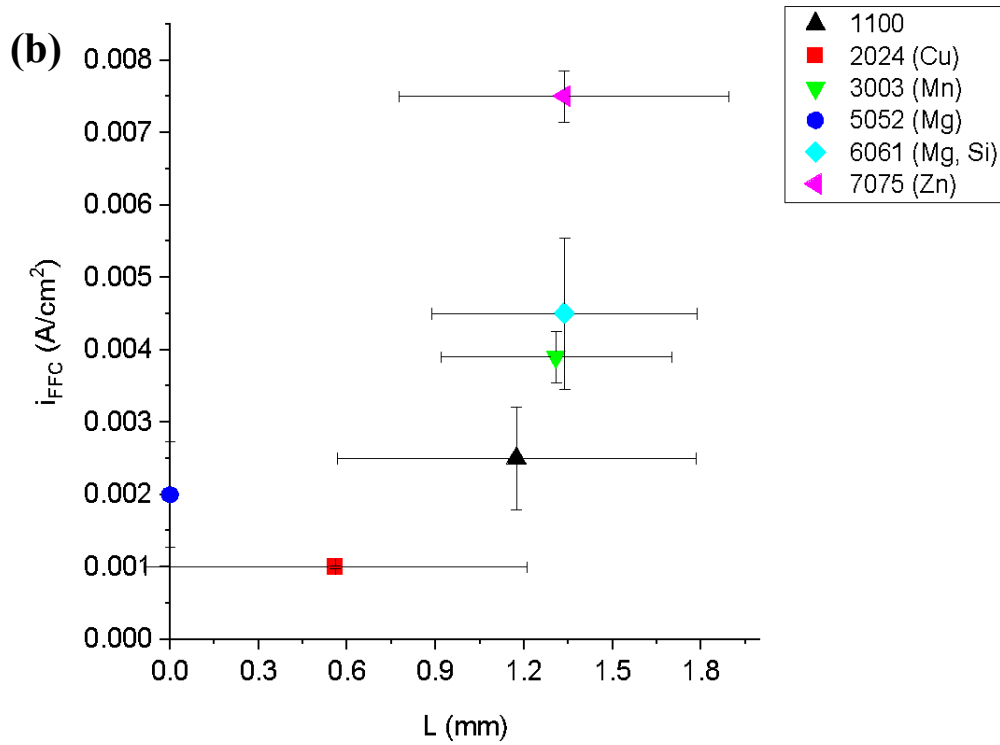


**Figure 4-18.** (a) Filament length ( $L$ ) distribution on AAs, and (b) the relation between the  $i_{FFC}$  and  $L$ .

#### 4.4.3 Results for a-AAs

**Figure 4-19** shows images of the scribe area of epoxy coated a-AAs 1100, 2024 (Cu), 3003 (Mn), 5052 (Mg), 6061 (Mg, Si) and 7075 (Zn) after 1000 h accelerated exposure to 80 % RH at 40 °C. Similar to the bare samples, a-AA 5052 (Mg) specimens were not susceptible to FFC under the same conditions evaluated. Overall, a substantial increase in FFC resistance of AAs with the anodizing pre-treatment is observed with a clear reduction in the number and length of filaments on all samples.

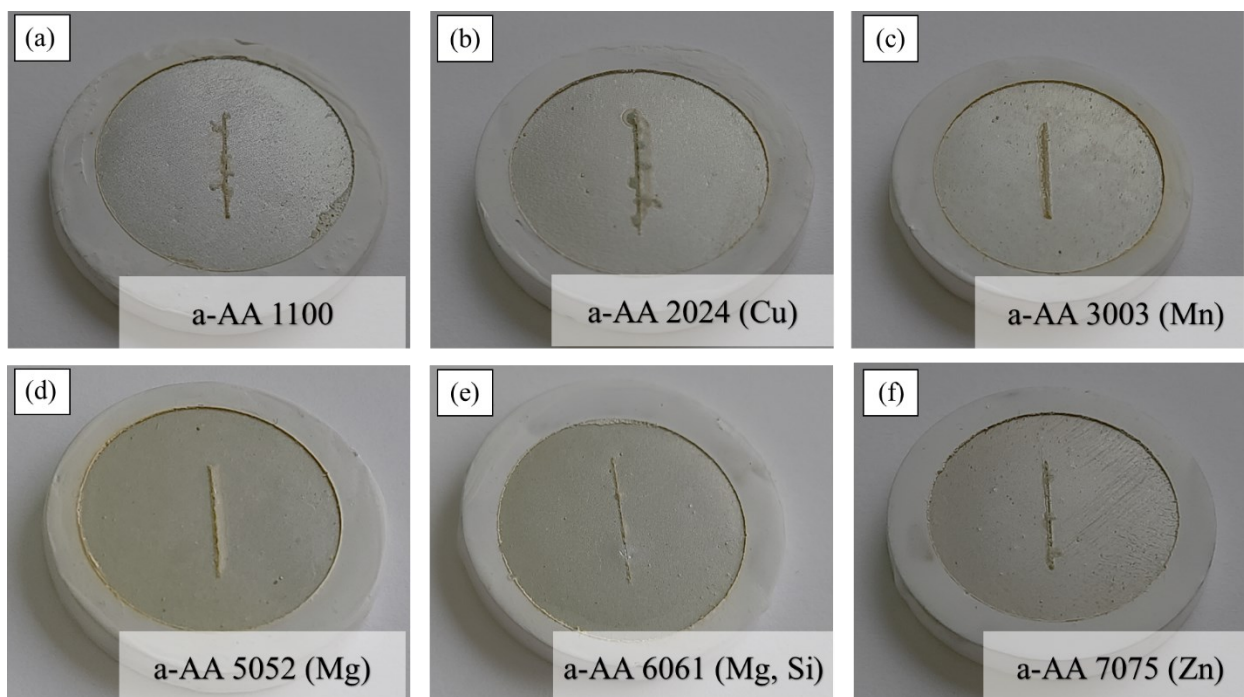


**Figure 4-19.** Images of epoxy coated a-AAs 1100, 2024 (Cu), 3003(Mn), 5052 (Mg), 6061 (Mg, Si) and 7075 (Zn) with scribes after 1000 h accelerated exposure to 80 % RH at 40 °C.

#### 4.4.3.1 Number of filaments (N)

The averaged N values obtained for a-AAs are summarized in **Table 4-7**. The highest N (4 filaments/cm) was exhibited for a-AAs 1100 and 2024 (Cu). N followed the trend 2024 (Cu), 1100 > 7075 (Zn) > 3003 (Mn), 6061 (Mg, Si) > 5052 (Mg). Additionally, **Table 4-7** compares the tendency to FFC initiation and propagation from the calculated  $\Delta E_{PR}$  and  $\Delta E_{CORR}$  in electrochemical measurements. There was no correlation found between the number of filaments (N) that emerged from the scribe and the tendency to initiation and propagation although the N values were significantly decreased on the a-AAs.

**Table 4-7.** Averaged N values of a-AAs after 1000h accelerated exposure testing (80 % RH, 40 °C).

a-AA	N (# of filaments/cm)	Tendency to FFC initiation and propagation from EC tests	
		$\Delta E_{PR}$	$\Delta E_{corr}$
1100	4 ±2	Low	Low
2024 (Cu)	4 ±3	High	Low
3003 (Mn)	1 ±1	Low	High
5052 (Mg)	0 ±0	Low	High
6061 (Mg, Si)	1 ±0	High	High
7075 (Zn)	2 ±1	High	High

#### 4.4.3.2 Length of filaments (L)

The calculated averaged L was 0.61, 0.65, 0.41, 0.45, 0.56 mm for a-AAs 1100, 2024 (Cu), 3003 (Mn), 6061 (Mg, Si) and 7075 (Zn) respectively. The L value followed the trend of 2024 (Cu) > 1100 > 7075 (Mn) > 6061 (Mg, Si) > 3003 (Mn). **Figure 4-20** presents the relation between the calculated  $i_{FFC}$  from the electrochemical measurements and the measured L from the accelerated exposure test. Even though the accelerated exposure testing also proved that pre-anodizing could effectively lower the susceptibility of AAs to FFC, no correlation was found between parameters L and  $i_{FFC}$ . This lack of correlation can be attributed to the fact that anodizing not only changes the electrochemistry response of AA surface but also affects the adhesion of the coating [222], [223]. The differences in the morphology and composition of anodic films from one alloy to another could also change the interaction between anodized surfaces with coating. In addition, due to the varying compositions and properties of anodic films on different AAs, the mechanisms of FFC on anodized AAs will be different and more complex than on the metal substrates.

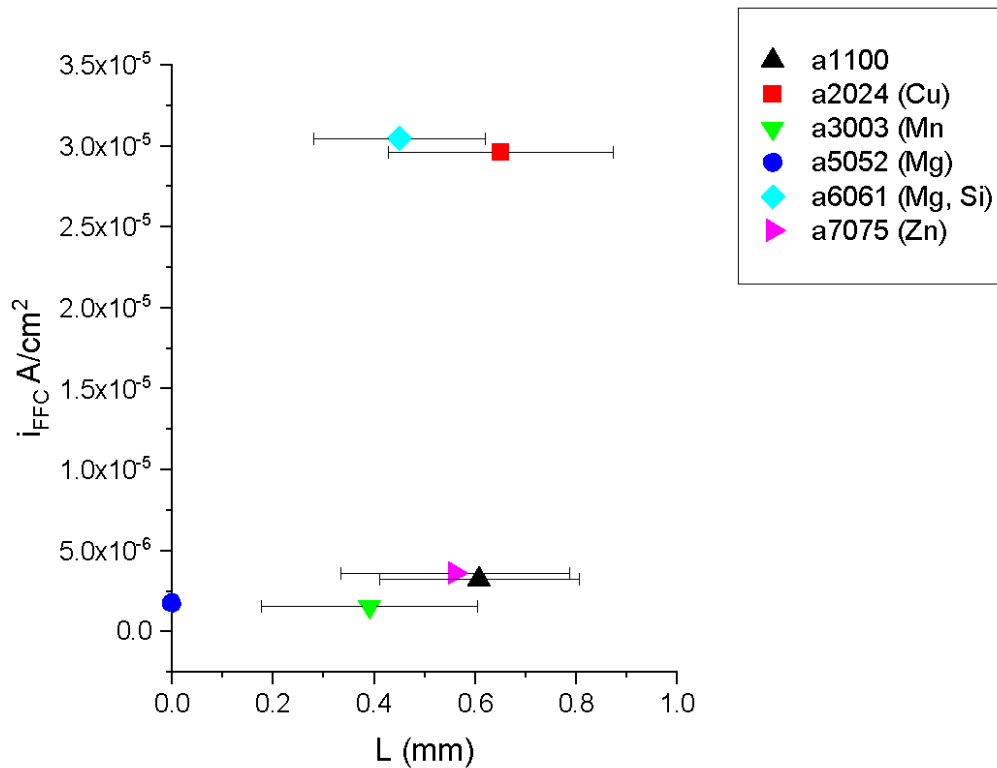


**Figure 4-20.** Relation between the  $i_{corr}$  and L for a-AA samples.

#### 4.4.4 Accelerated exposure testing summary

**Figure 4-21** summarizes N and L values calculated for AA and a-AA samples after 1000 h of accelerated exposure test (80 % RH, 40 °C) Specific conclusions are summarized as below:

- There was a dramatic reduction of FFC severity on AAs after the anodizing pre-treatment. The bare AAs exhibited a maximum N and L of 17 filaments/cm and 1.34 mm respectively, while the anodized ones showed a maximum N and L of 4 filaments/cm and 0.65 mm respectively.

- A clear correlation between FFC electrochemical parameters ( $\Delta E_{PR}$ ,  $\Delta E_{CORR}$  and  $i_{FFC}$ ) and those calculated from the accelerated exposure test (N and L) was observed for the bare AA samples. Even though the accelerated exposure testing also proved that pre-anodizing could effectively lower the susceptibility of AAs to FFC, no correlation between the group of N and L data vs. the group of EC data was found for the anodized specimens.
- It is observed from **Figure 4-21** that anodizing had the greatest effect on improving FFC resistance on AA 3003 (Mn) while the lowest improvement was observed on AA 2024 (Cu); this behaviour was predicted from the electrochemical measurements and illustrated in **Figure 4-13**. In addition, AA and a-AA5052 exhibited the highest resistance to FFC as filaments were not observed on these samples after 1000 h of accelerated exposure test (80 % RH, 40 °C). These results are in agreement with the EC measurements in which AA and a-AA5052 showed the highest resistance to FFC initiation (Larger  $\Delta E_{PR}$  values).

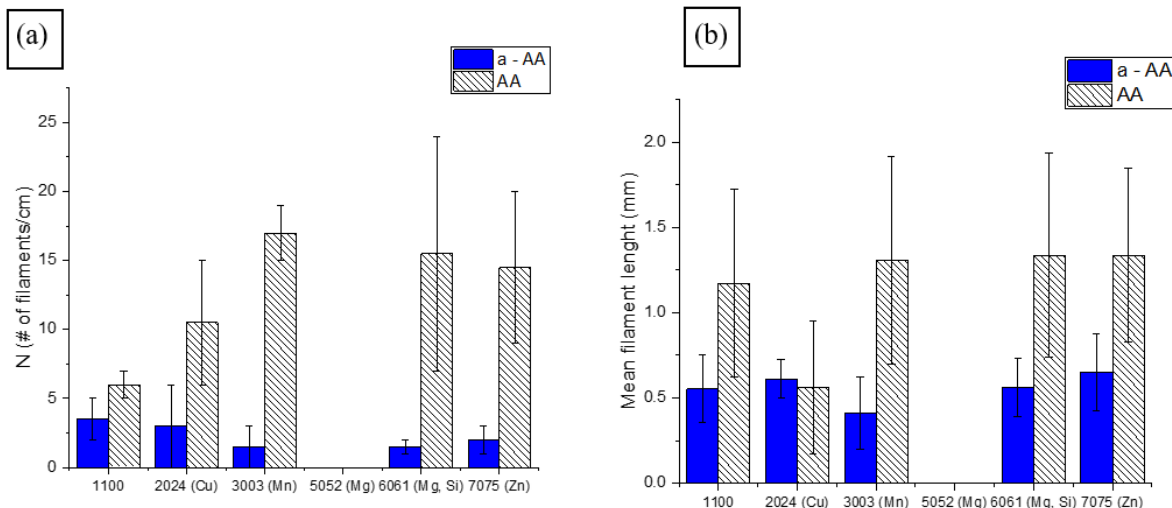


**Figure 4-21.** Summary of N (a) and L (b) values for AA and a-AA samples.

# CHAPTER 5 CONCLUSIONS AND FUTURE

## WORK

In this work, we investigated the FFC of various AAs via electrochemical measurements and long-term humidity testing. Specifically, we focused on the influence of alloying elements and anodizing as a pre-coating treatment on the FFC susceptibility of AAs in order to broaden current knowledge on the FFC of painted AAs. Some highlights and remaining challenges for future work are summarized and revealed.

### 5.1 Conclusions

- To describe the FFC behaviour of Al alloys, electrochemical measurements were successfully performed on AA substrates in bulk anolyte and catholyte solutions at room temperature. Three factors were defined, including the resistance to FFC initiation ( $\Delta E_{PR}$ , V), the driving force for propagation ( $\Delta E_{corr}$ , V), and the FFC kinetics of propagation ( $i_{FFC}$ , mA/cm<sup>2</sup>).  $\Delta E_{PR}$  results suggest that the resistance to FFC initiation follows a tendency of AA 2024 (Cu) > 5052 (Mg) > AA7075 (Zn) > 3003 (Mn) > AA6061 (Mg, Si) > AA1100; the driving force for FFC propagation ( $\Delta E_{corr}$ ) followed the trend AA 6061 (Mg, Si) > 7075 (Zn), 3003 (Mn) > 5052 (Mg) > 2024 (Cu), 1100; and FFC kinetics of propagation ( $i_{FFC}$ ) followed the trend 7075 (Zn) > 6061 (Mg, Si) > 3003 (Mn) > 5052 (Mg) > 1100 > 2024 (Cu). We have obtained accurate results showing that the application of these parameters offers a clear understanding of the FFC mechanisms on AAs and can be used to effectively predict their susceptibility to FFC. Accelerating exposure testing confirmed the effectiveness of adopting these parameters.

A clear correlation between FFC electrochemical parameters ( $\Delta E_{PR}$ ,  $\Delta E_{corr}$  and  $i_{FFC}$ ) and those calculated from the accelerated exposure test (N and L) was observed for the bare AA samples.

- The derivation in FFC susceptibility on various AAs suggested that alloying elements, and more specifically, the presence of IMPs and matrix composition, play a significant role in the FFC susceptibility of AAs. EC data and SEM with EDS support extensive previous work in which localized corrosion is strongly influenced by the heterogeneity of the alloy. For example, IMPs that are more cathodic compared to the matrix can promote pitting corrosion and cathodic reactions in the catholyte, thus enhancing FFC initiation and kinetics of propagation; alloying elements can affect the corrosion potential ( $E_{corr}$ ) of AAs layer in the anolyte and catholyte, and thus influence the driving force for propagation.
- Both EC and accelerated exposure testing proved that pre-anodizing could effectively lower the susceptibility of AAs to FFC, resulting in a strong decrease in FFC kinetics and delaying FFC during 1000h of exposition.

## 5.2 Future Work

Even though both EC and accelerated exposure tests proved that pre-anodizing could effectively lower the susceptibility of AAs to FFC, no correlation between the group of N and L data vs. the group of EC data was found for the anodized specimens. Potential reasons and limitations are:

- Electrochemical measurements did not consider metal/coating interaction.

- The electrical insulating properties of the anodic layers brought some uncertainties to the electrochemical measurements.
- The anodized samples were subjected to several processes (electropolishing, anodizing and sealing) in sequence. Each process, induced surface changes and brought more uncertainties for the following experiments.
- Data on the thickness and nanostructure of the anodic layer was not collected. They may be useful to explain the observed trends further.

In addition, another pre-anodizing method(s) may be more suitable for evaluating the susceptibility of anodized AAs to FFC. Future work is suggested to identify the optimal parameters of anodizing procedures, and to carry out the characterization of anodic films more in-depth in order to obtain comparable anodic layers and information that would allow us to rank FFC susceptibility of anodized Al alloys.

## REFERENCES

- [1] European Aluminum Association, “Mines on Wheels Project,” 2012.
- [2] A. I. Pogue and W. J. Lukiw, “The mobilization of aluminum into the biosphere,” *Frontiers in Neurology*, vol. 5, no. DEC, p. 262, 2014, doi: 10.3389/fneur.2014.00262.
- [3] K. McCallum *et al.*, “Localized Corrosion Risk Assessment Using Markov Analysis,” *CORROSION*, vol. 70, no. 11, Nov. 2014, doi: 10.5006/1184.
- [4] J. D. Weidenhamer *et al.*, “Metal exposures from aluminum cookware: An unrecognized public health risk in developing countries,” *Science of The Total Environment*, vol. 579, Feb. 2017, doi: 10.1016/j.scitotenv.2016.11.023.
- [5] S. González, F. Cáceres, V. Fox, and R. M. Souto, “Resistance of metallic substrates protected by an organic coating containing aluminum powder,” *Progress in Organic Coatings*, vol. 46, no. 4, Jun. 2003, doi: 10.1016/S0300-9440(03)00021-3.
- [6] B. N. Popov, “Organic Coatings,” in *Corrosion Engineering*, Elsevier, 2015. doi: 10.1016/B978-0-444-62722-3.00013-6.
- [7] A. John, “Filiform corrosion of aluminium alloys and iron,” 2007. [Online]. Available: <http://cronfa.swan.ac.uk/Record/cronfa42908>
- [8] W. H. Slabaugh and M. Grotheer, “Mechanism of Filiform Corrosion,” *Industrial & Engineering Chemistry*, vol. 46, no. 5, pp. 1014–1016, May 1954, doi: 10.1021/ie50533a053.
- [9] L. Fedrizzi, F. Deflorian, S. Rossi, and P. L. Bonora, “Study of aluminium filiform corrosion by using electrochemical techniques,” *Materials Science Forum*, vol. 289–292, no. PART 1, pp. 485–498, 1998, doi: 10.4028/www.scientific.net/msf.289-292.485.

- [10] C. F. Sharman, "sharman1944," "© 1944 Nature Publishing Group," *Nature*, vol. 3890, p. 621,622, 1944., 1944.
- [11] H. Michiki and S. Toshio, "Studies on filiform corrosion generated on Al and Alalloy coated sheets\*," 1969.
- [12] "Corrosion of Aluminum and Aluminum Alloys," *J.R. Davis*, 1999, doi: 10.1361/caaa1999p001.
- [13] A. Bautista, "Filiform corrosion in polymer-coated metals," *Progress in Organic Coatings*, vol. 28, no. 1, May 1996, doi: 10.1016/0300-9440(95)00555-2.
- [14] G. D. Steele, "Filiform Corrosion on Architectural Aluminium," *Anti-Corrosion Methods and Materials*, vol. 41, no. 1, Jan. 1994, doi: 10.1108/eb007337.
- [15] Iwona Lazur, "Effect of pH on Coatings Used to Protect Aluminum Beverage Cans," Ottawa, Ontario, 2014.
- [16] J. H. Powers, "Filiform Corrosion Resistance of Painted Automotive Body Sheet," Feb. 1991. doi: 10.4271/910556.
- [17] N. le Bozec, D. Persson, A. Nazarov, and D. Thierry, "Investigation of Filiform Corrosion on Coated Aluminum Alloys by FTIR Microspectroscopy and Scanning Kelvin Probe," *Journal of The Electrochemical Society*, vol. 149, no. 9, p. B403, 2002, doi: 10.1149/1.1497172.
- [18] H. N. McMurray and G. Williams, "Under Film/Coating Corrosion," in *Reference Module in Materials Science and Materials Engineering*, Elsevier, 2016. doi: 10.1016/B978-0-12-803581-8.01601-5.

- [19] N. Lebozec, D. Persson, D. Thierry, and S. B. Axelsen, “CORROSION ENGINEERING SECTION Effect of Climatic Parameters on Filiform Corrosion of Coated Aluminum Alloys,” 2004.
- [20] Daniela Arango and Jing Liu, “ELECTROCHEMICAL STUDY OF ALUMINUM FILIFORM CORROSION,” Edmonton, Canada, 2021.
- [21] American Architectural Manufacturers Association, “Voluntary Specification, Performance Requirements and Test Procedures For Pigmented Organic Coatings on Aluminum Extrusions and Panels,” *AAMA 2603-02*, 2002.
- [22] ISO 4623-2:2016, “Paints and varnishes — Determination of resistance to filiform corrosion — Part 2: Aluminium substrates.” Aug. 2016.
- [23] J. L. Delplancke, S. Berger, X. Lefèbvre, D. Maetens, A. Pourbaix, and N. Heymans, “Filiform corrosion: interactions between electrochemistry and mechanical properties of the paints,” 2001.
- [24] P. P. Leblanc and G. S. Frankel, “Investigation of Filiform Corrosion of Epoxy-Coated 1045 Carbon Steel by Scanning Kelvin Probe Force Microscopy,” *Journal of The Electrochemical Society*, vol. 151, no. 3, 2004, doi: 10.1149/1.1641038.
- [25] A. Afseth, J. H. Nordlien, G. M. Scamans, and K. Nisancioglu, “Filiform corrosion of binary aluminium model alloys,” 2005, [Online]. Available: [www.elsevier.com/locate/corsci](http://www.elsevier.com/locate/corsci)
- [26] A. E. Al-Rawajfeh and S. M. A. al Qawabah, “Investigation of copper addition on the mechanical properties and corrosion resistance of commercially pure aluminum,” 2009.
- [27] C. F. Glover, M. L. C. Lim, G. Post, M. Mayo, and J. R. Scully, “The effect of surface treatment on the performance of a trivalent chromium process (TCP) pretreatment on

- AA7075 aerospace alloys for the protection against filiform corrosion,” *Corrosion*, vol. 75, no. 12, pp. 1513–1526, 2019, doi: 10.5006/3380.
- [28] Margreet Spoelstra, “Filiform Corrosion of Anodised Aluminum,” The Netherlands, 1999.
- [29] Jutatip Namahoot, “Effect of deformation on corrosion of Al-Mn alloys,” Edgbaston, Birmingham, United Kingdom, 2004.
- [30] H. Ä. Kon, Olsen Leth, A. Afseth, and K. Nisancioglu, “Filiform corrosion of aluminium sheet ii, electrochemical and corrosion behaviour of bare substrates,” 2005.
- [31] J. M. C. Mol, B. R. W. Hinton, D. H. van der Weijde, J. H. W. de Wit, and S. van der Zwaag, “A filiform corrosion and potentiodynamic polarisation study of some aluminium alloys,” 2000.
- [32] D. Rabinovich, “The allure of aluminium,” *Nature Chemistry*, vol. 5, no. 1. p. 76, Jan. 2013. doi: 10.1038/nchem.1535.
- [33] European Aluminum Association, “Mines on Wheels Project,” 2012.
- [34] “ThyssenKrupp Materials (UK) Ltd,” 2018.
- [35] T. Dursun and C. Soutis, “Recent developments in advanced aircraft aluminium alloys,” *Materials & Design (1980-2015)*, vol. 56, Apr. 2014, doi: 10.1016/j.matdes.2013.12.002.
- [36] K. Dehghani, A. Nekahi, and M. A. M. Mirzaie, “Using response surface methodology to optimize the strain aging response of AA5052,” *Materials Science and Engineering: A*, vol. 527, no. 27–28, Oct. 2010, doi: 10.1016/j.msea.2010.07.088.
- [37] George Totten and D. Scott MacKenzie, *Handbook of Aluminum : Physical Metallurgy and Processes*. 2003.
- [38] C. Vargel, *Corrosion of Aluminium*. 2004. 2004.

- [39] M. Ernest. Kassner and M.-Teresa. Pérez-Prado, *Fundamentals of creep in metals and alloys*. Elsevier, 2004.
- [40] Christian Vargel, *Corrosion of Aluminium*, vol. 2nd Edition. 2020.
- [41] Z. Ahmad, “ATMOSPHERIC CORROSION,” in *Principles of Corrosion Engineering and Corrosion Control*, Elsevier, 2006. doi: 10.1016/B978-075065924-6/50011-8.
- [42] R. P. and S. das R. S. Rana, “Reviews on the Influences of Alloying elements on the Microstructure and Mechanical Properties of Aluminum Alloys and Aluminum Alloy Composites,” Bhoapl-462051, India, 2012.
- [43] NACE, *NACE International Basic Corrosion Course Handbook* . Houston, TX, 2000.
- [44] Ch. Thee *et al.*, “Atmospheric corrosion monitoring of a weathering steel under an electrolyte film in cyclic wet–dry condition,” *Corrosion Science*, vol. 78, Jan. 2014, doi: 10.1016/j.corsci.2013.09.008.
- [45] C. Vargel, “Types of Corrosion on Aluminium,” in *Corrosion of Aluminium*, 2004, pp. 113–146. doi: 10.1016/B978-008044495-6/50012-4.
- [46] Joseph W. Richards, *Aluminium; its history, occurrence, properties, metallurgy and applications, including its alloys*, 3d ed. Philadelphia, 1896.
- [47] N. L. *et al.*, “Durability and Corrosion of Aluminium and Its Alloys: Overview, Property Space, Techniques and Developments,” in *Aluminium Alloys - New Trends in Fabrication and Applications*, InTech, 2012. doi: 10.5772/53752.
- [48] Philippe Marcus, Ed., *Corrosion Mechanisms in Theory and Practice*. CRC Press, 2017.
- [49] A. Kolics, A. S. Besing, P. Baradlai, R. Haasch, and A. Wieckowski, “Effect of pH on Thickness and Ion Content of the Oxide Film on Aluminum in NaCl Media,” *Journal of The Electrochemical Society*, vol. 148, no. 7, 2001, doi: 10.1149/1.1376118.

- [50] Ph. Gimenez, J. J. Rameau, and M. C. Reboul, "Experimental pH Potential Diagram of Aluminum for Sea Water," *CORROSION*, vol. 37, no. 12, Dec. 1981, doi: 10.5006/1.3577557.
- [51] K. NIŞANCIOĞLU, "Corrosion and protection of aluminum alloys in seawater," in *Corrosion Behaviour and Protection of Copper and Aluminium Alloys in Seawater*, Elsevier, 2007. doi: 10.1533/9781845693084.4.145.
- [52] Materials Engineering Research Laboratory, "Corrosion and Cathodic Protection," Denver, Colorado, 2013.
- [53] L. Kuchariková, T. Liptáková, E. Tillová, D. Kajánek, and E. Schmidová, "Role of Chemical Composition in Corrosion of Aluminum Alloys," *Metals*, vol. 8, no. 8, Jul. 2018, doi: 10.3390/met8080581.
- [54] I. A. J. Gazapo, "Basic Approaches to Prevent Corrosion of Aluminium," *TALAT Lectures 5104*, 1994.
- [55] C. Vargel, "Selection criteria," in *Corrosion of Aluminium*, Elsevier, 2020. doi: 10.1016/B978-0-08-099925-8.00007-7.
- [56] Z. Ahmad, "ATMOSPHERIC CORROSION," in *Principles of Corrosion Engineering and Corrosion Control*, Elsevier, 2006. doi: 10.1016/B978-075065924-6/50011-8.
- [57] C. Vargel, "Influence of alloy composition," in *Corrosion of Aluminium*, Elsevier, 2020. doi: 10.1016/B978-0-08-099925-8.00012-0.
- [58] Litao Yin, Christofer Leygraf, Jinshan Pan, and Ying Jin, "Modeling of micro-galvanic corrosion on Al alloys." KTH Royal Institute of Technology, Sep. 2018.

- [59] A. S. Hamdy Makhoulouf, "Intelligent Stannate-Based Coatings of Self-Healing Functionality for Magnesium Alloys," in *Intelligent Coatings for Corrosion Control*, Elsevier, 2015. doi: 10.1016/B978-0-12-411467-8.00015-5.
- [60] G. Williams and H. N. McMurray, "The Kinetics of Chloride-Induced Filiform Corrosion on Aluminum Alloy AA2024-T3," *Journal of The Electrochemical Society*, vol. 150, no. 8, 2003, doi: 10.1149/1.1589020.
- [61] Dominique Thierry, Dan Persson, and Sten Axelsen, "Effect of Climatic Parameters on the Filiform Corrosion of Coated Aluminum Alloys AA6016," 2003.
- [62] M. Huisert, "Electrochemical Characterisation of Filiform Corrosion on Aluminium Rolled Products Elektrochemische karakterisatie van filiforme corrosie op gewalste aluminium producten," 2001.
- [63] V. Dumitrascu, L. Benea, and E. Danaila, "Corrosion Behavior of Aluminum Oxide Film Growth by Controlled Anodic Oxidation," *IOP Conference Series: Materials Science and Engineering*, vol. 209, Jun. 2017, doi: 10.1088/1757-899X/209/1/012016.
- [64] Margaretha Bonny Spoelstra, "Filiform corrosion of anodised aluminium alloys," 2000.
- [65] P. Cornette, S. Zanna, A. Seyeux, D. Costa, and P. Marcus, "The native oxide film on a model aluminium-copper alloy studied by XPS and ToF-SIMS," *Corrosion Science*, vol. 174, Sep. 2020, doi: 10.1016/j.corsci.2020.108837.
- [66] E. Hughes, A. K. Neufeld, and T. Markley-Csiro, "Underfilm Corrosion on Polyurethane-Coated Aluminum Alloy 2024-T3 Containing Dissimilar Metal Fasteners," 2006. [Online]. Available: [www.coatingstech.org](http://www.coatingstech.org)
- [67] J. Weissenrieder and C. Leygraf, "In Situ Studies of Filiform Corrosion of Iron," *Journal of The Electrochemical Society*, vol. 151, no. 3, 2004, doi: 10.1149/1.1645263.

- [68] G. D. Steele, "Filiform Corrosion on Architectural Aluminium," *Anti-Corrosion Methods and Materials*, vol. 41, no. 1, Jan. 1994, doi: 10.1108/eb007337.
- [69] H. Dafydd, D. A. Worsley, and H. N. McMurray, "The kinetics and mechanism of cathodic oxygen reduction on zinc and zinc–aluminium alloy galvanized coatings," *Corrosion Science*, vol. 47, no. 12, Dec. 2005, doi: 10.1016/j.corsci.2005.05.036.
- [70] Scamans GM and Butler EP, "In situ observations of crystalline oxide formation during aluminium and aluminium alloys oxidation," in *Metallurgical Transactions A*, vol. 6A:2055e63, 1975.
- [71] C. Vargel, "The oxide film and passivity of aluminium," in *Corrosion of Aluminium*, Elsevier, 2020. doi: 10.1016/B978-0-08-099925-8.00010-7.
- [72] A. Afseth, J. H. Nordlien, G. M. Scamans, and K. Nisancioglu, "Filiform corrosion of AA3005 aluminium analogue model alloys," 2005, [Online]. Available: [www.elsevier.com/locate/corsci](http://www.elsevier.com/locate/corsci)
- [73] M. Halseid, J. T. B. Gundersen, Ø. Bauger, and T. Hentschel, "The effect of trace additions of copper and pretreatment conditions on the filiform corrosion of powder-coated aluminium alloy AA6060," *Surface and Interface Analysis*, vol. 51, no. 12, pp. 1225–1230, Dec. 2019, doi: 10.1002/sia.6621.
- [74] C. F. Glover, M. L. C. Lim, and J. R. Scully, "The Effect of Surface Treatment on the Performance of a Zirconium-Based Conversion Coating on AA7075 Automotive Alloys for Protection Against Filiform Corrosion," *Minerals, Metals and Materials Series*, pp. 937–946, 2020, doi: 10.1007/978-3-030-36296-6\_87.

- [75] Y. Liu *et al.*, “Influence of near-surface deformed layers on filiform corrosion of AA3104 aluminium alloy,” in *Surface and Interface Analysis*, Oct. 2013, vol. 45, no. 10, pp. 1553–1557. doi: 10.1002/sia.5232.
- [76] A. Jordan, “Microstructure Characterization and Corrosion Properties of Two Recycled Aluminium Alloys AA5050 and AA6011,” 2016.
- [77] X. F. Liu, “Filiform corrosion attack on pretreated aluminum alloy with tailored surface of epoxy coating,” *Corrosion Science*, vol. 49, no. 9, Sep. 2007, doi: 10.1016/j.corsci.2007.03.031.
- [78] J. M. C. Mol, J. van de Langkruis, J. H. W. de Wit, and S. van der Zwaag, “An integrated study on the effect of pre- and post-extrusion heat treatments and surface treatment on the filiform corrosion properties of an aluminium extrusion alloy,” *Corrosion Science*, vol. 47, no. 11, Nov. 2005, doi: 10.1016/j.corsci.2004.11.003.
- [79] M. Halseid, J. T. B. Gundersen, Ø. Bauger, and T. Hentschel, “The effect of trace additions of copper and pretreatment conditions on the filiform corrosion of powder-coated aluminium alloy AA6060,” *Surface and Interface Analysis*, vol. 51, no. 12, pp. 1225–1230, 2019, doi: 10.1002/sia.6621.
- [80] R. S. Huang, C. J. Lin, and H. S. Isaacs, “A difference-imaging technique used to study streaking corrosion of aluminum alloys AA7075 and AA8006 in chloride solution,” *Electrochemical and Solid-State Letters*, vol. 9, no. 2, 2006, doi: 10.1149/1.2140503.
- [81] G. J. Courval, B. Chamberlain, and D. Pattemore, “Effects of Alloy Composition and Condition on Filiform Corrosion Performance of Cast Aluminum Wheels,” *JOURNAL OF MATERIALS & MANUFACTURING*, vol. 106, pp. 75–83, 1997.

- [82] Christopher Hahin and ; Rudolph G. Buchheit, "Filiform Corrosion," in *Corrosion: Fundamentals, Testing, and Protection*, ASM International, 2003. doi: 10.31399/asm.hb.v13a.a0003614.
- [83] L. Fedrizzi, A. Bianchi, F. Deflorian, S. Rossi, and P. L. Bonora, "Effect of chemical cleaning on the corrosion behaviour of painted aluminium alloys," 2002. [Online]. Available: [www.elsevier.com/locate/electacta](http://www.elsevier.com/locate/electacta)
- [84] M. Costa and C. B. Klein, "Toxicity and Carcinogenicity of Chromium Compounds in Humans," *Critical Reviews in Toxicology*, vol. 36, no. 2, Jan. 2006, doi: 10.1080/10408440500534032.
- [85] World Health Organization, "International Agency for Research on Cancer (IARC)," *IARC monographs*, vol. 1-109., 2006.
- [86] Agency for Toxic Substances and Disease Registry (ATSDR), "Toxicological Profile for Chromium," *U.S. Public Health Service, U.S. Department of Health and Human Services, Atlanta, GA.*, 1998.
- [87] D. Chidambaram, M. Jaime Vasquez, G. P. Halada, and C. R. Clayton, "Studies on the repassivation behavior of aluminum and aluminum alloy exposed to chromate solutions," *Surface and Interface Analysis*, vol. 35, no. 2, Feb. 2003, doi: 10.1002/sia.1507.
- [88] C. A. Grubbs, "Anodizing of aluminum," *Metal Finishing*, vol. 97, no. 1, Jan. 1999, doi: 10.1016/S0026-0576(99)80049-X.
- [89] J. A. González, M. Morcillo, E. Escudero, V. López, and E. Otero, "Atmospheric corrosion of bare and anodized aluminium in a wide range of environmental conditions. Part I: Visual observations and gravimetric results," *Surface and Coatings Technology*, vol. 153, no. 2–3, Apr. 2002, doi: 10.1016/S0257-8972(01)01680-2.

- [90] A. Doublet *et al.*, “Bifunctional coatings: coupling an organic adhesion promoter with an anticorrosion inorganic layer,” *RSC Advances*, vol. 9, no. 42, 2019, doi: 10.1039/C9RA03657A.
- [91] T. Hryniewicz, “Concept of microsmoothing in the electropolishing process,” *Surface and Coatings Technology*, vol. 64, no. 2, May 1994, doi: 10.1016/S0257-8972(09)90006-8.
- [92] M. L. Saad, M. H. Sar, O. S. Barrak, S. K. Hussein, and A. K. Hussein, “Fuzzy logic model analysis of shear force in aluminium / polyethylene lap joined by hot press,” *IOP Conference Series: Materials Science and Engineering*, vol. 518, Jun. 2019, doi: 10.1088/1757-899X/518/3/032007.
- [93] G. C. Wood and J. P. O’Sullivan, “The anodizing of aluminium in sulphate solutions,” *Electrochimica Acta*, vol. 15, no. 12, Dec. 1970, doi: 10.1016/0013-4686(70)85024-1.
- [94] N. Hu, X. Dong, X. He, J. F. Browning, and D. W. Schaefer, “Effect of sealing on the morphology of anodized aluminum oxide,” *Corrosion Science*, vol. 97, Aug. 2015, doi: 10.1016/j.corsci.2015.03.021.
- [95] T. C. Simpson, “Accelerated Corrosion Test for Aluminum-Zinc Alloy Coatings,” *CORROSION*, vol. 49, no. 7, Jul. 1993, doi: 10.5006/1.3316084.
- [96] I. T. Kim and Y. Itoh, “Accelerated exposure tests as evaluation tool for estimating life of organic coatings on steel bridges,” *Corrosion Engineering, Science and Technology*, vol. 42, no. 3, Sep. 2007, doi: 10.1179/174327807X214833.
- [97] QUALICOAT Specifications, “Specifications for a quality label for liquid and powder coatings on Al for architectural applications,” 2021.

- [98] American Architectural Manufacturers Association, “AAMA 2603-02, Voluntary Specification, Performance Requirements and Test Procedures for Pigmented Organic Coatings on Al Extrusions and Panels,” Schaumburg, IL, 2002.
- [99] ASTM International, “ASTM D2803-09(2020), Standard Guide for Testing Filiform Corrosion Resistance of Organic Coatings on Metal,” West Conshohocken, 2020.
- [100] ASTM International, “ASTM D1654-05, Standard Test Method for Evaluation of Painted or Coated Specimens Subjected to Corrosive Environments,” West Conshohocken, 2005.
- [101] ASTM International, “ASTM D714-02(2017), Standard Test Method for Evaluating Degree of Blistering of Paints,” West Conshohocken, PA, 2017.
- [102] ASTM International, “ASTM D2247-15(2020), Standard Practice for Testing Water Resistance of Coatings in 100 % Relative Humidity,” West Conshohocken, PA, 2020.
- [103] ISO International Organization for Standardization, “Paints and varnishes. Evaluation of degradation of coatings. Designation of quantity and size of defects, and of intensity of uniform changes in appearance,” 2016.
- [104] Corrosion Tests In Artificial Atmospheres - Salt Spray Tests, “Corrosion Tests In Artificial Atmospheres - Salt Spray Tests,” 2017.
- [105] J. R. Davis, *Surface Engineering for Corrosion and Wear Resistance*. ASM International, 2001, 2001.
- [106] N. LeBozec, D. Persson, D. Thierry, and S. B. Axelsen, “Effect of Climatic Parameters on Filiform Corrosion of Coated Aluminum Alloys,” *CORROSION*, vol. 60, no. 6, Jun. 2004, doi: 10.5006/1.3287763.
- [107] “Corrosion Testing, Monitoring and Inspection,” in *Corrosion and Protection*, London: Springer London. doi: 10.1007/978-1-85233-845-9\_9.

- [108] D. C. Silverman, "Practical Corrosion Prediction Using Electrochemical Techniques," in *Uhlig's Corrosion Handbook*, Hoboken, NJ, USA: John Wiley & Sons, Inc., 2011. doi: 10.1002/9780470872864.ch85.
- [109] J. Oldfield, "Electrochemical Theory of Galvanic Corrosion," in *Galvanic Corrosion*, 100 Barr Harbor Drive, PO Box C700, West Conshohocken, PA 19428-2959: ASTM International. doi: 10.1520/STP26188S.
- [110] H. Leidheiser, "Electrical and electrochemical measurements as predictors of corrosion at the metal—organic coating interface," *Progress in Organic Coatings*, vol. 7, no. 1, Mar. 1979, doi: 10.1016/0300-9440(79)80038-7.
- [111] H. Takahashi and M. Chiba, "Role of anodic oxide films in the corrosion of aluminum and its alloys," *Corrosion Reviews*, vol. 36, no. 1, Feb. 2018, doi: 10.1515/corrrev-2017-0048.
- [112] C. Vargel, "The notion of potential," in *Corrosion of Aluminium*, Elsevier, 2020. doi: 10.1016/B978-0-08-099925-8.00009-0.
- [113] D. Snihirova, L. Liphardt, G. Grundmeier, and F. Montemor, "Electrochemical study of the corrosion inhibition ability of 'smart' coatings applied on AA2024," *Journal of Solid State Electrochemistry*, vol. 17, no. 8, Aug. 2013, doi: 10.1007/s10008-013-2078-3.
- [114] S.-J. Kim and J.-Y. Ko, "Electrochemical properties of Al and Al alloys relevant to corrosion protection in seawater environments," *Korean Journal of Chemical Engineering*, vol. 23, no. 5, Sep. 2006, doi: 10.1007/BF02705939.
- [115] M. Huisert, "Electrochemical characterisation of filiform corrosion on aluminium rolled products. ," 2001.
- [116] "ASTM G69-20 Standard Test Method for Measurement of Corrosion Potentials of Aluminum Alloys," 2020.

- [117] B. LIU, X. rong ZHOU, and X. xin ZHANG, “Filiform corrosion behaviour on machined AA7150 aluminium alloy,” *Transactions of Nonferrous Metals Society of China (English Edition)*, vol. 30, no. 8, pp. 2056–2066, Aug. 2020, doi: 10.1016/S1003-6326(20)65360-2.
- [118] Y. Tang, Y. Zuo, J. Wang, X. Zhao, B. Niu, and B. Lin, “The metastable pitting potential and its relation to the pitting potential for four materials in chloride solutions,” *Corrosion Science*, vol. 80, Mar. 2014, doi: 10.1016/j.corsci.2013.11.015.
- [119] B. Zaid, D. Saidi, A. Benzaid, and S. Hadji, “Effects of pH and chloride concentration on pitting corrosion of AA6061 aluminum alloy,” *Corrosion Science*, vol. 50, no. 7, Jul. 2008, doi: 10.1016/j.corsci.2008.03.006.
- [120] Z. Yang, B. Kan, J. Li, L. Qiao, A. A. Volinsky, and Y. Su, “A Statistical Study on the Effect of Hydrostatic Pressure on Metastable Pitting Corrosion of X70 Pipeline Steel,” *Materials*, vol. 10, no. 11, Nov. 2017, doi: 10.3390/ma10111307.
- [121] F. Andreatta, H. Terryn, and J. H. W. de Wit, “Corrosion behaviour of different tempers of AA7075 aluminium alloy,” *Electrochimica Acta*, vol. 49, no. 17–18, Jul. 2004, doi: 10.1016/j.electacta.2004.01.046.
- [122] X. Zhang, X. Zhou, T. Hashimoto, and B. Liu, “Localized corrosion in AA2024-T351 aluminium alloy: Transition from intergranular corrosion to crystallographic pitting,” *Materials Characterization*, vol. 130, Aug. 2017, doi: 10.1016/j.matchar.2017.06.022.
- [123] Z. Zhao and G. S. Frankel, “On the first breakdown in AA7075-T6,” *Corrosion Science*, vol. 49, no. 7, Jul. 2007, doi: 10.1016/j.corsci.2007.02.001.
- [124] H. N. McMurray and G. Williams, “2.14 Under Film/Coating Corrosion,” 2005.
- [125] R. S. Rana, Rajesh Purohit, and S Das, “Reviews on the Influences of Alloying elements on the Microstructure and Mechanical Properties of Aluminum Alloys and Aluminum Alloy

- Composites,” *International Journal of Scientific and Research Publications*, vol. 2, Jun. 2012.
- [126] J. E. Dorn, P. Pietrokowsky, and T. E. Tietz, “The effect of alloying elements on the plastic properties of aluminum alloys,” *JOM*, vol. 2, no. 7, Jul. 1950, doi: 10.1007/BF03399086.
- [127] S. v. Sajadifar, E. Scharifi, U. Weidig, K. Steinhoff, and T. Niendorf, “Effect of Tool Temperature on Mechanical Properties and Microstructure of Thermo-Mechanically Processed AA6082 and AA7075 Aluminum Alloys,” *HTM Journal of Heat Treatment and Materials*, vol. 75, no. 3, Jun. 2020, doi: 10.3139/105.110412.
- [128] S. G. , A.-S. M. A. , T. A. M. , & A.-W. M. Hussein, “ Effect of Heat Treatment on Mechanical and Vibration Properties for 6061 and 2024 Aluminum Alloys,” *Journal of Mechanical Engineering Research and Developments*, pp. 48–68, 2020.
- [129] J. P. Mercier, G. Zambelli, and W. Kurz, “Microstructures,” in *Introduction to Materials Science*, Elsevier, 2002. doi: 10.1016/B978-2-84299-286-6.50016-0.
- [130] J. E. DRALEY and W. E. RUTHER, “Aqueous Corrosion of Aluminum,” *Corrosion*, vol. 12, no. 9, Sep. 1956, doi: 10.5006/0010-9312-12.9.31.
- [131] Y. Pan, Y. Shen, and P. Zhao, “The Microstructure and Deformation Behavior of Al-Fe-Mn Alloys with Different Fe Contents during Cold Rolling,” *Metals*, vol. 8, no. 10, Sep. 2018, doi: 10.3390/met8100753.
- [132] K. F. O. Seri, “Effect of Al-Fe-Si intermetallic compound phases on initiation and propagation of pitting attacks for aluminum 1100,” in *Materials and Corrosion/Werkstoffe und Korrosion*, vol. 53, 2002.

- [133] H. Ezuber, A. El-Houd, and F. El-Shawesh, "A study on the corrosion behavior of aluminum alloys in seawater," *Materials & Design*, vol. 29, no. 4, Jan. 2008, doi: 10.1016/j.matdes.2007.01.021.
- [134] T. Staab, P. Folegati, I. Wolfertz, and M. Puska, "Stability of Cu-Precipitates in Al-Cu Alloys," *Applied Sciences*, vol. 8, no. 6, Jun. 2018, doi: 10.3390/app8061003.
- [135] T. Balarami Reddy, P. Karthik, and M. Gopi Krishna, "Mechanical behavior of Al-Cu binary alloy system/ Cu particulates reinforced metal-metal composites," *Results in Engineering*, vol. 4, Dec. 2019, doi: 10.1016/j.rineng.2019.100046.
- [136] Valerie Guillaumin and Georges Mankowski, "Localized corrosion of 1913 T240 aluminium alloy in chloride media," *Corrosion Science*, vol. 41, Jun. 1998.
- [137] A. Staszczuk, J. Sawicki, and B. Adamczyk-Cieslak, "A Study of Second-Phase Precipitates and Dispersoid Particles in 2024 Aluminum Alloy after Different Aging Treatments," *Materials*, vol. 12, no. 24, Dec. 2019, doi: 10.3390/ma12244168.
- [138] P. Cornette, S. Zanna, A. Seyeux, D. Costa, and P. Marcus, "The native oxide film on a model aluminium-copper alloy studied by XPS and ToF-SIMS," *Corrosion Science*, vol. 174, Sep. 2020, doi: 10.1016/j.corsci.2020.108837.
- [139] Z. Huda and T. Zaharinie, "Kinetics of grain growth in 2024-T3: An aerospace aluminum alloy," *Journal of Alloys and Compounds*, vol. 478, no. 1–2, Jun. 2009, doi: 10.1016/j.jallcom.2008.11.071.
- [140] S. W. Nam and D. H. Lee, "The effect of Mn on the mechanical behavior of Al alloys," *Metals and Materials*, vol. 6, no. 1, Jan. 2000, doi: 10.1007/BF03026339.

- [141] Y. J. Li and L. Arnberg, "Evolution of eutectic intermetallic particles in DC-cast AA3003 alloy during heating and homogenization," *Materials Science and Engineering: A*, vol. 347, no. 1–2, Apr. 2003, doi: 10.1016/S0921-5093(02)00555-5.
- [142] Y. Liu, G. Z. Meng, and Y. F. Cheng, "Electronic structure and pitting behavior of 3003 aluminum alloy passivated under various conditions," *Electrochimica Acta*, vol. 54, no. 17, Jul. 2009, doi: 10.1016/j.electacta.2009.02.058.
- [143] A. Davoodi, J. Pan, C. Leygraf, and S. Norgren, "Integrated AFM and SECM for in situ studies of localized corrosion of Al alloys," *Electrochimica Acta*, vol. 52, no. 27, Oct. 2007, doi: 10.1016/j.electacta.2006.12.073.
- [144] Kim, Kapun, Tiringir, Šekularac, and Milošev, "Protection of Aluminum Alloy 3003 in Sodium Chloride and Simulated Acid Rain Solutions by Commercial Conversion Coatings Containing Zr and Cr," *Coatings*, vol. 9, no. 9, Sep. 2019, doi: 10.3390/coatings9090563.
- [145] Y. S. Sato, Y. Sugiura, Y. Shoji, S. H. C. Park, H. Kokawa, and K. Ikeda, "Post-weld formability of friction stir welded Al alloy 5052," *Materials Science and Engineering: A*, vol. 369, no. 1–2, Mar. 2004, doi: 10.1016/j.msea.2003.11.035.
- [146] I. J. POLMEAR and K. R. SARGANT, "Enhanced Age-hardening in Aluminium–Magnesium Alloys," *Nature*, vol. 200, no. 4907, Nov. 1963, doi: 10.1038/200669b0.
- [147] John E. Hatch, "Chapter 3: Microstructure of alloys," in *Aluminum Properties and Physical Metallurgy*, 1984, pp. 58–104.
- [148] B. WANG, X. CHEN, F. PAN, J. MAO, and Y. FANG, "Effects of cold rolling and heat treatment on microstructure and mechanical properties of AA 5052 aluminum alloy," *Transactions of Nonferrous Metals Society of China*, vol. 25, no. 8, Aug. 2015, doi: 10.1016/S1003-6326(15)63866-3.

- [149] S. H. Lee, Y. Saito, T. Sakai, and H. Utsunomiya, “Microstructures and mechanical properties of 6061 aluminum alloy processed by accumulative roll-bonding,” *Materials Science and Engineering: A*, vol. 325, no. 1–2, Feb. 2002, doi: 10.1016/S0921-5093(01)01416-2.
- [150] S. N. Samaras and G. N. Haidemenopoulos, “Modelling of microsegregation and homogenization of 6061 extrudable Al-alloy,” *Journal of Materials Processing Technology*, vol. 194, no. 1–3, Nov. 2007, doi: 10.1016/j.jmatprotec.2007.03.126.
- [151] N. C. W. Kuijpers, W. H. Kool, P. T. G. Koenis, K. E. Nilsen, I. Todd, and S. van der Zwaag, “Assessment of different techniques for quantification of  $\alpha$ -Al(FeMn)Si and  $\beta$ -AlFeSi intermetallics in AA 6xxx alloys,” *Materials Characterization*, vol. 49, no. 5, Dec. 2002, doi: 10.1016/S1044-5803(03)00036-6.
- [152] K. Mutombo, “Intermetallic Particles-Induced Pitting Corrosion in 6061-T651 Aluminium Alloy,” *Materials Science Forum*, vol. 690, Jun. 2011, doi: 10.4028/www.scientific.net/MSF.690.389.
- [153] B.-A. Behrens, F. Nürnberger, C. Bonk, S. Hübner, S. Behrens, and H. Vogt, “Influences on the formability and mechanical properties of 7000-aluminum alloys in hot and warm forming,” *Journal of Physics: Conference Series*, vol. 896, Sep. 2017, doi: 10.1088/1742-6596/896/1/012004.
- [154] John E. Hatch e, “Chapter 2: Constitution of Alloys,” in *Aluminum Properties and Physical Metallurgy*, 1984, pp. 25–57.
- [155] S. S. Singh, E. Guo, H. Xie, and N. Chawla, “Mechanical properties of intermetallic inclusions in Al 7075 alloys by micropillar compression,” *Intermetallics*, vol. 62, Jul. 2015, doi: 10.1016/j.intermet.2015.03.008.

- [156] A. Ghosh and M. Ghosh, "Microstructure and texture development of 7075 alloy during homogenisation," *Philosophical Magazine*, vol. 98, no. 16, Jun. 2018, doi: 10.1080/14786435.2018.1439596.
- [157] A. N. Aliyah and A. Anawati, "Effect of Heat Treatment on Microstructure and mechanical hardness of aluminum alloy AA7075," *IOP Conference Series: Materials Science and Engineering*, vol. 541, Jul. 2019, doi: 10.1088/1757-899X/541/1/012007.
- [158] R. G. Buchheit, R. K. Boger, M. C. Carroll, R. M. Leard, C. Paglia, and J. L. Searles, "The electrochemistry of intermetallic particles and localized corrosion in Al alloys," *JOM*, vol. 53, no. 7, Jul. 2001, doi: 10.1007/s11837-001-0084-x.
- [159] Y. Zhu, K. Sun, and G. S. Frankel, "Intermetallic Phases in Aluminum Alloys and Their Roles in Localized Corrosion," *Journal of The Electrochemical Society*, vol. 165, no. 11, Aug. 2018, doi: 10.1149/2.0931811jes.
- [160] Z. Szklarska-Smialowska, "Pitting corrosion of aluminum," *Corrosion Science*, vol. 41, no. 9, Aug. 1999, doi: 10.1016/S0010-938X(99)00012-8.
- [161] N. Birbilis and R. G. Buchheit, "Electrochemical Characteristics of Intermetallic Phases in Aluminum Alloys," *Journal of The Electrochemical Society*, vol. 152, no. 4, 2005, doi: 10.1149/1.1869984.
- [162] J. Li and J. Dang, "A Summary of Corrosion Properties of Al-Rich Solid Solution and Secondary Phase Particles in Al Alloys," *Metals*, vol. 7, no. 3, Mar. 2017, doi: 10.3390/met7030084.
- [163] N. LeBozec, D. Persson, and D. Thierry, "In Situ Studies of the Initiation and Propagation of Filiform Corrosion on Aluminum," *Journal of The Electrochemical Society*, vol. 151, no. 7, p. B440, 2004, doi: 10.1149/1.1760577.

- [164] P. Marcus, V. Maurice, S. Zein, E. Abedin,^^, and F. Endres^, “Passivation of Metals and Semiconductors, and Properties of Thin Oxide Layers Electrochemical behaviour of Al and some of its alloys in chloride solutions,” 2006.
- [165] J. Liu, A. Alfantazi, and E. Asselin, “Effects of Temperature and Sulfate on the Pitting Corrosion of Titanium in High-Temperature Chloride Solutions,” *Journal of The Electrochemical Society*, vol. 162, no. 4, Jan. 2015, doi: 10.1149/2.0541504jes.
- [166] Brian E. Placzankis, “General Corrosion Resistance Comparisons of Medium- and High-Strength Aluminum Alloys for DOD Systems Using Laboratory-Based Accelerated Corrosion Methods,” *Army Research Laboratory*, Sep. 2009.
- [167] J. R. Davis, “Pitting and Crevice Corrosion,” in *Corrosion of Aluminum and Aluminum Alloys*, ASM International, 1999. doi: 10.31399/asm.tb.caaa.t67870045.
- [168] S.-S. Wang *et al.*, “Effect of Cu Content and Aging Conditions on Pitting Corrosion Damage of 7xxx Series Aluminum Alloys,” *Journal of The Electrochemical Society*, vol. 162, no. 4, Jan. 2015, doi: 10.1149/2.0301504jes.
- [169] R. K. Gupta, N. L. Sukiman, M. K. Cavanaugh, B. R. W. Hinton, C. R. Hutchinson, and N. Birbilis, “Metastable pitting characteristics of aluminium alloys measured using current transients during potentiostatic polarisation,” *Electrochimica Acta*, vol. 66, Apr. 2012, doi: 10.1016/j.electacta.2012.01.090.
- [170] U. Donatus *et al.*, “Corrosion Resistance of Precipitation-Hardened Al Alloys: A Comparison between New Generation Al-Cu-Li and Conventional Alloys,” in *Advanced Aluminium Composites and Alloys*, IntechOpen, 2021. doi: 10.5772/intechopen.92807.
- [171] Valerie Guillaumin and Georges Mankowski, “Localized corrosion of 1913 T240 aluminium alloy in chloride media,” *Corrosion Science*, 1999.

- [172] L. Calabrese, L. Bonaccorsi, A. Capri, and E. Proverbio, "Electrochemical behavior of hydrophobic silane–zeolite coatings for corrosion protection of aluminum substrate," *Journal of Coatings Technology and Research*, vol. 11, no. 6, Nov. 2014, doi: 10.1007/s11998-014-9597-4.
- [173] D. Lee, H. Lee, and H. Jeong, "Slurry components in metal chemical mechanical planarization (CMP) process: A review," *International Journal of Precision Engineering and Manufacturing*, vol. 17, no. 12, Dec. 2016, doi: 10.1007/s12541-016-0201-y.
- [174] Philip A, "Corrosion Engineering Handbook," 2nd ed., vol. 3, Schweitzer, P.E., 1996, pp. 124–125.
- [175] P. Rodič and I. Milošev, "Corrosion Inhibition of Pure Aluminium and Alloys AA2024-T3 and AA7075-T6 by Cerium(III) and Cerium(IV) Salts," *Journal of The Electrochemical Society*, vol. 163, no. 3, Dec. 2016, doi: 10.1149/2.0431603jes.
- [176] I.-W. Huang, B. L. Hurley, F. Yang, and R. G. Buchheit, "Dependence on Temperature, pH, and Cl<sup>-</sup> in the Uniform Corrosion of Aluminum Alloys 2024-T3, 6061-T6, and 7075-T6," *Electrochimica Acta*, vol. 199, May 2016, doi: 10.1016/j.electacta.2016.03.125.
- [177] A. J. Coleman, "Filiform corrosion of aluminium alloys and iron," 2007.
- [178] Q. Meng and G. S. Frankel, "Effect of Cu Content on Corrosion Behavior of 7xxx Series Aluminum Alloys," *Journal of The Electrochemical Society*, vol. 151, no. 5, 2004, doi: 10.1149/1.1695385.
- [179] Mariano Iannuzzi, "How to determine pitting and repassivation potentials," 2014.
- [180] Shan-Shan Wang, Fan Yang, and G. S. Frankel, "Effect of Altered Surface Layer on Localized Corrosion of Aluminum Alloy 2024," *Journal of The Electrochemical Society*, vol. 164, no. 6, Apr. 2017.

- [181] Z. Zhao and G. S. Frankel, "On the first breakdown in AA7075-T6," *Corrosion Science*, vol. 49, no. 7, Jul. 2007, doi: 10.1016/j.corsci.2007.02.001.
- [182] K. Srinivasa Rao and Prasad Kalvala, "Pitting corrosion of heat-treatable aluminium alloys and welds: A review," Dec. 2004.
- [183] R. Escalera-Lozano, M.I. Pech-Canul, and A. Uribe-Salas, "The Role of Mg<sub>2</sub>Si in the Corrosion Behavior of Al-Si-Mg Alloys for Pressureless Infiltration," *The Open Corrosion Journal*, pp. 73–79, 2010.
- [184] N. , E. D. , Wint, E. , Michailidou, A. , Bennett, Searle, W. J. R., and & M. H. N. G., "The kinetics and mechanism of filiform corrosion occurring on zinc-aluminium-magnesium coated steel," 2019.
- [185] ASTM International, "ASTM G69-97, Standard Test Method for Measurement of Corrosion Potentials of Aluminum Alloys," West Conshohocken, PA, , 1997.
- [186] Mahdi Che Isa *et al.*, "Electrochemical Characterisation of As-Cast Al-Zn-Sn and Al-Zn-Mg-Sn Alloys for Corrosion Control Application in Tropical Marine Environments," *Defence S and T Technical Bulletin*, 2011.
- [187] S. Liu, L. Liu, F. Meng, Y. Li, and F. Wang, "Protective Performance of Polyaniline-Sulfosalicylic Acid/Epoxy Coating for 5083 Aluminum," *Materials*, vol. 11, no. 2, Feb. 2018, doi: 10.3390/ma11020292.
- [188] O. Seri and K. Furumata, "Effect of Al-Fe-Si intermetallic compound phases on initiation and propagation of pitting attacks for aluminum 1100\*," 2002, pp. 111–120.
- [189] D. v. Dzhurinskiy, S. S. Dautov, P. G. Shornikov, and I. Sh. Akhatov, "Surface Modification of Aluminum 6061-O Alloy by Plasma Electrolytic Oxidation to Improve Corrosion Resistance Properties," *Coatings*, vol. 11, no. 1, Dec. 2020, doi: 10.3390/coatings11010004.

- [190] N. Zidane *et al.*, “Effect of Gadolinium Content on the Corrosion Behavior of Magnesium Alloys in 1 wt.% NaCl Solution,” *Portugaliae Electrochimica Acta*, vol. 33, no. 5, 2015, doi: 10.4152/pea.201505289.
- [191] M. Šeruga and D. Hasenay, “Electrochemical and surface properties of aluminum in citric acid solutions,” *Journal of Applied Electrochemistry*, vol. 31, no. 9, 2001, doi: 10.1023/A:1017556323508.
- [192] F. Ropital, “Environmental degradation in hydrocarbon fuel processing plant: issues and mitigation,” in *Advances in Clean Hydrocarbon Fuel Processing*, Elsevier, 2011. doi: 10.1533/9780857093783.5.437.
- [193] Ahmed Musa, Abdul Amir Hassan Kadhum, and Abu Baker Muhamad, “Corrosion Inhibitor Film Forming in Aerated and Deaerated Solutions,” *International Journal of Electrochemical Science*, Dec. 2010.
- [194] K. Nisancioglu and H. Holtan, “The protection potential of aluminium,” *Corrosion Science*, vol. 18, no. 11, Jan. 1978, doi: 10.1016/0010-938X(78)90035-5.
- [195] R. A. Buchanan and E. E. Stansbury, “Electrochemical Corrosion,” in *Handbook of Environmental Degradation of Materials*, Elsevier, 2012. doi: 10.1016/B978-1-4377-3455-3.00004-3.
- [196] Y.-M. Han and X.-G. Chen, “Electrochemical Behavior of Al-B4C Metal Matrix Composites in NaCl Solution,” *Materials*, vol. 8, no. 9, Sep. 2015, doi: 10.3390/ma8095314.
- [197] E. McCafferty, “Validation of corrosion rates measured by the Tafel extrapolation method,” *Corrosion Science*, vol. 47, no. 12, Dec. 2005, doi: 10.1016/j.corsci.2005.05.046.

- [198] Hongxin Wang, Yingwei Song, Jin Yu, Dayong Shan, and Hou Han, “Characterization of Filiform Corrosion of Mg–3Zn Mg Alloy,” *Journal of The Electrochemical Society*, Apr. 2017.
- [199] N. Wint, D. Eaves, G. Williams, and H. N. McMurray, “The effect of composition and thickness on the mechanism and kinetics of filiform corrosion occurring on zinc-aluminium-magnesium coated steel,” *Corrosion Science*, vol. 179, Feb. 2021, doi: 10.1016/j.corsci.2020.109168.
- [200] G. Yang, B. Wang, K. Tawfiq, H. Wei, S. Zhou, and G. Chen, “Electropolishing of surfaces: theory and applications,” *Surface Engineering*, vol. 33, no. 2, pp. 149–166, Feb. 2017, doi: 10.1080/02670844.2016.1198452.
- [201] Benu Chatterjee, “Science and Industry of Electropolishing,” *Galvanotechnik*, vol. 71, no. 1, pp. 71–93, Jan. 2015.
- [202] M. Saenz de Miera, M. Curioni, P. Skeldon, and G. E. Thompson, “Modelling the anodizing behaviour of aluminium alloys in sulphuric acid through alloy analogues,” *Corrosion Science*, vol. 50, no. 12, pp. 3410–3415, Dec. 2008, doi: 10.1016/j.corsci.2008.09.019.
- [203] M. Curioni, “Macroscopic and Local Filming Behavior of AA2024 T3 Aluminum Alloy during Anodizing in Sulfuric Acid Electrolyte,” *Journal of The Electrochemical Society*, vol. 155, no. 8, Jun. 2008.
- [204] I. Tsangaraki-Kaplanoglou, S. Theohari, Th. Dimogerontakis, Y.-M. Wang, H.-H. (Harry) Kuo, and S. Kia, “Effect of alloy types on the anodizing process of aluminum,” *Surface and Coatings Technology*, vol. 200, no. 8, pp. 2634–2641, Jan. 2006, doi: 10.1016/j.surfcoat.2005.07.065.

- [205] M. Saenz de Miera, M. Curioni, P. Skeldon, and G. E. Thompson, “The behaviour of second phase particles during anodizing of aluminium alloys,” *Corrosion Science*, vol. 52, no. 7, pp. 2489–2497, Jul. 2010, doi: 10.1016/j.corsci.2010.03.029.
- [206] Y. Ma *et al.*, “Anodic film growth on Al–Li–Cu alloy AA2099-T8,” *Electrochimica Acta*, vol. 80, pp. 148–159, Oct. 2012, doi: 10.1016/j.electacta.2012.06.126.
- [207] Tahir Ahmad, “Effect of Magnesium Content and Temperature on the Morphology and Chemical Composition of Anodized Layer of Al Alloys,” *Journal of Pakistan Institute of Chemical Engineers*, vol. 43, no. 1, pp. 111–116, 2015.
- [208] Y. Liu *et al.*, “Corrosion behaviour of mechanically polished AA7075-T6 aluminium alloy,” *Surface and Interface Analysis*, vol. 42, no. 4, pp. 185–188, Apr. 2010, doi: 10.1002/sia.3136.
- [209] S. Zheng *et al.*, “Fabrication of a micro-nanostructured superhydrophobic aluminum surface with excellent corrosion resistance and anti-icing performance,” *RSC Advances*, vol. 6, no. 83, pp. 79389–79400, 2016, doi: 10.1039/C6RA13447E.
- [210] Dalip Singh, Veena Dhayal, and Dinesh Chandra Agarwal, “Corrosion Performance of Nano-Alumina Coatings over Anodized Aluminum Alloy by Dip Coating Method,” *Surface Engineering and Applied Electrochemistry*, vol. 55, no. 4, pp. 436–442, Jul. 2019, doi: 10.3103/S1068375519040148.
- [211] R D Montoya Z, E Vera L, Y Pineda T, and M L Cedeño, “Effect of the layer of anodized 7075-T6 aluminium corrosion properties,” *Journal of Physics: Conference Series*, 2017.
- [212] J. Lee, Y. Kim, H. Jang, U. Jung, and W. Chung, “Cr<sub>2</sub>O<sub>3</sub> Sealing of Anodized Aluminium Alloy by Heat Treatment,” *Procedia Engineering*, vol. 10, pp. 2803–2808, 2011, doi: 10.1016/j.proeng.2011.04.466.

- [213] M. García-Rubio *et al.*, “Effect of posttreatment on the corrosion behaviour of tartaric–sulphuric anodic films,” *Electrochimica Acta*, vol. 54, no. 21, pp. 4789–4800, Aug. 2009, doi: 10.1016/j.electacta.2009.03.083.
- [214] L. E. Fratila-Apachitei *et al.*, “A transmission electron microscopy study of hard anodic oxide layers on AlSi(Cu) alloys,” *Electrochimica Acta*, vol. 49, no. 19, pp. 3169–3177, Aug. 2004, doi: 10.1016/j.electacta.2004.02.030.
- [215] G.-L. Song and Z. Shi, “Anodization and corrosion of magnesium (Mg) alloys,” in *Corrosion Prevention of Magnesium Alloys*, Elsevier, 2013, pp. 232–281. doi: 10.1533/9780857098962.2.232.
- [216] H. Habazaki, K. Shimizu, P. Skeldon, G. E. Thompson, G. C. Wood, and X. Zhou, “Effects of Alloying Elements in Anodizing of Aluminium,” *Transactions of the IMF*, vol. 75, no. 1, pp. 18–23, Jan. 1997, doi: 10.1080/00202967.1997.11871137.
- [217] Chia-Jung Hu, Liu-Ho Chiu, Chi-Ying Tsai, and Kuan-Hung Chen, “Effect of Coarse Second-Phase Particles on Galvanic Corrosion of Anodized 6061 Aluminum Alloy Coupled with C1 100 Copper,” *International Journal of Electrochemical Science*, vol. 10, no. 8, pp. 6572–6585, Jun. 2015.
- [218] C. Vargel, “Protection of aluminium,” in *Corrosion of Aluminium*, Elsevier, 2020, pp. 383–443. doi: 10.1016/B978-0-08-099925-8.00029-6.
- [219] T.M.Watson and H.N.McMurray, “The Mechanism of Chloride-Induced Filiform Corrosion on Iron Investigated by Time-Lapse Photomicrography.,” Singleton Park, Swansea, SA2 8PP, UK.

- [220] G. Williams, H. N. McMurray, D. Hayman, and P. C. Morgan, "Time-lapse potentiometric imaging of active filiform corrosion using a scanning Kelvin probe technique," *PhysChemComm*, vol. 4, no. 6, p. 26, 2001, doi: 10.1039/b100835h.
- [221] N. Wint *et al.*, "The kinetics and mechanism of filiform corrosion occurring on zinc-aluminium-magnesium coated steel," *Corrosion Science*, vol. 158, Sep. 2019, doi: 10.1016/j.corsci.2019.06.028.
- [222] Y. Xu, H. Li, Y. Shen, S. Liu, W. Wang, and J. Tao, "Improvement of adhesion performance between aluminum alloy sheet and epoxy based on anodizing technique," *International Journal of Adhesion and Adhesives*, vol. 70, pp. 74–80, Oct. 2016, doi: 10.1016/j.ijadhadh.2016.05.007.
- [223] V. Jothi, A. Y. Adesina, A. M. Kumar, N. Al-Aqeeli, and J. S. N. Ram, "Influence of an anodized layer on the adhesion and surface protective performance of organic coatings on AA2024 aerospace Al alloy," *Progress in Organic Coatings*, vol. 138, p. 105396, Jan. 2020, doi: 10.1016/j.porgcoat.2019.105396.